Title
Quest for High Temperature and Functional Quantum Anomalous Hall States

Author
Pan, Lei

Publication Date
2019

Peer reviewed|Thesis/dissertation

UNIVERSITY OF CALIFORNIA

Los Angeles

Quest for High Temperature and Functional Quantum Anomalous Hall States

A dissertation submitted in partial satisfaction of the

requirements for the degree Doctor of Philosophy in

Electrical and Computer Engineering

by

Lei Pan

2019

ABSTRACT OF THE DISSERTATION

Quest for High Temperature and Functional Quantum Anomalous Hall states

by

Lei Pan

Doctor of Philosophy in Electrical and Computer Engineering

University of California, Los Angeles, 2019

Professor Kang Lung Wang, Chair

Quantum anomalous Hall effect (QAHE) is the zero-field version of the quantum Hall effect which shows dissipationless chiral edge electron transport and quantized Hall resistance without the help of external magnetic field. In this Dissertation, we study the growth of magnetic topological insulator (MTI) Cr-doped $(BiSb)_2Te_3$ thin film, which is the host of the QAH states, using molecular beam epitaxy. We report the first observation of QAHE in a milli-meter sized device with the thin film thickness beyond the two-dimension (2D) limit. In addition, by controlling the thin film thickness down to the 2D limit, we observe a metal-to-insulator transition behavior due to the hybridization effect introduced by the vertical quantum confinement.

We further investigate the temperature limiting factors of QAHE in the Cr-doped $(BiSb)_2Te_3$ system by studying the thickness and doping effects. We identify that for thin film thickness larger than 6 quintuple layers (QLs), the limiting factor is the overlap of Fermi level with the trivial bulk band. For thin film thickness equal to 6 QLs, weak ferromagnetism and pronounced superparamagnetism are the temperature limiting factors. However, modulation doping technique can significantly strengthen the ferromagnetism at this thickness. In addition, the metal-to-

insulator transition behavior can also be tuned according to the doping profile of the thin film which can potentially affect the phase transition behavior in this material system.

To manipulate the QAH states, we investigate the heterogenous integration of the QAH insulator or TI with antiferromagnets. We first study the QAH insulator/Cr_2O_3 bilayer structure and realize the QAHE on a magnetically ordered system for the first time. We identify the positive exchange bias in this structure and discover the magnetic coupling between the two material systems using polarized neutron reflectometry (PNR). We then study the undoped TI/CrSe heterostructure and realize the antiferromagnet induced magnetic proximity effect in the TI layer confirmed by both PNR and X-ray magnetic dichroism techniques. We also discover the interface-dependent proximity behavior in the heterostructure that may help our understanding towards high temperature and functional QAH states.

The dissertation of Lei Pan is approved.

Chee Wei Wong

Hong-wen Jiang

Oscar M. Stafsudd

Kang Lung Wang, Committee Chair

University of California, Los Angeles

2019

This dissertation is dedicated to my parents,

for their unconditional love

Table of Contents

List of Figures

Acknowledgements

Foremost, I would like to express my sincere gratitude to my advisor Prof. Kang L. Wang for the continuous support of my Ph.D. study. His vision and passion are the beacons to my pursuit of knowledge. And his kindness and wisdom in life impact me far beyond research. It's a lesson of life that one cannot ask for more throughout my limited time at UCLA. I would also like to thank Mrs. Wang for the warmest caring towards every DRL members.

I would like to thank my committee members: Prof. Chee Wei Wong, Prof. Hong-wen Jiang and Prof. Oscar M. Stafsudd, for their time, encouragement and insightful guidance during my Ph.D. study. I would like to thank the tremendous help I received from the collaborators including: Prof. Jing Xia, Dr. Alex Stern and Mr. Brian Casas at UC Irvine, Prof. David Goldhaber-Gordon, Mr. Eli Fox, Prof. Shou-Cheng Zhang, Dr. Jing Wang and Dr. Biao Lian at Stanford, Dr. Alex Grutter at NIST, Prof. Wei-Li Lee at Institute of Physics, Academia Sinica, Prof. Christian Binek at University of Nebraska-Lincoln, Dr. Eun Sang Choi at National High Magnetic Field Lab, Prof. Sahashi Masashi, Prof. Tomohiro Nozaki at Tohoku University, Dr. Scott Chambers at Pacific Northwest National Laboratory, Prof. Xiaodong Han at Beijing University of Technology. The work presented in this thesis will not be possible without both the theoretical and experimental help and efforts from them. I would also like to thank Dr. Xiaoyu Yang, Dr. Ming Zhang, Dr. Qing Li, Dr. Zhongguang Xu and Mr. Liqin Xu for their help and guidance during my intern at Western Digital in 2018.

One of the greatest assets of my life I received during my Ph.D. study is the opportunity to work alongside with the wonderful DRL members. First of all, I would like to thank Prof. Xufeng Kou who not only leads me with great insights into the research field but also is a great friend for

life. I would like to thank Prof. Qing Lin He, Prof. Liang He, Dr. Koichi Murata, Prof. Tianxiao Nie, Dr. Peng Deng and Mr. Peng Zhang who are the best MBE people in the world. I would also like to thank Mr. Xiaoyu Che, Mr. Qiming Shao, Dr. Gen Yin, Dr. Chao-Yao Yang, Dr. Yabin Fan, Dr. Murong Lang, Ms. Yingying Wu, Dr. Li-Te Chang for their help both in theory and in experiment.

I would like to thank the financial support for this work including the Defense Advanced Research Projects Agency (DARPA) Meso program under contract No.N66001-12-1-4034 and N66001-11-1-4105, the Spins and Heat in Nanoscale Electronic Systems (SHINES), an Energy Frontier Research Center funded by the US Department of Energy (DOE), Office of Science, Basic Energy Sciences (BES), under Award # DE-SC0012670, the Army Research Office Multidisciplinary University Research Initiative (MURI) program accomplished under Grant Number W911NF-16-1-0472 and W911NF-15-1-10561, the Function Accelerated nanoMaterial Engineering (FAME) Center, one of six centers of STARnet, a Semiconductor Research Corporation (SRC) program sponsored by Microelectronics Advanced Research Corporation (MARCO) and DARPA. A portion of this work was performed at the National High Magnetic Field Laboratory, which is supported by the National Science Foundation Cooperative Agreement No. DMR-1644779, No. DMR-1157490 and the State of Florida.

Last but not least, I would like to express my deepest gratitude to my parents and my wife for their unconditional love, care and support.

VITA

Education

2013-2015 M.S. in Electrical Engineering
University of California, Los Angeles

2009-2013 B.Eng. (Hons.) in Electrical and Electronics Engineering
Nanyang Technological University, Singapore

Employment

2018 RAMP Memory Applications Engineering Intern
Western Digital

2013-2019 Graduate Student Researcher
Department of Electrical and Computer Engineering,
University of California, Los Angeles

Publications (*co-first author)

[1] "Probing the low temperature limit of quantum anomalous Hall effect" **L. Pan**, X. Liu, Q. He, A. Stern, G. Yin, X. Che, Q. Shao, C. Yang, B. Casas, E. Choi, J. Xia, X. Kou, K. L. Wang. In preparation 2019

[2] "Quantum anomalous Hall insulator/antiferromagnet Heterostructure" **L. Pan**, A.Grutter, X. Che, T. Nozaki, A. Stern, B. Casas, Q. He, G. Yin, Q. Shao, P. Zhang, P. Deng, X. Kou, S. Masashi, C. Binek, S. Chambers, J. Xia, K. L. Wang. In preparation 2019

[3] "Chiral Majorana edge state in a quantum anomalous Hall insulator-superconductor structure", Q. He*, **L. Pan***, A. Stern, E. Burks, X. Che, G. Yin, J. Wang, B. Lian, Q. Zhou, E. Choi, K. Murata, X. Kou, T. Nie, Q. Shao, Y. Fan, S. Zhang, K. Liu, J. Xia, K. Wang. Science 357, 294-299 (2017)

[4] "Metal-to-insulator switching in quantum anomalous Hall states", X. Kou*, **L. Pan***, J. Wang, Y. Fan, E. S. Choi, W. Lee, T. Nie, K. Murata, Q. Shao, S. Zhang, K. L. Wang. Nature Communications 2015, 6:8474

[5] "Antiferromagnetic proximity effect in topological insulator directly studied by an element-specific approach" C. Yang*****, **Lei Pan***, A. Grutter*****, H. Wang, X. Che, Q. He, D. A. Gilbert, E. Arenholz, Y. Wu, G. Yin, P. Deng, J. A. Borchers, W. Ratcliff, K. L. Wang. In preparation 2019

[6] "Zero-field edge plasmons in a magnetic topological insulator", A. Mahoney, J. I. Colless, L. Peeters, S. J. Pauka, E. J. Fox, X. Kou, **L. Pan**, K. L. Wang, D. Goldhaber-Gordon, D. J. Reilly. Nature Communications 2017, 8:1836

[7] "Electric-field control of spin-orbit torque in a magnetically doped topological insulator", Y. Fan, X. Kou, P. Upadhyaya, Q. Shao, **L. Pan**, M. Lang, X. Che, J. Tang, M. Montazeri, K. Murata, L. Chang, M. Akyol, G. Yu, T. Nie, K. L. Wong, J. Liu, Y. Wang, Y. Tserkovnyak, K. L. Wang. Nature Nanotechnology 11, 352–359 (2016).

[8] "Tailoring exchange couplings in magnetic topological-insulator/antiferromagnet heterostructures", Q. He, X. Kou, A. J. Grutter, G. Yin, **L. Pan**, X. Che, Y. Liu, T. Nie, B.

Zhang, S. M. Disseler, B. J. Kirby, W. Ratcliff II, Q. Shao, K. Murata, X. Zhu, G. Yu, Y. Fan, M. Montazeri, X. Han, J. Borchers, K. Wang. Nature Materials 16, 94–100 (2017).

[9] "Precise Quantization of the Anomalous Hall Effect near Zero Magnetic Field", A. Bestwick, E. Fox, X. Kou, **L. Pan**, K. L. Wang, D. Goldhaber-Gordon. Physical Review Letters 114, 187201.

[10] "Scale-Invariant Quantum Anomalous Hall Effect in Magnetic Topological Insulators beyond the Two-Dimensional Limit", X. Kou, S. Guo, Y. Fan, **L. Pan**, M. Lang, Y. Jiang, Q. Shao, T. Nie, K. Murata, J. Tang, Y. Wong, L. He, T. Lee, W. Lee, K. L. Wang. Physical Review Letters 113, 137201.

[11] "Topological transitions induced by antiferromagnetism in a thin-film topological insulator" Q.He, G. Yin, L. Yu, A. Grutter, **L. Pan**, C. Chen, X. Che, G. Yu, B. Zhang, Q. Shao, A. Stern, B. Casas, J. Xia, X. Han, B. Kirby, R. Lake, K. Law, K. L. Wang. Physical Review Letters 121, 096802.

[12] "Role of dimensional crossover on spin-orbit torque efficiency in magnetic insulator thin films" Q. Shao, C. Tang, G. Yu, A. Navabi, H. Wu, C. He, J. Li, P. Upadhyaya, P. Zhang, S. Razavi, Q. He, Y. Liu, P. Yang, S. Kim, C. Zheng, Y. Liu, **L. Pan**, R. Lake, X. Han, Y. Tserkovnyak, J. Shi, K. L. Wang. Nature communications 3612 (2018).

[13] "Exchange-biasing topological charges by antiferromagnetism" Q. He, G. Yin, A. Grutter, **L. Pan**, X. Che, G. Yu, D. A Gilbert, S. Disseler, Y. Liu, P. Shafer, B. Zhang, Y. Wu, B. Kirby, E. Arenholz, R. Lake, X. Han, K. L. Wang. Nature Communications 2767 (2018).

[14] "Unidirectional Magneto-Resistance in Modulation-doped Magnetic Topological Insulators" Y. Fan, Q. Shao, **L. Pan**, X. Che, Q. He, G. Yin, C. Zheng, G. Yu, T. Nie, M. R. Masir, A. MacDonald, K. L. Wang. Nano Letters 2019, 19 (2), pp 692–698.

[15] "Room Temperature Highly Efficient Topological Insulator/Mo/CoFeB Spin-Orbit Torque Memory with Perpendicular Magnetic Anisotropy" Q. Shao, H. Wu, Q. Pan, P. Zhang, **L. Pan**, K. Wong, X. Che, K. L. Wang. IEDM 36.3.1-36.3.4

[16] "Proximity-Induced Magnetic Order in a Transferred Topological Insulator Thin Film on a Magnetic Insulator" X. Che, K. Murata, **L. Pan**, Q. He, G. Yu, Q. Shao, G. Yin, P. Deng, Y. Fan, B. Ma, X. Liang, B. Zhang, X. Han, L. Bi, Q. Yang, H. Zhang, K. L. Wang. ACS Nano, 2018, 12 (5), pp 5042–5050

[17] "Part-per-million quantization and current-induced breakdown of the quantum anomalous Hall effect" E. Fox, I. Rosen, Y. Yang, G. Jones, R. Elmquist, X. Kou, **L. Pan**, K. L. Wang, D. Goldhaber-Gordon. Phys. Rev. B 98, 075145

[18] "TiO_2 rutile-anatase core-shell nanorod and nanotube arrays for photocatalytic applications", **L. Pan**, H. Huang, C. K. Lim, Q. Y. Hong, M. S. Tse, O. K. Tan. RSC Advances, 2013, 3 (11), 3566 – 3571.

[19] "Hydrothermal Growth of TiO2 Nanorod Arrays and In Situ Conversion to Nanotube Arrays for Highly Efficient Quantum Dot-Sensitized Solar Cells", H. Huang, **L. Pan**, C. K. Lim, H. Gong, J. Guo, M. S. Tse, O. K. Tan. Small, 2013, 9(18), 3153-3160.

Chapter 1

Introduction

1.1. Topological insulator

Topological insulator (TI) is a new class of quantum material which possesses a bulk band gap and topologically protected surface states when interfaced with vacuum or a trivial insulator[1-3]. Such unique property arises from its inverted bulk band structure caused by the strong spin-orbit coupling (SOC). In common semiconductors with a trivial band gap, the conduction band is often formed from electrons in *s* orbitals while the valence band is formed from electrons in *p* orbitals. The conduction band is always above the valence band which results a positive band gap E_g. In the TI case, which usually consists of heavy elements, possesses strong SOC so that the *p* orbital band is pushed above the *s* orbital band. The band structure is effectively inverted in this case and the band gap E_g can be considered as negative. When TI is interfaced with a positive-gap material (e.g., vacuum or trivial semiconductor), due to the continuity of wavefunction at the boundary, the energy gap will close and results exotic surface/edge state.

1.2. Quantum spin Hall effect

The spin Hall effect describes the phenomenon where a spin current flows perpendicular to an applied electric field in a strong SOC material[4-6]. The quantized version of the spin Hall

effect, known as the quantum spin Hall (QSH) effect, describes the spin current that is carried by helical edge states in two-dimensional materials without dissipation. Being protected by time-reversal symmetry, odd number of pairs of helical states cannot open a gap at the edge which ensures that the back-scattering by non-magnetic impurities are forbidden. It is also found out that such time-reversal property is associated with a novel Z_2 topological invariant. This topological invariant defines the QSH state as a topologically distinct new state of matter which is the first topological insulator system to be understood.

The first theoretical approach to realize QSH effect was done by C. L. Kane and E. J. Mele back in 2005 when they tried to introduce SOC into a graphene strip[7, 8]. They studied the topological number of the system and concluded a large enough SOC could drive the graphene into a state of matter that is gapped in the bulk and with gapless helical edge states. However, in reality, the gap opened by the SOC in graphene is extremely small[9], on the order of 10^{-3} meV, making it an unrealistic material system to study the QSH effect.

The first viable material system to realize the QSH effect was proposed by B. A. Bernevig *et al.* in 2006[10] who suggested the CdTe/HgTe/CdTe quantum well might host the QSH states after fine tuning the HgTe thickness. Explained in schematic band diagram drawing as shown in Figure 1-1, the CdTe is a trivial semiconductor with the s-type Γ_6 band sitting on top of the p-type Γ_8 band and the quantum well material HgTe is non-trivial with the Γ_8 band on top of the Γ_6 due to large SOC. Theoretical calculation suggests that there exists a critical thickness $d_c = 6.5$ nm of the HgTe layer, below which the heterostructure is merely a trivial semiconductor dominated by the CdTe band structure. However, when the HgTe thickness is beyond the d_c, the whole system will be driven in the QSH state due to the band inversion in the HgTe layer and the topological number change at the HgTe/CdTe boundary.

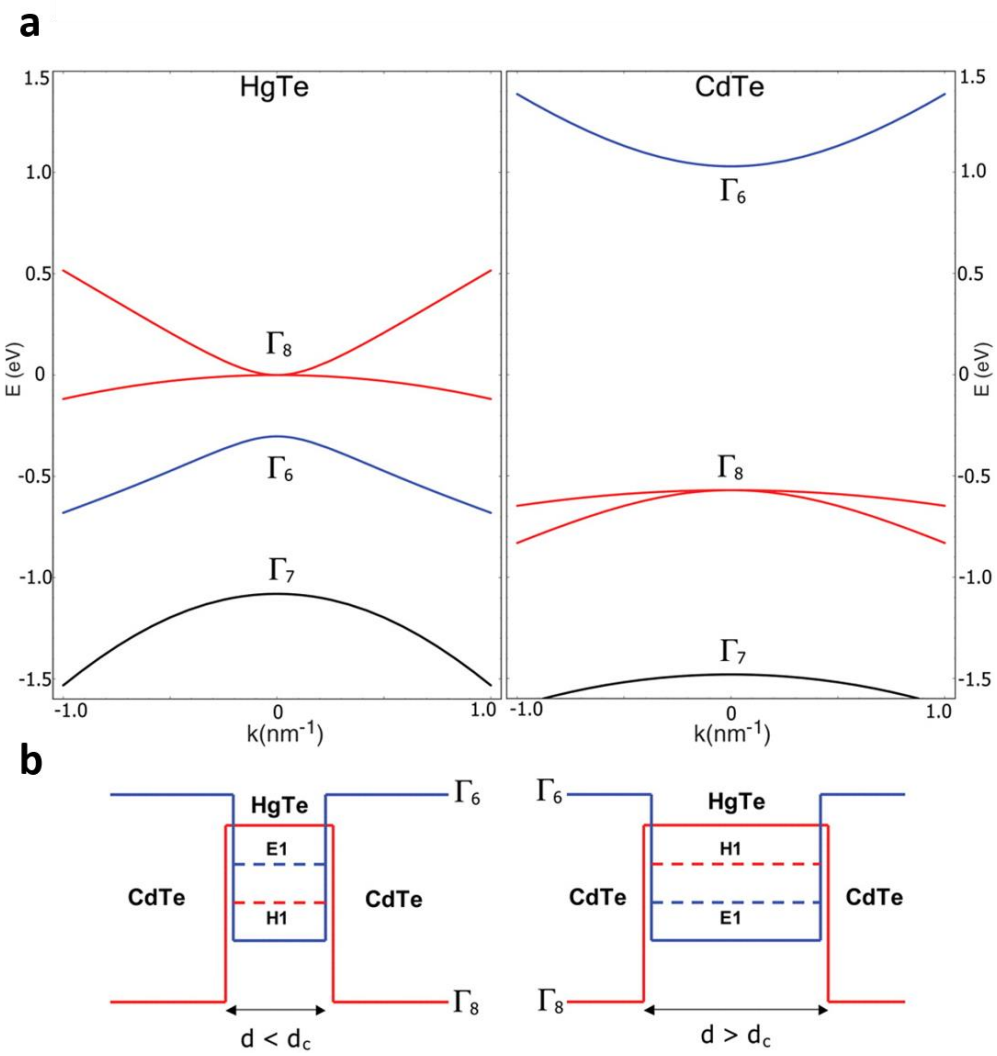

Figure 1-1 CdTe/HgTe/CdTe quantum wells. (a) Bulk energy bands of HgTe and CdTe near the Γ point. (b) Left: quantum well in normal regime $E_1>H_1$ with HgTe thickness$<d_c$. Right: quantum well in inverted regime $H_1>E_1$ with HgTe thickness$>d_c$. Adopted from Ref. [10].

In 2007, the QSH effect was experimentally realized by König et al. in the HgTe/(Hg,Cd)Te quantum wells[11]. Transport properties of the molecular-beam-epitaxy-grown quantum wells were measured as a function of gate voltage, sample thickness and external magnetic field. The authors found that when quantum well thickness is below 6.3 nm, which is in good agreement with the theoretically predicted critical thickness, the sample behaved like an

insulator with a vanishingly small conductance at low temperature. However, when the quantum well thickness was above the critical thickness, a residual 2 e^2/h (where e is the electron charge and h is Planck's constant) longitudinal conductance was measured as shown in Figure 1-2. The residual quantized conductance was independent of the sample size and could be destroyed by a small external magnetic field which further confirmed its helical quantum transport nature.

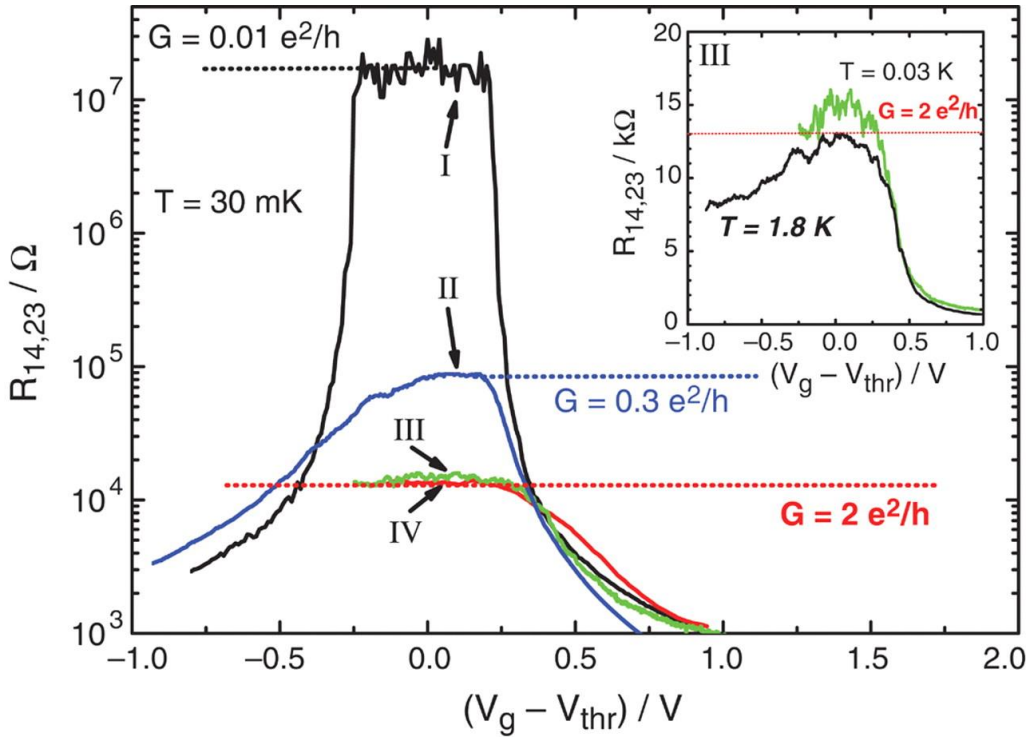

Figure 1-2 Quantum spin Hall effect in HgTe/CdTe quantum wells. The longitudinal four-terminal resistance, $R_{14,23}$, of various normal (d = 5.5 nm) (I) and inverted (d = 7.3 nm) (II, III, and IV) quantum well structures as a function of the gate voltage measured for B = 0 T at T = 30 mK. Adopted from Ref. [11].

More recently, the QSH effect was observed in another two material systems including the InAs/GaSb quantum wells[12] and the single layer WTe_2[13]. Both material systems demonstrated QSH state's transport signature at higher temperature (4 K for InAs/GaSb quantum wells, 100 K

for WTe_2). Specifically, for the WTe_2 system, the importance of this finding is twofold: firstly, the observation of the dissipationless edge transport surpassed liquid nitrogen temperature (77 K); secondly, it is the first intrinsic QSH insulator discovered so far which have many advantages in terms of preparation and heterogenous integration with other condensed matters.

1.3. Three-dimensional topological insulators

Despite the early effort in realizing the QSH insulator in two-dimensional (2D) materials, the topological insulator theory quickly extended to three-dimensional spaces[14-16]. Being similar as the 2D TI case where the insulating bulk coexists with the metallic edge states, in three-dimensional (3D) TI, the bulk band coexists with the gapless surface states which are protected by time-reversal symmetry. The surface states of a 3D TI consist of an odd number of massless Dirac cones ensured by the Z_2 topological invariant of the bulk band[14].

The first proposed 3D TI is the $Bi_{1-x}Sb_x$ alloy[14] and later confirmed experimentally using angle-resolved photoemission spectroscopy (ARPES)[17]. The ARPES technique since then became a standard approach to verify materials' topological property because it can present direct evidence of the topological surface states. However, the TI property other than the hints of the Dirac cone on the $Bi_{1-x}Sb_x$ alloy surface is hard to access due to its complex band structure. Another class of layered and stoichiometric tetradymite compound including Bi_2Te_3, Bi_2Se_3 and Sb_2Te_3 were proposed after the $Bi_{1-x}Sb_x$ alloy to be 3D TIs with a single Dirac cone on the surface[18]. In addition, they were predicted to have a bulk band gap as large as 0.3 eV. Such signatures were quickly confirmed using ARPES technique[19]. A typical Bi_2Se_3 ARPES image is shown in Figure 1-3 depicting the detailed bulk band and Dirac surface band information.

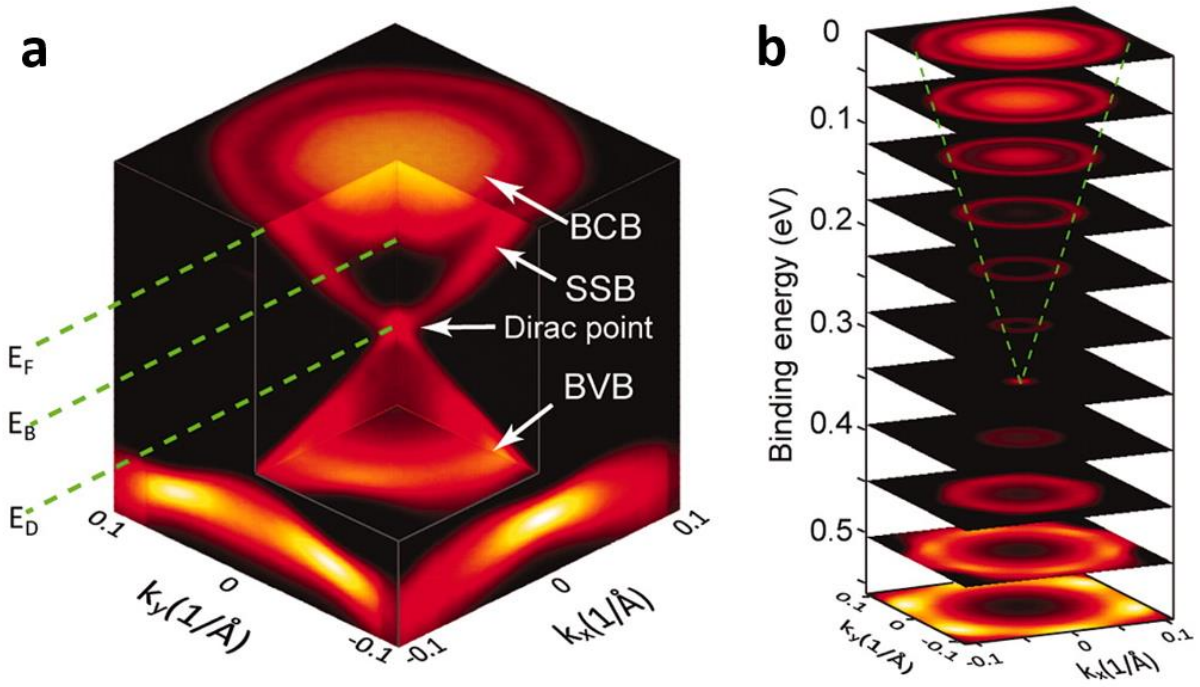

Figure 1-3 Electronic band structure of undoped Bi_2Se_3 measured by ARPES. (a) The bulk conduction band (BCB), bulk valence band (BVB), and surface-state band (SSB) are indicated, along with the Fermi energy (E_F), the bottom of the BCB (E_B), and the Dirac point (E_D). Adopted from Ref. [20].

The tetradymite 3D TI family (Bi_2Te_3, Sb_2Te_3, and Bi_2Se_3) has multiple advantages making it the most studied topological materials to date. The first advantage is the simple band structure and accessible surface states. The topological surface state is within the ~0.3 eV bulk band which can provide pure surface state signature using transport measurement. Also, there is only one Dirac cone at the Γ point which is helpful to achieve clean measurement results. Secondly, the Bi_2Te_3 and Sb_2Te_3 3D TIs are able to form ternary 3D TI compound $(Bi_{1-x}Sb_x)_2Te_3$ using molecular beam epitaxy (MBE). The Bi to Sb ratio can be tuned freely to achieve truly bulk-insulating TI[21]. Thirdly, long range ferromagnetic order can be introduced into this 3D TI system using transition metal doping method also by the MBE technique[20, 22, 23]. The introduction of ferromagnetism

will break the time-reversal symmetry of the TI and result a gap opening at the Dirac point which makes the surface Dirac fermion massive[1]. The breaking of time-reversal symmetry may lead to many other exotic physics including the quantum anomalous Hall effect (QAHE), axion electrodynamics, induced magnetic monopole, etc.[1, 24, 25] The fourth advantage is similar as the WTe_2 which is an intrinsic TI, tetradymite 3D TI family is also intrinsic. The accessible TI surface states can be heterogeneously integrated with other material systems including ferromagnets[26, 27], antiferromagnets[28, 29] and superconductors[30].

1.4. Quantum anomalous Hall effect

In the 3D TI system, one of the most important findings is the quantum anomalous Hall effect. Sharing the similar topological nature and dissipationless chiral edge state transport signature, one of the major differences between the quantum Hall effect and the quantum anomalous Hall effect is that no external field is required for the latter case. Although the first zero-field dissipationless edge state was discovered as the QSH state in 2007, the theory of QAH effect was first explored since 1988 by Haldane[31]. In this early approach to realize the zero-field version of the quantum Hall effect, a graphene-like lattice with a periodic local magnetic-flux was proposed. To date, this system is still not physically realizable, but it indicates that the quantum Hall effect does not necessarily require an external magnetic field and can be approached in a wider context related to phenomena with broken time-reversal invariance.

Another approach to realize the QAH effect is based on the QSH system. Liu *et al.* proposed to dope the HgTe quantum well with Mn atoms and introduce ferromagnetism into the system, such that one pair of the spin sub-band will be driven into a trivial state and hence

transforms a QSH state into a QAH state[32]. However, Mn-doped HgTe quantum well is a paramagnet which requires a small external magnetic field to drive the system into quantized state[33].

In the case of tetradymite 3D TI, ferromagnetism is no longer an issue. Transition metal (Cr, Mn or V) can be doped into the parent 3D TI compound in a substitutional manner and induce out-of-plane ferromagnetic order up to 100 K[34]. Such ferromagnetic ordering can induce an exchange field along the out-of-plane axis and the Hamiltonian of the surface state can be written in the form of:

$$H = \begin{bmatrix} h_k + gM\sigma_z & 0 \\ 0 & h_k^* - gM\sigma_z \end{bmatrix} \qquad (1-1)$$

With the basis: $|+\uparrow\rangle$, $|-\downarrow\rangle$, $|+\downarrow\rangle$, $|-\uparrow\rangle$, where $|\pm\uparrow\rangle = (|t\uparrow\rangle \pm |b\uparrow\rangle)/\sqrt{2}$, $|\pm\downarrow\rangle = (|t\downarrow\rangle \pm |b\downarrow\rangle)/\sqrt{2}$. Here t, b represent the top and bottom surfaces and $\uparrow$, $\downarrow$ represent the spin up and down states. In addition, $h_k = v_F(k_y\sigma_x - k_x\sigma_y)$, where v_F is the Fermi velocity, g is the effective g factor, σ is the Pauli matrix and M is the exchange field along the out-of-plane axis.

The surface band evolution when exchange field is introduced into TI is shown in Figure 1-4. It is noted that the starting point to realize the QAH effect does not have to be a TI where a sufficiently large exchange field can change the Chern number of the system. If the system starts from a topological trivial case as shown in Figure 1-4(a), the exchange field can pull the upper block subbands into a band inversion state and push the lower block subbands further away. On the other hand, if the system starts from a topological non-trivial case as shown in Figure 1-4(b) where both subbands are inverted, the exchange field can increase the band inversion in the upper

block subbands and release the inversion in the lower block. Both surface band evolving paths can result a QAH insulator.

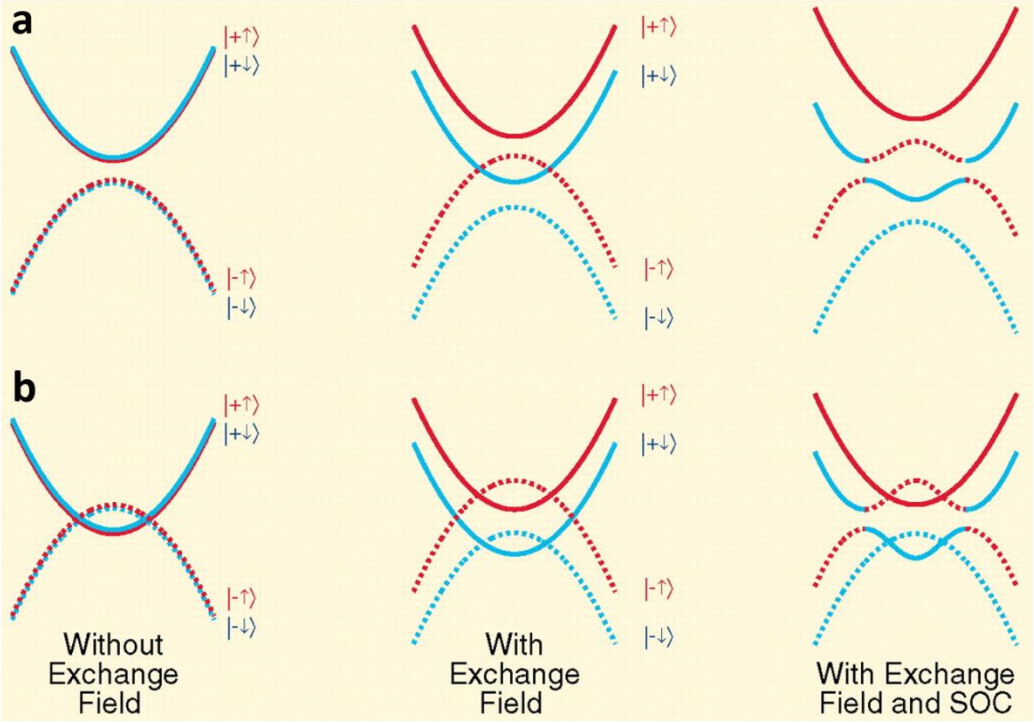

Figure 1-4 Evolution of the subband structure upon increasing the exchange field. The solid lines denote the subbands that have even parity at Γ point, and dashed lines denote subbands with odd parity at Γ point. The blue color denotes the spin down electrons; red, spin up electrons. (a) The initial subbands are not inverted. When the exchange field is strong enough, a pair of inverted subbands appears (red dashed line and blue solid line). (b) The initial subbands are already inverted. The exchange field releases the band inversion in one pair of subbands (red solid line and blue dashed line) and increase the band inversion in the other pair (red dashed line and blue solid line). Adopted from Ref. [24].

Although in theory both approaches to realize the QAH effect may work, in reality, trivial ferromagnet with simple surface band structure and large enough exchange field to invert one pair of the spin subband (as shown in Figure 1-4(a)) is very hard to find. The second approach (as

shown in Figure 1-4(b)) turns out to be much more feasible. In 2013, Chang *et al.* reported the first observation of QAH effect in the $Cr_{0.15}(Bi_{0.1}Sb_{0.9})_{1.85}Te_3$ thin films grown on $SrTiO_3$ substrate using the MBE technique. The $SrTiO_3$ substrate also serves as a back gate because of its large dielectric constant at low temperature. By applying a gate voltage, the Fermi level of the material can be tuned into the bulk band gap and the surface subband gap. In this case, V_g at -1.5 V is the optimal back-gate voltage value which resulted a quantized Hall resistivity ρ_{yx} at h/e^2 as shown in Figure 1-5(a). In the meantime, the longitudinal resistivity ρ_{xx} dropped to 0.098 h/e^2 as shown in Figure 1-5(c). The quantized state only happened at a very small back-gate voltage window around -1.5 V. The Hall and longitudinal resistivity and the converted conductivity quickly deviated from the quantized value (marked as dashed line in the graph) when the gate voltage was outside of the window as shown in Figure 1-5(b) and (d).

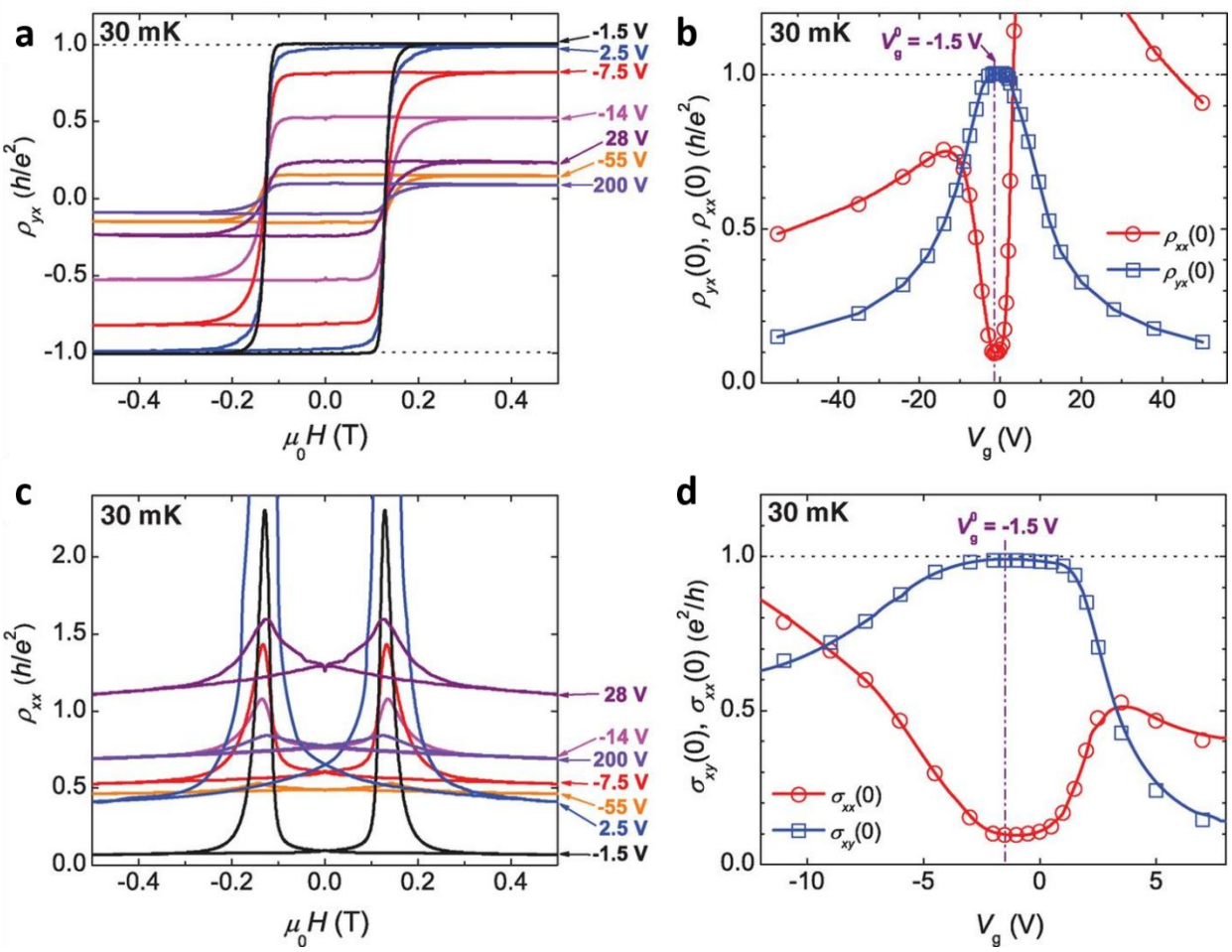

Figure 1-5 The transport signature of the QAH effect in Cr-doped $(BiSb)_2Te_3$. (a) Magnetic field dependence of ρ_{yx} at different back-gate voltage. (b) Dependence of $\rho_{yx}(0)$ (empty blue squares) and $\rho_{xx}(0)$ (empty red circles) on V_g. 0 means the optimal back-gate voltage. (c) Magnetic field dependence of ρ_{xx} at different V_g. (d) Dependence of $\sigma_{xy}(0)$ (empty blue squares) and $\sigma_{xx}(0)$ (empty red circles) on V_g. Adopted from Ref. [35].

1.5. Organization

In this dissertation, we summarize our work on the quantum anomalous Hall insulator and its related heterostructures. The contents are arranged as follows. In Chapter 2, we show the molecular beam epitaxy growth of quantum anomalous Hall insulator, topological insulator and

their related heterostructures. In Chapter 3, we discuss the quantum anomalous Hall effect we observed in our material and the temperature limiting factors in the system. In Chapter 4, we show the magnetic coupling and proximity effect between topological insulator and antiferromagnet systems. Chapter 5 is the conclusion chapter of this dissertation.

Chapter 2

Molecular beam epitaxy growth of topological insulator and related heterostructures

In this dissertation, all the topological insulators were grown using the molecular beam epitaxy technique in a Perkin-Elmer made ultra-high vacuum (UHV) system. Depending on the specific heterostructure, thin films other than the topological insulator were integrated into the structure by serving as a substrate, *in-situ* grown in the same molecular beam epitaxy (MBE) chamber or *ex-situ* grown in a different chamber.

2.1. Molecular beam epitaxy

Molecular beam epitaxy technique is a thin-film epitaxy growth method to achieve high quality single-crystals. It was first developed by Alfred Cho and John Arthur in the late 1960s[36, 37]. MBE has several advantages owing to its unique growth method and environment. Firstly, the growth is performed in UHV allowing low impurity density and slow layer-by-layer growth at the same time. Secondly, the growth temperature is relatively lower than other growth technique, *e.g.*, chemical vapor deposition and liquid phase epitaxy, which enables stable heterostructure or superlattice formation that is far from the thermodynamic equilibrium. Thirdly, during the growth, powerful *in-situ* monitoring technique including the reflective higher-energy electron diffraction

(RHEED), low-energy electron diffraction (LEED), etc., can provide real-time crystal growth information down to atomic scale.

In our Device Research Lab at UCLA, all MBE growths are performed in a Perkin-Elmer ultra-high vacuum system (shown in Figure 2-1) with a base pressure in the range of 10^{-10} Torr. The system is equipped with 8 effusion cells capable of growing Bi, Sb, Te, Se, Al, Cr, Sn, Mn. The Sb and Se cells are specially designed with a cracker to achieve pure and controllable molecular flux. The Te cell uses a unique hot-lip design to avoid material condensation at the crucible end and to extend the source refilling cycles. In addition to the Knudsen cells, the system is also equipped with an e-gun evaporator that can generate W, Mo, V and Nb fluxes using high power electron beam heating. The main chamber is maintained at UHV through an integration of a three-stage transfer process. During the transfer of the sample between the atmospheric pressure (760 Torr) and the UHV growth chamber (10^{-10} Torr, maintained by one ion pump and one cryo-pump), sample will go through a load-lock first (10^{-6} Torr, maintained by a turbomolecular pump) and then a transfer tube (10^{-8} Torr, maintained by an ion pump). In that way the main chamber's UHV environment's exposure towards impurities is minimized which is critical for realizing consistent and high-quality MBE grown thin films. The growth environment is actively monitored by an ionization gauge which shows the total pressure in the chamber and a residual gas analyzer (RGA) that can provide accurate residual gases' mass spectrum. The RGA system may also serve as a leak detector when needed by monitoring the helium partial pressure inside the chamber when exposing possible leakage spot with ultra-high purity helium gas.

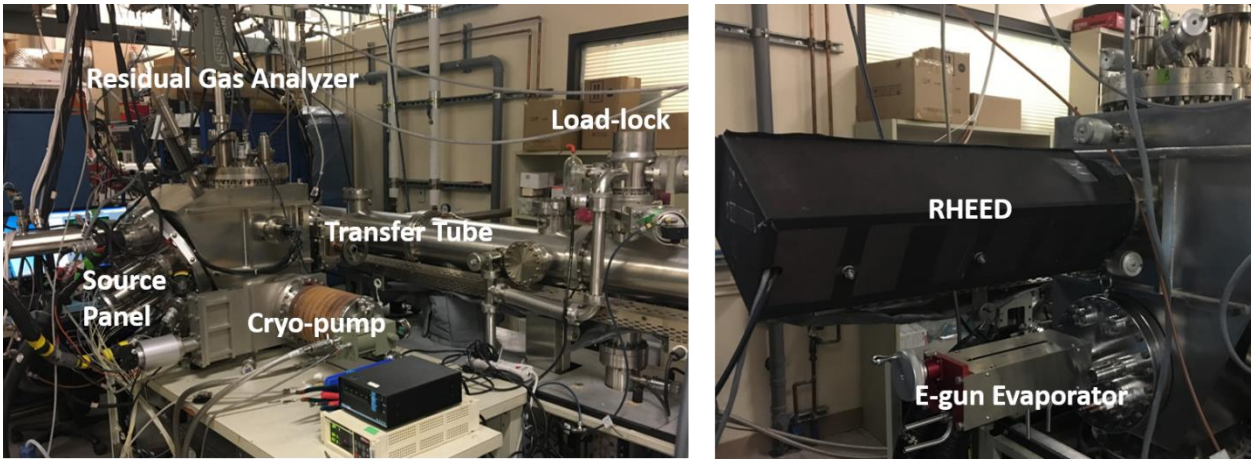

Figure 2-1 MBE system in Device Research Lab, UCLA. The system is equipped with 8 Knudsen cells (2 have crackers), 1 e-gun evaporator with 4 crucibles. The system is capable of growing 12 elements including Bi, Sb, Te, Se, Cr, Al, Sn, Mn, W, Nb, Mo and V.

During the MBE growth, the first step is to fill the source panel's cooling shroud with liquid nitrogen (shown in the schematic drawing in Figure 2-2). This step further lowers down the growth chamber's pressure by trapping both gas vapor with higher condensation temperature than liquid nitrogen and unused beam fluxes. Also, in the case of evaporating element at relatively higher temperature (> 600 °C), the liquid nitrogen filled shroud serves as a protection layer to avoid structural damage towards stainless steel made chamber.

After that, clean substrate will be mounted onto the molybdenum-made substrate holder using indium as the glue at elevated temperature (~ 200 °C to melt the indium). Using the indium as glue has the advantage of avoiding introducing organic materials into the UHV system, and in the meantime, it provides a superior thermal conductivity which ensures uniform substrate temperature and fast temperature responses during the change of the substrate heating power.

The substrate holder will then be transferred to the growth chamber. Depending on the substrate, different thermal treatment will be applied to further clean the surface at an elevated temperature. Being different from the substrate temperature, the source temperatures are usually maintained at elevated growth temperature since the beginning of the growth day to ensure stable and high-purity molecular beam for the subsequent growth. After the thermal treatment of the substrate, its temperature will be lowered down to the growth temperature according to the recipe for which we have optimized. During the growth, computer controlled pneumatic shutters will be opened for different sources depending on the molecular beam we would like to have. The shutter opening schedule is also programmable allowing fast switching between different beam elemental compositions which enables the superlattice growth.

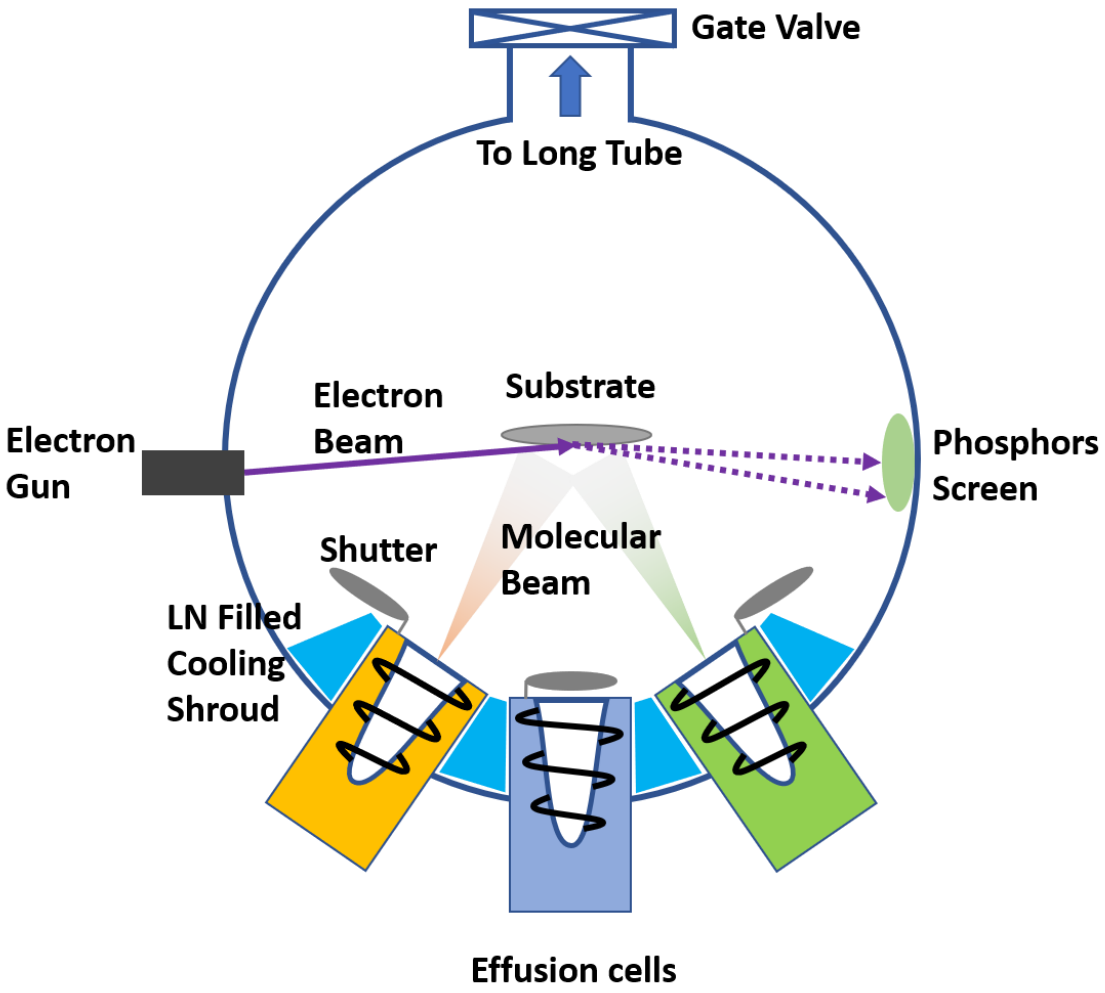

Figure 2-2 Schematic drawing of DRL MBE setup. This system is equipped with effusion cell cooled by LN shroud, pneumatic shutter and RHEED system.

One of the key advantages of MBE is the *in-situ* monitoring of the as-grown crystals using electron diffraction technique, our MBE system is also equipped with the RHEED system (KSA Associates.) which provides pivotal information regarding the on-going growth. As shown in the schematic drawings in Figure 2-2, the electron gun that is attached to the side of the growth chamber will emit high energy electron beams (>8 keV) towards the substrate in a shallow angle (<5°). 8 keV electron energy corresponds to a wavelength around 0.26 Å that is sufficient to

resolve crystal details down to atom-to-atom scale. The shallow angle of the incident electron beam is to make sure a small penetration depth and ensures that the technique is only surface sensitive. The diffraction process follows the Laue diffraction condition [38]:

$$\boldsymbol{k}_{out} - \boldsymbol{k}_{in} = \Delta\boldsymbol{k} = \boldsymbol{G} \qquad (2-1)$$

where $\boldsymbol{k}_{out}$ and $\boldsymbol{k}_{in}$ are the outgoing (diffracted) and incoming (incident) beams' wavevectors and $\boldsymbol{G}$ is the crystal's reciprocal lattice vector. The crystal surface in ideal case during the growth can be viewed as an infinite two-dimensional lattice point spaced in a periodic way. In such case, the reciprocal lattice for the crystal surface is an infinite arrays of lattice rod (with infinitesimal radius) spaced by $(\frac{2\pi n}{a_1}, \frac{2\pi m}{a_2})$ where n and m are integers; a_1 and a_2 are the lattice constants of the real space lattice in the orthogonal direction(assuming rectangular lattice). To fulfill the diffraction condition, an Ewald sphere can be constructed using the incident beam's wavevector as the radius shown in Figure 2-3(left). The intersection between the reciprocal lattice rod and the Ewald sphere fulfills the Laue diffraction condition and will result a diffraction pattern on the phosphors screen.

However, in real case, the reciprocal lattice rod always has finite radius. There are three major factors limiting the technique generating an ideal diffraction pattern. The first one is that the electron beam is not perfectly monochromatic, electron beams with different wavelength will create an Ewald sphere with finite thickness and broadens the diffraction pattern. The second one is the coherent length of the crystal surface, due to unavoidable defects at the crystal surface, it can no longer be viewed as a two-dimensional periodical lattice with infinite size. Imposing such boundary conditions onto the reciprocal lattice conversion, the lattice rod will have finite radius.

The third one is called transfer width which is strongly related to the instrument limit and its response.

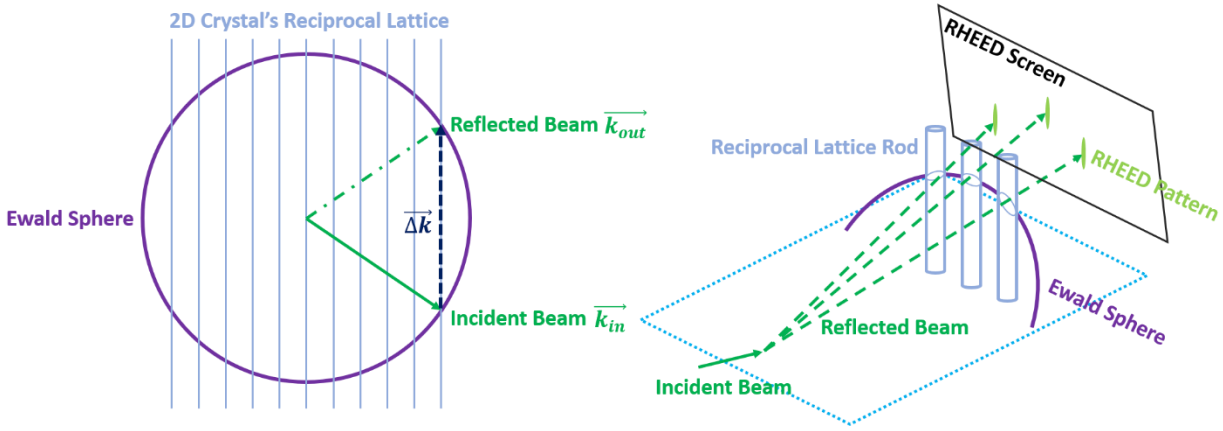

Figure 2-3 Schematic drawing of RHEED pattern formation. Left: Ideal Ewald sphere construction to determine the diffraction condition that is satisfied by incident beam, outgoing beam and reciprocal lattice rod. Right: In real case scenario, the reciprocal lattice rod will have finite radius and result streaky RHEED pattern with finite size.

Beyond the monitoring of the crystal quality, RHEED system can also provide important growth rate information when the crystal is growing in a layer-by-layer mode as shown in Figure 2-4. During the layer-by-layer growth, the crystal surface undergoes a series of island nucleation, island expansion and finally the formation of a new layer process. In this period, the crystal surface's roughness also evolves in a cycle from smooth to rough then back to smooth. Reflected in the RHEED pattern intensity, the smooth surface results a brighter coherent spot while the rough surface results a dimmer spot. Counting the period between two RHEED intensity peaks can provide us an accurate growth rate for 1 monolayer of the thin film. This technique plays a pivotal role in our later thickness dependent quantum anomalous Hall insulator study.

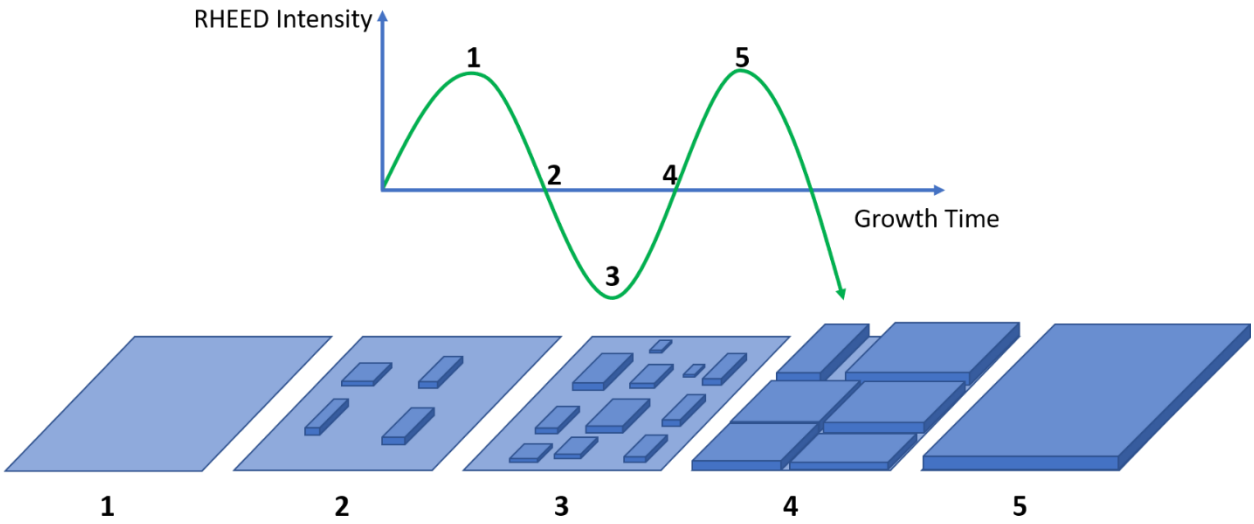

Figure 2-4 RHEED intensity oscillation during layer-by-layer growth mode. Smooth surface results brighter RHEED pattern and rough surface results dimmer RHEED pattern. The oscillation period is equal to the monolayer growth time.

After the growth of the thin film, the substrate will be cooled down to room temperature. Depending on the purpose of the study, capping layer may be deposited onto the surface at this temperature. 2 nm Aluminum capping is the most frequently used technique which shows robust protection of the thin film against ambient oxidation and degradation[39]. Tellurium and Selenium capping will be used if the capping layer is to be removed in the future for other surface sensitive studies.

2.2. MBE growth of TI on GaAs

Since the proposal of topological insulator, multiple material systems have been theoretically and experimentally investigated regarding its topological property, including HgTe/CdTe quantum well[10, 11], InAs/GaSb bilayers[40], BiSb alloys[41, 42] and Bi_2Te_3 based

crystals[18, 19]. Among all the materials, the Bi_2Te_3 based tetradymite-type 3D TI is the most intensively studied material system due to its stable chemical property, large bulk bandgap and readily mature growth technique. In this dissertation, all the topological insulator materials are based on it.

To utilize the advantage of MBE for TI growth, the first task is to identify a suitable substrate. The Bi_2Te_3 TI family has a rhombohedral crystal structure. It also has a layered structure consisting of five atomic layers as a basic unit cell that is named as quintuple layer (QL). The five atomic layer stacks in the order of Te-Bi-Te-Bi-Te where Bi and Te are strongly bonded in a covalent manner. Between QLs, Te and Te atoms are bonded through weaker van der Waals force. Single QL of Bi_2Te_3 is effectively a 2D material similar as graphene without dangling bonds. In the hexagonal representation of the rhombohedral crystal structure, the stacking of the QLs align in the [0001] direction of the crystal and the van der Waals gap is also in the (0001) plane. In such representation, Bi_2Te_3 possesses a lattice constant of a=4.38 Å and c=30.49 Å.

After trying multiples substrate for TI growth, GaAs(111)B substrate was chose because of the following reasons:

1. GaAs(111)B in hexagonal representation has a lattice constant of a=4 Å. The lattice mismatch is below 10%. By growing along the [0001] axis, we are likely to utilize the unique van der Waals epitaxy mechanism that is more tolerant towards lattice mismatch[43].
2. GaAs surface is self-passivated with native oxide and the treatment before the growth is well-established with clear surface reconstruction.

3. Semi-insulating GaAs substrate is widely available which is essential for clean electrical signal measurement.
4. GaAs substrate is much cheaper than InP(a=4.15 Å) and CdS(a=4.12 Å) substrate which also share similar lattice constant with the Bi_2Te_3 TI family.

To start the growth, the GaAs substrate will first be ultrasonically cleaned using acetone to remove possible organic contaminations. After that, the substrate will be loaded onto the substrate holder and then be transferred into the growth chamber. The substrate temperature will be raised to 300 °C and be kept at this temperature for 30 minutes to thermally clean the surface. Then the temperature will be raised to 580 °C to remove the native oxide. During the annealing, Se molecular beam will be supplied to suppress the As atom escaping which will generate unwanted pits on the substrate. The Se rich environment will also form a monolayer of GaSe on GaAs surface as a passivation layer which promotes van der Waals epitaxy[44]. The growth temperature for Bi_2Te_3 based TI is at 200 °C. There are usually two other elements being introduced into the material system. The first one is Sb which proves to be able to fine tune the thin film's Fermi level without sacrificing its topological property[21]. The Fermi level position is crucial to access the transport property of topological surface states. The preferred position is the bulk band gap which greatly reduces trivial bulk carriers' involvement in the transport signal. It is later found out that the observation of quantum anomalous Hall effect also relies on the correct Sb doping level. The second element that is frequently introduced into the Bi_2Te_3 based TI is Cr. The purpose of Cr doping is to introduce ferromagnetism into the system which can break the time-reversal symmetry of the topological surface states and introduce an exchange gap[22, 23, 45]. During the growth, the (1×1) RHEED pattern of GaAs(111)B quickly evolves into the (1×1) Bi_2Te_3 based pattern as shown in Figure 2-5. The d-spacing between the first order RHEED stripes which is inversely

proportional to the crystal's lattice constant also quickly decreases as Bi_2Te_3 based TI family has larger lattice constant. This particular sample shown in Figure 2-5 which is a Cr-doped $(BiSb)_2Te_3$ thin film provides an estimated lattice constant around 4.21 Å using its relative relationship with the initial GaAs lattice constant. This is an indication of successful Sb incorporation into the system because of the smaller lattice constant of Sb_2Te_3(4.25 Å).

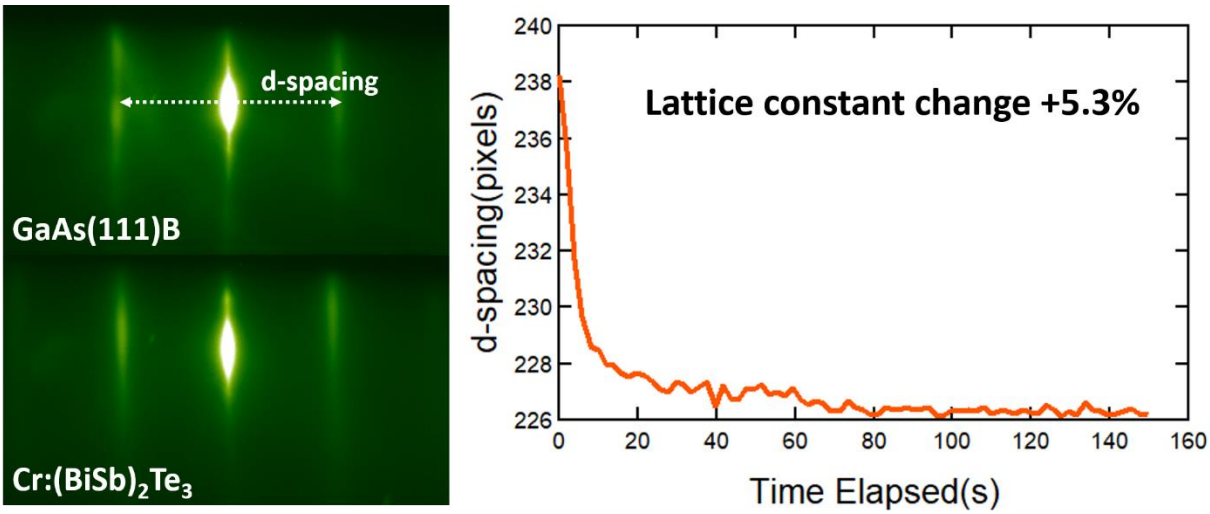

Figure 2-5 RHEED image of Cr-doped $(BiSb)_2Te_3$ growth on GaAs substrate. Left: RHEED image of GaAs(111)B substrate after the Se-rich pre-annealing and after the Cr-doped $(BiSb)_2Te_3$ growth. Right: The change of pixel number between the first order RHEED stripes known as the d-spacing during the Cr-doped TI growth. The change percentage when converted back to the lattice constant is around 5.3% which corresponds to high Sb:Bi atomic ratio.

During the TI growth, there are few parameter or parameter pairs that have great impact towards the material quality and the doping level. The first parameter pair is the substrate temperature (T_{SUB}) and the tellurium flux. The Bi_2Te_3 based TI growth is very similar to the GaAs MBE growth where the Ga flux determines the growth rate while the As flux is oversupplied because of its lower sticking coefficient than Ga. In Bi_2Te_3 case, Te is oversupplied by around 20

times more than Bi/Sb flux. The T_{SUB} in this case is dynamically adjusting this ratio by controlling the sticking coefficient of Te which is more sensitive than Bi/Sb. Shifting away from the optimized atomic ratio will result unwanted 3D growth as shown in the RHEED image in Figure 2-6. The second important parameter pair is the Bi and Sb flux. The Bi-to-Sb ratio will not affect the crystallinity of the thin film as long as the growth is in 2D mode, but it can control the material's Fermi level and its carrier type. More details will be discussed in the session regarding realizing quantum anomalous Hall effect in Cr-doped TI thin films. The third parameter is the Cr flux during the growth. The purpose of Cr in our study is to introduce ferromagnetism into the TI system while keeping TI's topological property. Generally speaking, high Cr-doping usually results higher Curie temperature, larger coercive field and hole-type doping while low Cr-doping usually gives lower defect density and stronger superparamagnetic behavior at low temperature. To serve different study purposes, we actively adjust our Cr flux to create TI with different doping levels or even selective doping at different positions to create unique elemental depth profile.

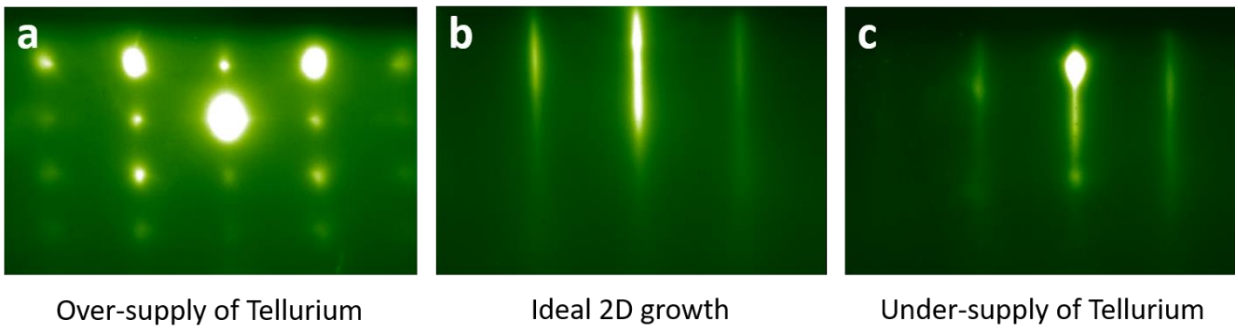

Figure 2-6 Tellurium flux's effect on TI growth. (a) Over-supply of Te will form Te clusters on the crystal surface. RHEED will show 3D pattern. (b) Ideal Te flux will result 2D growth. (c) Under-supply of Te also generates 3D pattern overlapped on 2D TI's pattern.

The as-grown material is characterized by the atomic force microscope and the transmission electron microscope (TEM) to acquire key crystal quality information regarding the thin film as shown in Figure 2-7. The AFM image usually shows atomically flat surface of TI with single QL islands sitting on top of it for good growth. Such island is unavoidable in layer-by-layer growth mode where nucleation of new TI island can happen at any time and any location during the growth. Figure 2-7(b) shows a high angle annular dark field (HAADF) scanning transmission electron microscopy (STEM) image of the cross-section of the Cr-doped $(BiSb)_2Te_3$. The lighter GaAs atoms show typical darker color as compared to heavier elements in TI due to the atomic mass correlation of such technique. The thin film's crystal shows clear quintuple-layer structure consisting of 5 layers of atom stacking together. The TEM image also shows a clear van der Waals gap in between neighboring QLs. The colored electron-dispersive x-ray (EDX) scan of the cross-section shows a uniform Cr doping throughout the whole structure without obvious clustering or phase segregation.

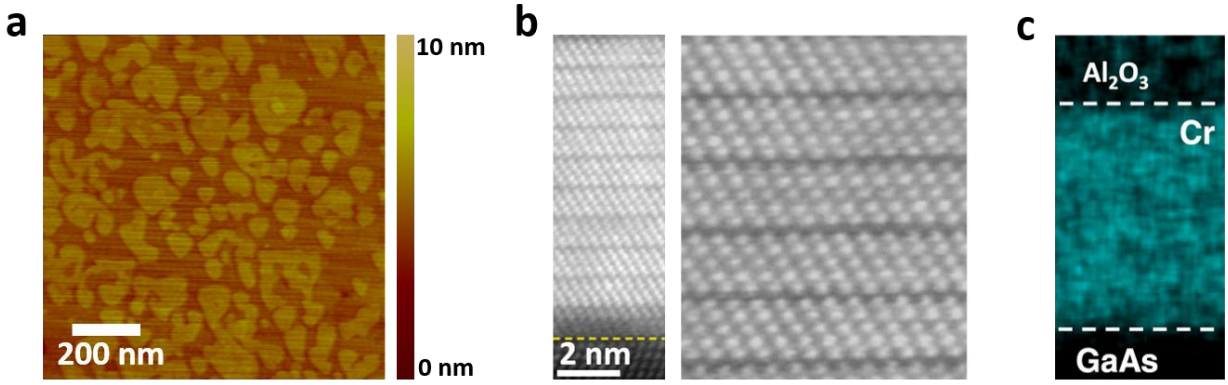

Figure 2-7 Microscopic image of TI grown on GaAs. (a) Atomic force microscopy image of Cr-doped $(BiSb)_2Te_3$ grown on GaAs. (b) HAADF-STEM image of the cross-section of Cr-doped $(BiSb)_2Te_3$. (c) EDX spectroscopy of Cr atom inside the TI structure. Adopted from Ref. [46].

To sum up, the TI and Cr-doped TI on GaAs growth using the MBE technique is the foundation throughout my study because of its high reproducibility and superior quality over other substrates. It enables accurate Cr doping control and Fermi level control which is the key to access the quantum anomalous Hall states in this material.

2.3. MBE growth of TI on Mica

Muscovite mica with a stoichiometry of $KAl_2(Si_3Al)O_{10}(OH)_2$ is a layered material that is commonly used for van der Waals epitaxy[47-49]. It is highly insulating which facilitates epilayer's transport study. In the meantime, mica substrate is highly transparent and flexible which can be an advantage to study epilayer's optical property as well as its strain response. The cleaved mica surface is atomically flat and in hexagonal symmetry[50, 51]. The key advantage of mica over other semiconductor substrate is the ability to control its thickness before growth. Utilizing mica's dielectric property, we may use the substrate as a back-gate to tune the Fermi level of the thin film without any further fabrication procedures. The challenge here is to cleave the mica to thin enough so that the epilayer can be effectively tuned with a reasonable back-gate voltage.

We start the work by establishing a good TI growth recipe on thicker mica. Mica substrate is first glued to a piece of silicon substrate using melted indium. Then we use scotch tape to remove the top few layers of the material and expose the fresh surface. After ultrasonic cleaning by acetone to remove any organic residual during the cleaving process, the silicon wafer with mica on it is then glued onto the substrate holder. After loading the sample into the growth chamber, 500 °C thermal cleaning is conducted for half an hour. The growth temperature for Bi_2Te_3 based TI on mica is also at 200 °C. During the first 300 seconds of the MBE growth, electron gun of the

RHEED system is kept off to avoid any charging effect on the insulating substrate. The as-grown material shows atomically flat surface as shown in the atomic force microscopy image in Figure 2-8. The TEM image shows clear boundary between the two layered materials with very good crystallinity on both sides.

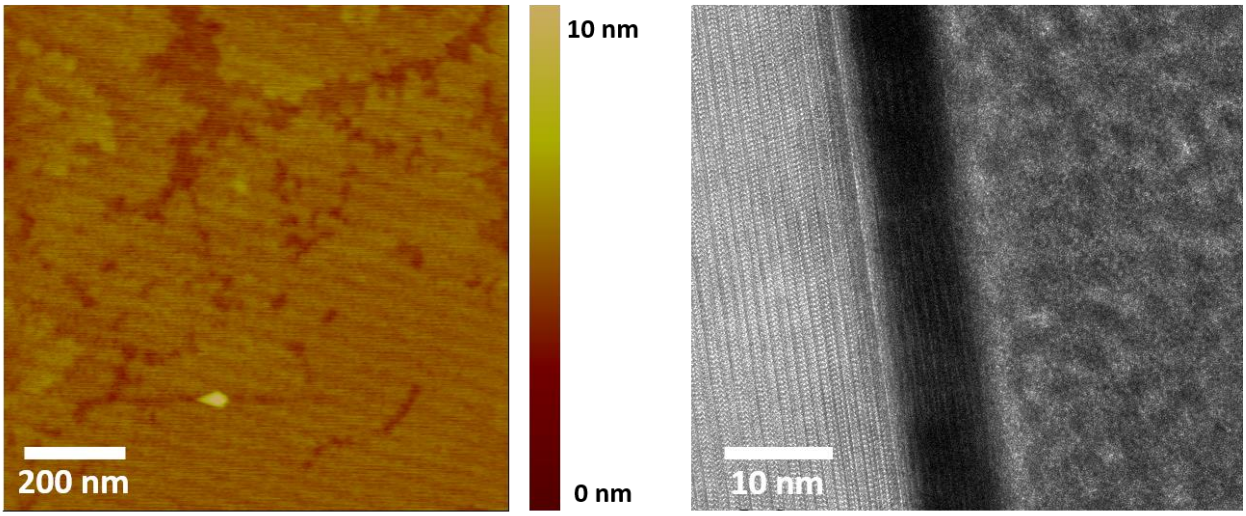

Figure 2-8 Microscopic image of Bi_2Te_3 TI family grown on mica substrate. Left: Atomic force microscopy image of Bi_2Te_3 grown on mica substrate. Right: TEM image of Cr-doped $(BiSb)_2Te_3$ on mica substrate.

We further carried out HRSTEM and EDX mapping of the entire structure as shown in Figure 2-9. The result is very similar to our Cr-doped $(BiSb)_2Te_3$ grown on GaAs substrate shown in reference [23]. The magnetically doped TI shows clear van der Waals layered structure. The Cr-doping in the structure is uniformly distributed as well as other elements that constitutes the TI. We do observe additional aluminum and oxygen signals on both the top of TI and at the bottom of TI. On top of the TI, the aluminum and oxygen signal come from the aluminum capping after the TI growth. The naturally oxidized alumina contains both elements. The bottom signal comes from

the mica itself as aluminum and oxygen are both rich inside the mica. The platinum signal comes from an additional capping layer for TEM measurement.

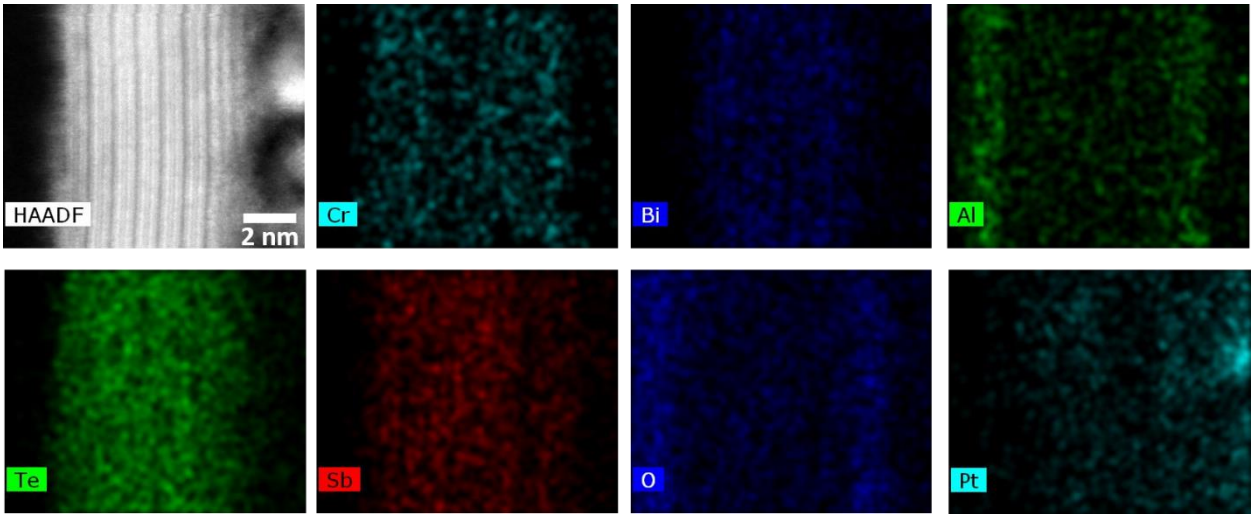

Figure 2-9 Cross-section HRSTEM and EDX of the Cr-doped $(BiSb)_2Te_3$ on mica structure. Cr, Bi, Te and Sb which constitute the magnetic TI material distribute uniformly in the structure. Al and O are seen at the bottom and the top of TI because they are part of the mica substrate and they are in the naturally oxidized Aluminum capping on top of TI.

After establishing a suitable growth recipe for TI on mica substrate, the next object is to thinner down the mica thickness. But there are quite a few challenges including: 1. How do we handle the sub-1 μm thin film considering it is mechanically unstable. 2. How to overcome the thermal stress during growth. 3. How to fabricate a back-gate device and make contact onto it without damaging it. To overcome all these challenges, we developed a fabrication procedure as shown in Figure 2-10. To strengthen the mica's mechanical robustness and prepare it for future thermal cycles, we first deposit a 100 nm tungsten layer followed by 100 nm copper as a protection layer onto the substrate. Tungsten is chosen because of its relatively matching thermal expansion coefficient with mica (mica: 3×10^{-6} m/mK, tungsten: 4.3×10^{-6} m/mK). A comparison of mica's

shape after TI growth between using non-thermal-matching material nickel (13×10^{-6} m/mK) and tungsten is shown in Figure 2-11(a). The nickel coated mica wrinkled more significantly, and the final sample was not suitable for further device fabrications, but the tungsten coated sample survived the whole process.

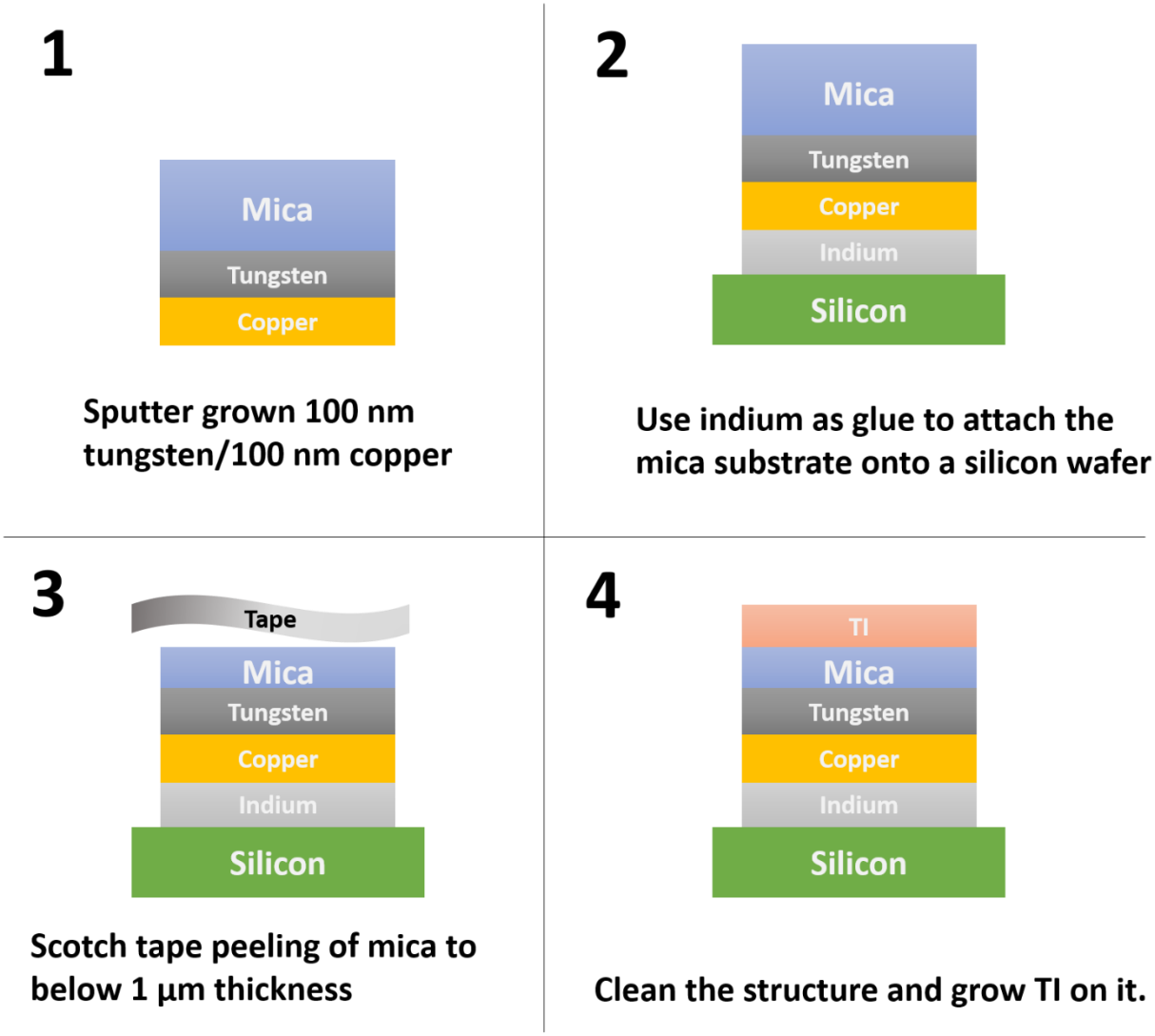

Figure 2-10 TI-Mica heterostructure fabrication process. Step 1: Tungsten/Copper sputtering to serve as a thermal-expansion-matched back electrode. Step 2: Use indium as adhesive to attach mica onto a supporting substrate. Step 3: Thin down the mica thickness using scotch tape peeling. Step 4: Clean the structure and grow TI on top of it using MBE technique.

After tungsten and copper coating, the mica substrate is glued onto the silicon wafer using indium. The third step is to peel the mica using scotch tape very similar to the cleaving of other 2D materials, for example, graphene. The peeling stops when the mica starts to show different reflection interference colors. The exact mica thickness can be determined by comparing the reflectance spectrum of the thin film and the simulation data using mica's dielectric constant (n = 1.552) as shown in Figure 2-11(b). In this case, the estimated thickness is 385 nm. With this thickness, mica is able to serve as a back-gate and effectively tune the Fermi level of the TI by applying a sub-200 V back-gate voltage.

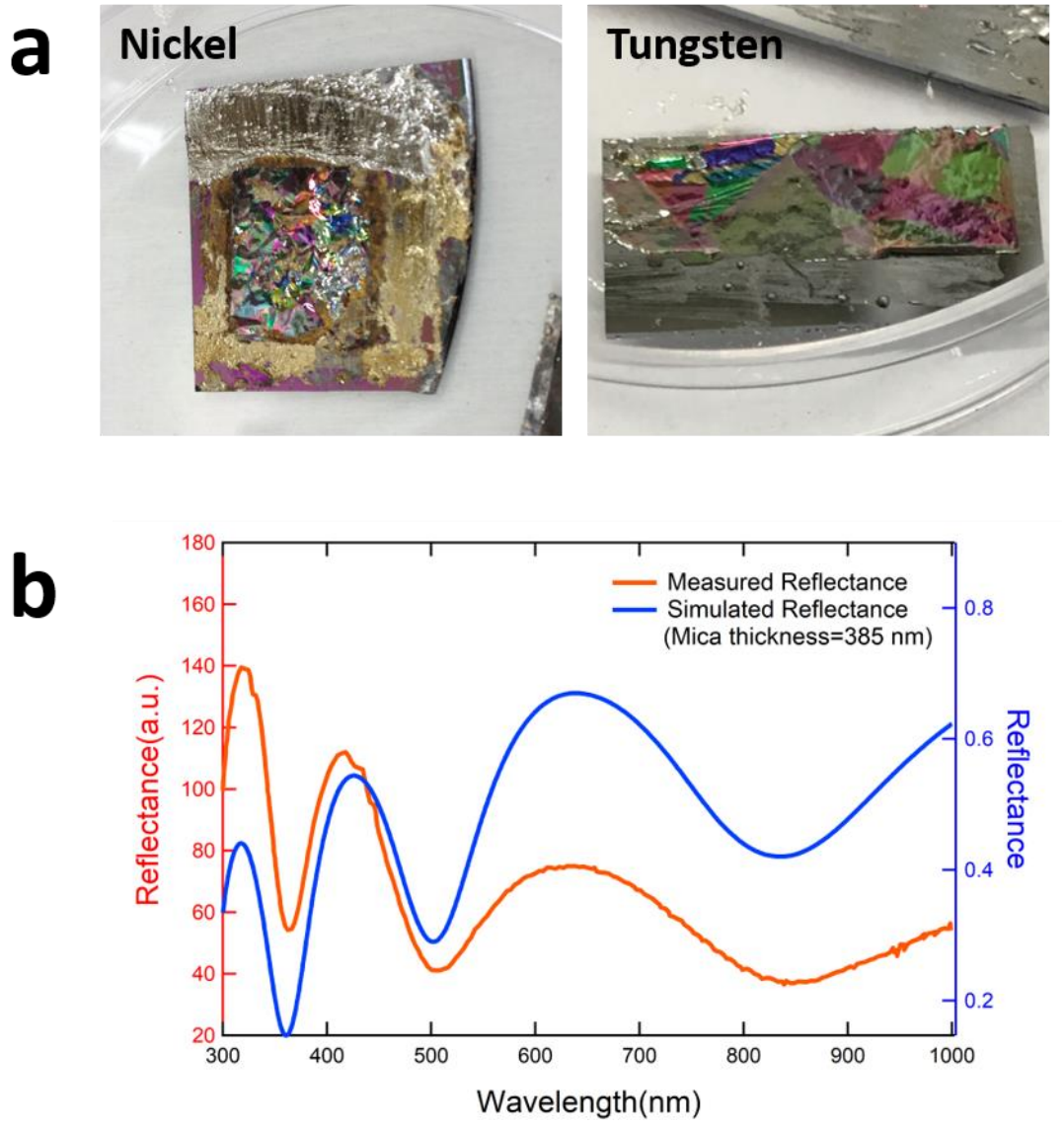

Figure 2-11 Metal coating and mica thickness measurement. (a) The nickel coated sample wrinkles more significantly than the tungsten coated one because of larger thermal expansion mismatch. (b) Measured and simulated reflectance spectrum for mica thickness estimation. By matching the peak and valley of the spectrum we can estimate this mica's thickness is around 385 nm.

After achieving this thickness, apply voltage across the mica substrate can tune the Fermi level of the TI. Here we show the Cr-doped TI/mica heterostructure's low temperature transport measurement to demonstrate the chemical potential tuning capability using mica as a back-gate.

The mica device fabrication is very challenging due to the following reasons: 1. Mica substrate is transparent which adds additional difficulty for photolithography process; 2. Ultra-thin mica substrate is very fragile which may lead to cracking during the fabrication and thus lead to electrical shorting between the device and the bottom electrode; 3. To make contact toward the device, traditional wire-bonding machine can no longer be used because the heat-assisted bonding process may penetrate the ultra-thin mica substrate and compromise its gating capability. The whole fabrication process limits the device yield, yet we are able to achieve some TI/mica devices with both top and bottom gates working. To make contact towards the electrode, a damage-free contact method was developed by creating silver epoxy droplets at the contact pads using very thin tungsten wires. Then normal aluminum wire was dipped into the droplet and baked at elevated temperature to guarantee its mechanical strength as well as the good electrical property. The fabricated device is shown in Figure 2-12.

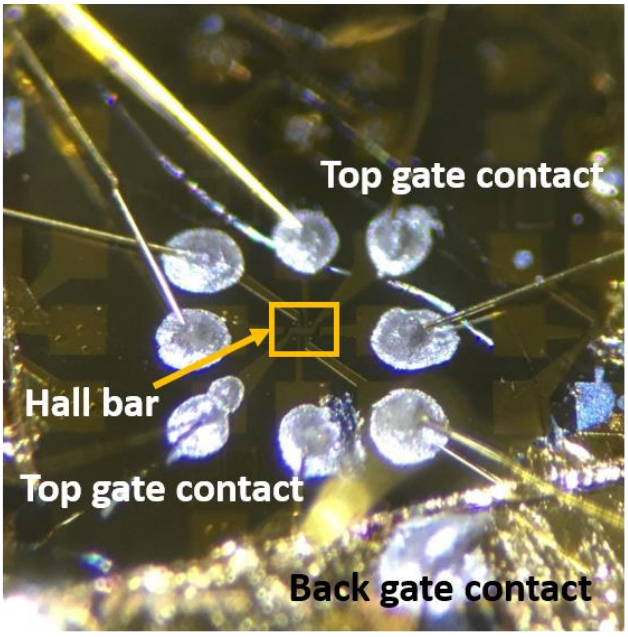

Figure 2-12 Optical microscope image of a double-gate TI/mica device.

In this sample, the TI layer is Cr-doped $(BiSb)_2Te_3$ which has pronounced anomalous Hall effect at low temperature. So, we carried out the gate response experiment all at 1.9 K in our PPMS system. Here we first show the longitudinal resistance's response to both top and bottom gates as shown in Figure 2-13(a-b). We can see that both gates can change the longitudinal resistance of the Hall-bar by a significant amount. The required voltage at the back-gate is much larger than the alumina top-gate because of the gate thickness difference (10 nm for the top gate and few hundreds of nm for the bottom gate). More importantly, the Hall channel also has large gate-response towards both gates as shown in Figure 2-13(c-d). By fixing either the top gate voltage or the bottom gate voltage and tune the other, we observe a large anomalous Hall resistance change of the magnetic TI layer. The anomalous Hall resistance in this material system is very sensitive towards the Fermi level position which will be discussed more in details in Chapter 3. Here the major achievement of this work is the successful fabrication of a working double-gate TI device on a widely available substrate.

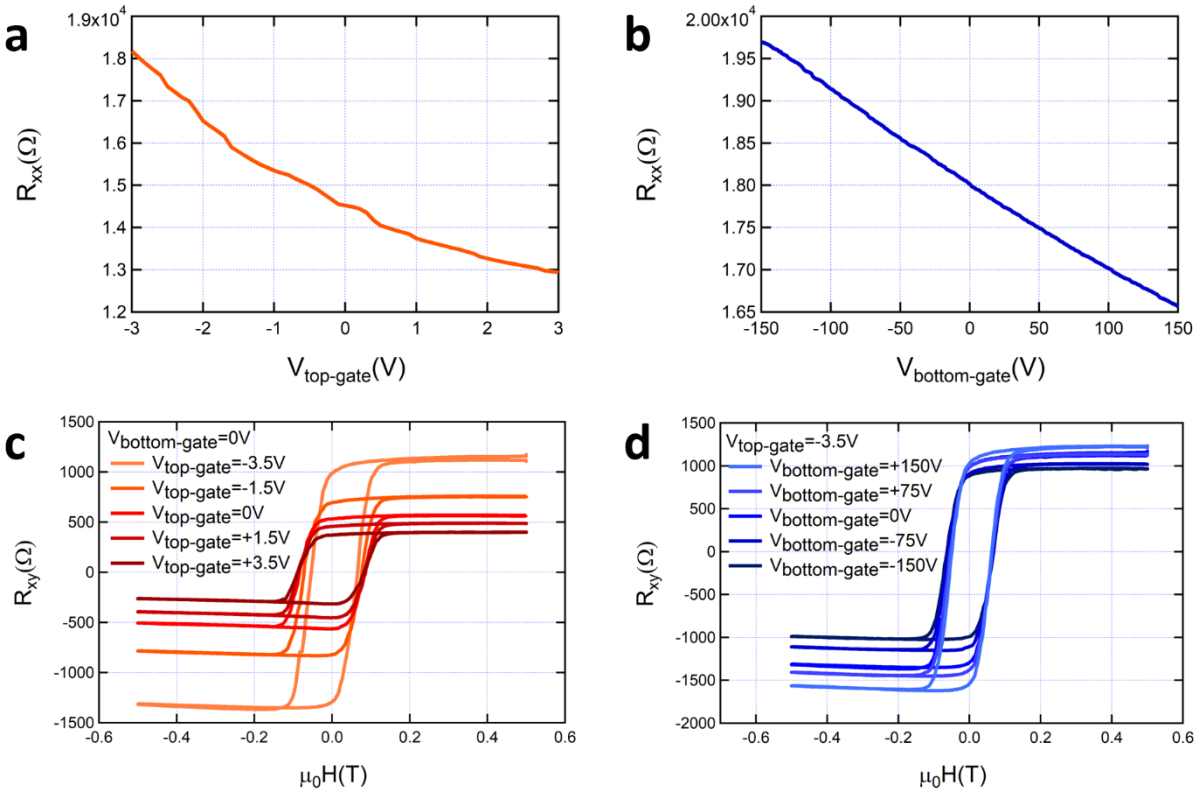

Figure 2-13 Top and bottom gate response of the Cr-doped TI/Mica heterostructure. (a) Top-gate response of the longitudinal resistance of the magnetic TI. (b) Bottom-gate response of the longitudinal resistance of the magnetic TI. (c) Top-gate voltage dependent hysteresis loop of the magnetic TI at 1.9 K. The bottom-gate voltage is fixed at 0 V. (d) Bottom-gate voltage dependent hysteresis loop of the magnetic TI at 1.9 K. The top-gate voltage is fixed at -3.5 V.

2.4. MBE growth of antiferromagnet-TI heterostructure

Antiferromagnets (AFM) do not have macroscopic magnetization, but the short-range interfacial exchange coupling with neighboring materials does exist when couple this material with other condensed matters[28, 29, 52]. The integration of TI and AFM using the MBE technique allows atomically sharp interfacial engineering and can maximize the proximity and exchange interaction between the two material systems. The magnetic interaction and its resulted

modification of the topological surface states brings enormous opportunities to studying TI in an exchange coupled system. In the next two sub-sections, we study the growth and preparation of two AFM-TI heterostructures. One is the Cr_2O_3-TI heterostructure, the other is the CrSe-TI heterostructure.

2.4.1. Cr_2O_3-TI heterostructure

Cr_2O_3 is a well-studied antiferromagnetic (AFM) material with Néel temperature (T_N) around 300 K[53]. Its crystal structure is very similar to sapphire and is usually grown on sapphire substrate using MBE or sputtering technique[54-56]. Looking along the [0001] direction of the Cr_2O_3 lattice, it is also in hexagonal symmetry which is suitable for TI growth. The spin structure of Cr_2O_3 is also along the [0001] orientation which is parallel/anti-parallel to magnetic TI's out-of-plane magnetic anisotropy. The detailed crystal and spin structure of the Cr_2O_3 lattice is shown in Figure 2-14. Besides its AFM property, Cr_2O_3 is also a magnetoelectric material in which a boundary magnetization can be induced and manipulated through a combination of external electric and magnetic field[57]. This property, if properly utilized, may realize the electrical manipulation of AFM's adjacent exchange-coupled ferromagnetic material. The coupling of electrically controlled boundary magnetization with the topological surface states as well as TI's magnetic order may also be interesting.

The Cr_2O_3 in our experiment was grown using MBE technique on sapphire(0001) substrate with a thickness ranging from 40 to 1000 nm. To verify the crystal quality, HAADF-STEM was performed at the boundary between sapphire and Cr_2O_3. The interface is atomically sharp with clear epitaxy signature. To confirm its antiferromagnetism, temperature-dependent neutron diffraction on the magnetic (10-12) reflection of the Cr_2O_3 film was performed using the SPINS

instrument at the NIST Center for Neutron Research within a temperature of 125 K to 350 K. The result is shown in Figure 2-14(c). By fitting the temperature-dependent curve (shown in Figure 2-14(d)), we are able to determine the thin film's T_N to be 297.3 K ± 0.3 K which is in good agreement with its bulk form.

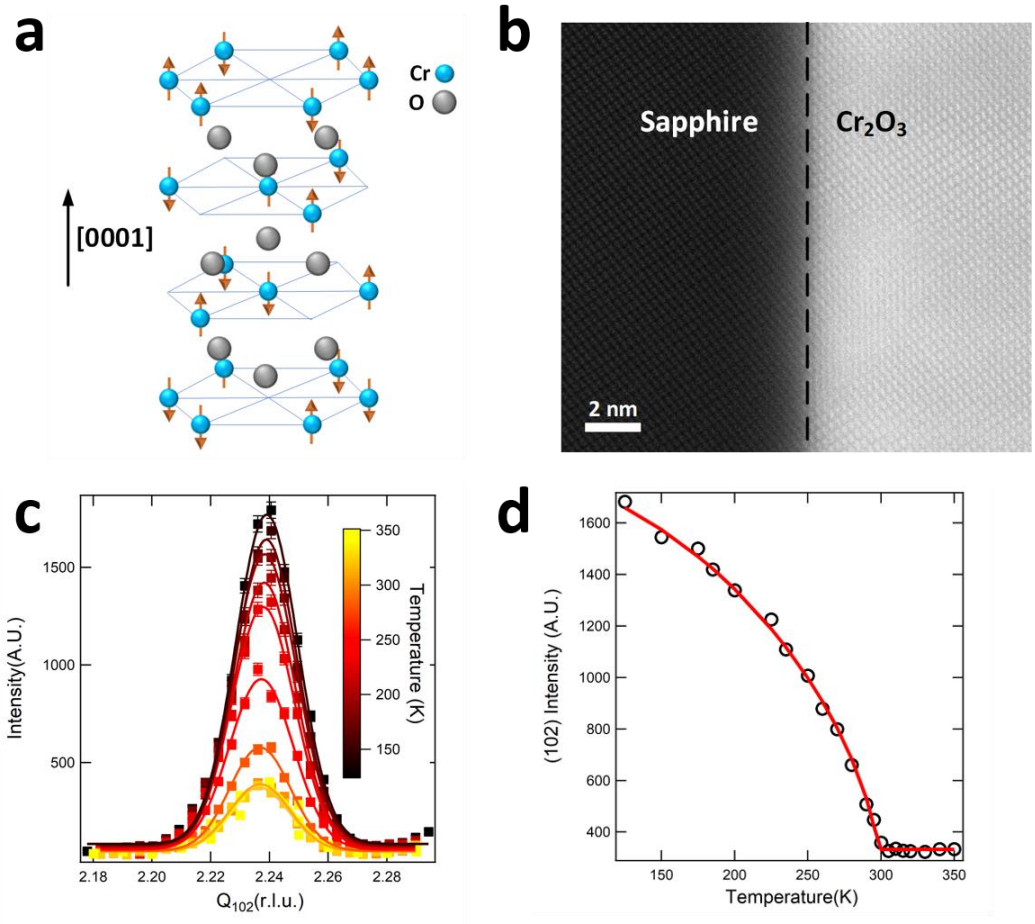

Figure 2-14 Magnetic and crystal property of Cr_2O_3 grown on sapphire(0001) substrate. (a) Crystal and magnetic structure of antiferromagnet Cr_2O_3. (b) HAADF-STEM of the Cr_2O_3/sapphire interface. (c) Neutron Diffraction measurement of the Cr_2O_3 (102) peak in the temperature range from 125 K to 350 K. (d) fitted temperature-dependent peak height suggests a TN around 300 K.

The TI growth on the Cr_2O_3/sapphire substrate was performed in our Perkin-Elmer MBE chamber. The substrate will first be cleaned ultrasonically with acetone followed by 500 °C thermal annealing in the growth chamber for 30 minutes. The growth temperature of TI on Cr_2O_3 is at 200 °C and the quality of the TI is monitored by RHEED and later characterized by HAADF-STEM as shown in Figure 2-15. The HRSTEM-EDX image shown in Figure 2-15(c) also shows clear boundary with no inter-diffusion between TI and Cr_2O_3. The sharp interface achieved is essential for later studies on the exchange coupling effect between the AFM order in Cr_2O_3 and FM order in magnetically-doped TI thin films.

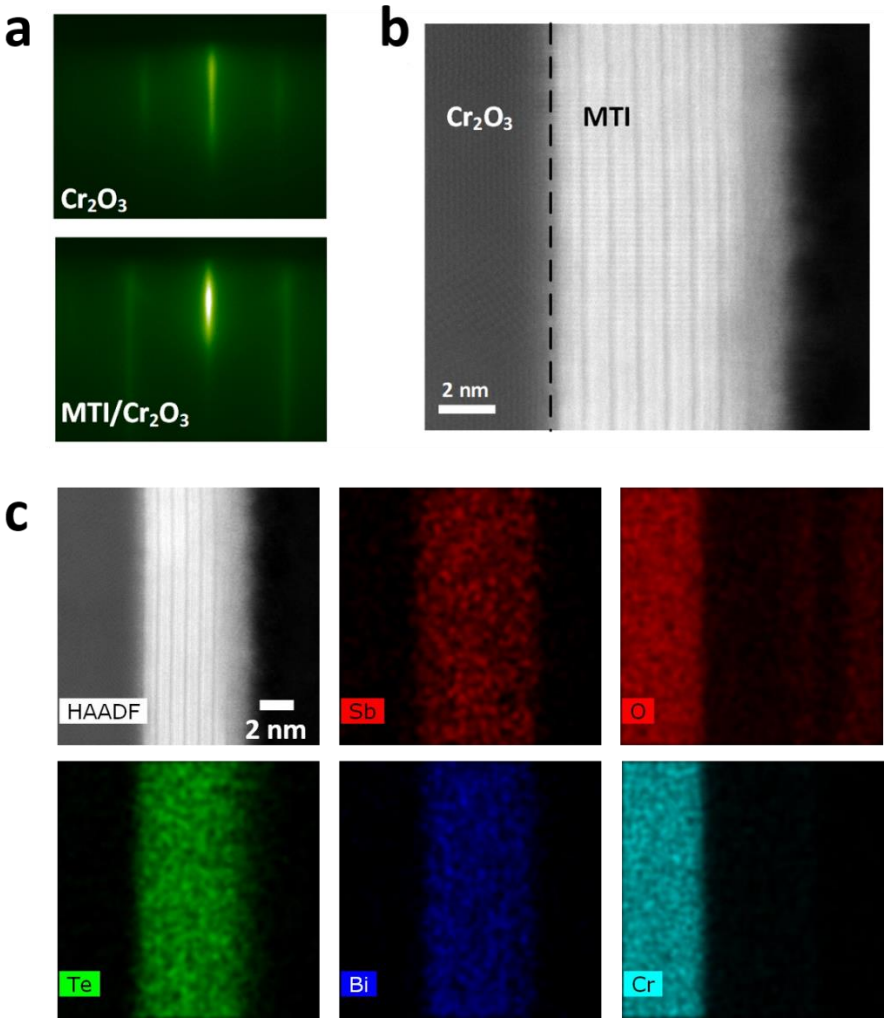

Figure 2-15 Structural characterization of Cr-doped TI grown on Cr_2O_3. (a) RHEED pattern of Cr_2O_3 and magnetically-doped TI grown on Cr_2O_3. (b)HAADF-STEM image of MTI-Cr_2O_3 bilayer structure. (c) HAADF-STEM-EDX image of MTI-Cr_2O_3 bilayer structure.

2.4.2. CrSe-TI heterostructure

CrSe is an AFM material with hexagonal NiAs-phase as shown in Figure 2-16(a). Its magnetic structure is rather complicated. Neutron scattering studies suggest that a non-collinear antiferromagnetic order that features an umbrella-like AFM texture at two sub-lattices. At each

basal plane, the magnetic order tilts out-of-plane with a component along the [001] or the opposite crystal orientation and can cancel each other between adjacent layers[58]. Its lattice constant in the (001) plane is 3.67 Å [58] which is around 8% mismatched to GaAs(111)B lattice. To incorporate such large lattice mismatch and to ensure good thin film quality, we adopted two strategies. The first one is by limiting the thickness of the CrSe layer on GaAs and the second is by using a two-step growth method. To grow CrSe on the GaAs(111)B substrate, we first use the same method that has been discussed in the previous section to pre-anneal the GaAs substrate and lower the temperature down to 200 °C. The first layer of CrSe is grown at this temperature and the growth lasts for 600 seconds with a growth rate at 2 Å/minute. After the first 2 nm of CrSe growth, the substrate temperature will be raised to 400 °C and be maintained at this temperature for the following growth. For most of our samples, the CrSe thickness is limited to below 10 nm. After the two-step growth, the RHEED of CrSe shows bright streaky pattern and follows the hexagonal structure of GaAs(111)B. The quality of the CrSe thin film is verified by STEM, neutron diffraction and X-ray diffraction (XRD) as shown in Figure 2-16. The interface between substrate and CrSe is atomically sharp with clear epitaxial relationship. The neutron diffraction of 201 and 200 magnetic peaks in CrSe indicate the material's Néel temperature to be around 273 K which agrees well with the bulk data[58]. The XRD confirms the NiAs crystal structure of our CrSe thin film and estimates the lattice constant to be 3.6 Å which is in close agreement with previous work[58, 59].

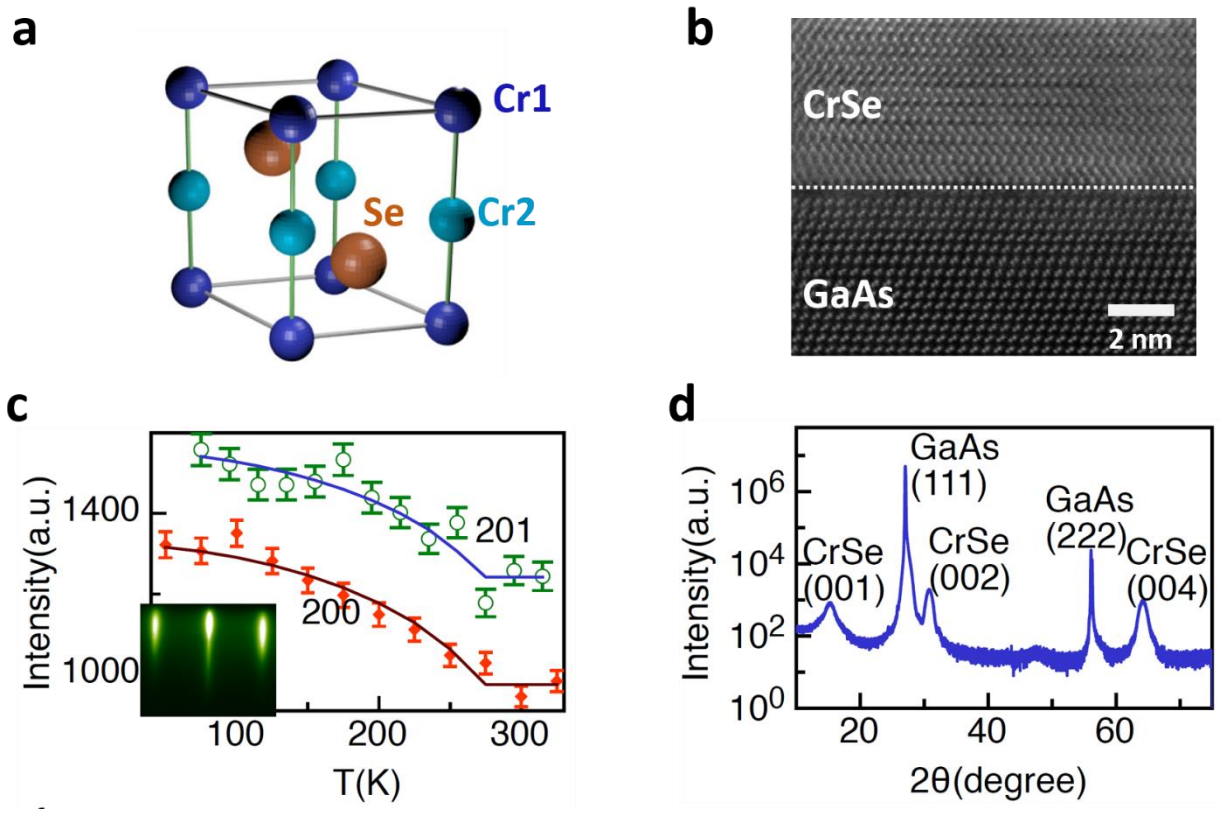

Figure 2-16 Magnetic and crystal property of CrSe grown on GaAs(111)B substrate. (a) Crystal structure of NiAs phase CrSe. (b) Cross-sectional HAADF-STEM image of CrSe grown on GaAs. (c) Temperature dependent neutron diffraction of the 201 and 200 magnetic peaks of CrSe indicating a Néel temperature around 273 K. The inset shows the RHEED image of CrSe after growth. (d) XRD data of the CrSe thin film grown on GaAs shows the NiAs phase of it.

TI growth on CrSe is similar to the growth on GaAs substrate. The growth temperature is also at 200 °C. The lattice mismatch is larger but the unique van der Waals structure of TI can effectively relax the strain and promotes 2D epitaxial growth. However, to grow CrSe on TI is harder because it is no longer van der Waals epitaxy growth and the sublimation temperature of TI (around 300 °C) is also too low to conduct two-step growth. The optimized substrate growth temperature is around 250 °C and the thickness of the CrSe layer is limited to below 6 nm. In

Figure 2-17, we show a trilayer structure where a TI layer is sandwiched in between two CrSe layer (top layer 3 nm in thickness, bottom layer 5 nm in thickness). From the EDX mapping we can see that the element inter-diffusion is well-controlled especially the Cr atoms that are confined only in the AFM layer. The interface qualities between the two surfaces are comparable but later study with isolated TI-CrSe surfaces revealed interesting AFM proximity effect that is related to the stacking order of TI and CrSe.

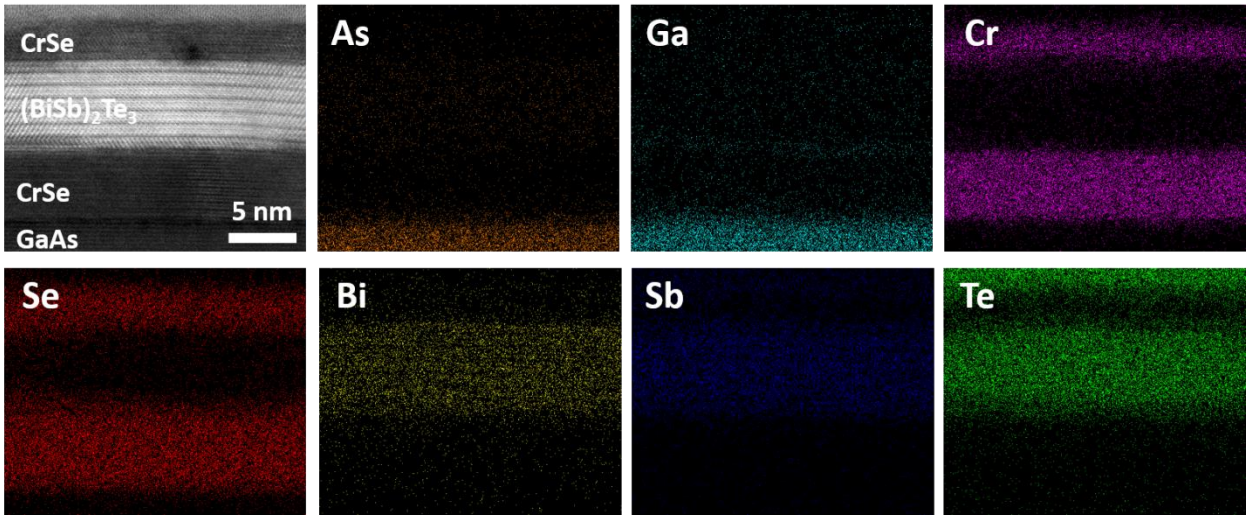

Figure 2-17 Cross-sectional HAADF-STEM-EDX image of the CrSe-$(BiSb)_2Te_3$-CrSe trilayer structure. The two CrSe-$(BiSb)_2Te_3$ are all atomically sharp. All elements are confined within their own material systems with no obvious inter-diffusion.

2.5. Summary of Chapter 2

In this chapter, we introduced the fundamentals of MBE which is the key equipment for our study. We demonstrate the thin film growth capability of our MBE system including TI on GaAs substrate, TI on mica substrate and TI-antiferromagnet heterostructures. The TI on GaAs growth has the best epilayer quality among all the substrates and later plays an important role in

realizing the quantum anomalous Hall effect without additional gate tuning in our magnetically doped TI thin films. The TI on mica substrate growth provides great insight in terms of how to realize a double-gate TI device on a widely available substrate. Beyond that, the van der Waals epitaxy process also provides great TI quality. We also investigated the possibility of integrating high quality TI thin films with AFM Cr_2O_3 and CrSe. On the Cr_2O_3 substrate, TI with similar quality as the growth on GaAs substrate can be achieved which facilitates the first observation of quantum anomalous Hall effect on a magnetic substrate that will be covered in Chapter 4. For CrSe which can be grown in our MBE chamber, we achieved heterostructures including both CrSe and TI with different stacking orders. This achievement later helped us reveal the unique interface dependent magnetic proximity effect which will also be covered in Chapter 4.

Chapter 3

Quantum anomalous Hall effect

As introduced in chapter 1, quantum anomalous Hall effect is the zero-external-field version of the quantum Hall effect. At quantization temperature, dissipationless chiral edge states emerge at the sample boundary. Reflected in the transport signal, quantized Hall resistance and near-zero longitudinal resistance show up when the sample is in the quantized state. The first working material system to achieve the QAH effect was proposed in 2010 [24] and experimentally realized in 2013[35]. Thus far, the magnetically doped 3D TI system remain as the only material system that can demonstrate the QAH effect. This is no surprise to experimentalist because of the strict combination of requirements that must be met to realize the QAH effect including a robust out-of-plane ferromagnetic order, a non-zero first Chern number and a large bulk bandgap with Fermi level sitting inside of it. Since the first observation of the QAH effect, multiple research groups including our UCLA group are able to reproduce the similar transport signature in Cr-doped TIs[46, 60, 61]. In our study, we demonstrate the first QAH insulator grown on GaAs substrate without gate tuning of the Fermi level. The Fermi level of the as-grown magnetic TI was positioned inside both the bulk band gap and the surface gap through composition tuning as introduced in Chapter 2. Beyond the previous report which only shows the QAH effect at the 2D limit of the system, we demonstrate the QAH effect in the 3D regime and in macroscopic scale. Through precise control of the sample thickness, we also discovered a metal-to-insulator transition behavior towards the 2D limit of the magnetic TI. Lastly, we investigated the temperature limiting

factors of the QAH effect in current magnetic TI material systems using transport and optical method.

3.1. Scale-invariant quantum anomalous Hall effect

In the first report of the observation of the QAH effect in magnetic TI systems[35], the 5 QLs TI thin film was grown on $SrTiO_3$ substrate to facilitate the back-gating utilizing $SrTiO_3$'s giant dielectric constant at cryogenic temperature. It was then hand-scratched into a μm-sized Hall-bar structure to conduct the transport measurement. Though back-gate adds more flexibility in terms of initial Fermi level positioning for the as-grown materials, it also brings more complexity and limits the substrate choice. An as-grown QAH insulator with Fermi-level positioned at charge-neutral point (*i.e.,* the bulk conduction is minimized) is highly preferred.

As introduced in Chapter 2, we prepared our magnetically-doped TI on GaAs(111)B substrate. Through careful composition tuning of the Cr:Bi:Sb ratio for our Cr-doped $(Bi_xSb_{1-x})_2Te_3$ growth, we were able to optimize it to charge neutral point where no additional gate-tuning is required to achieve the QAH effect. The TI's chemical composition determined using EDX is $Cr_{0.24}(Bi_{0.3}Sb_{0.7})_{1.76}Te_3$. The thickness of the TI thin film is 10 QLs confirmed by monitoring the RHEED oscillation period as shown in Figure 3-1(a). At this thickness, the TI is no longer in the 2D limit which is different from the first QAH effect observation. To minimize the possible damage towards the TI thin film, the device fabrication process was also minimized: a milli-meter sized Hall-bar mask was first attached to the surface of the as-grown thin film followed by a single-step CHF_3 dry etching with an etching rate around 1 nm/sec. The Hall-bar device is shown in Figure 3-1(b) with an active region at the size of 2 mm × 1mm.

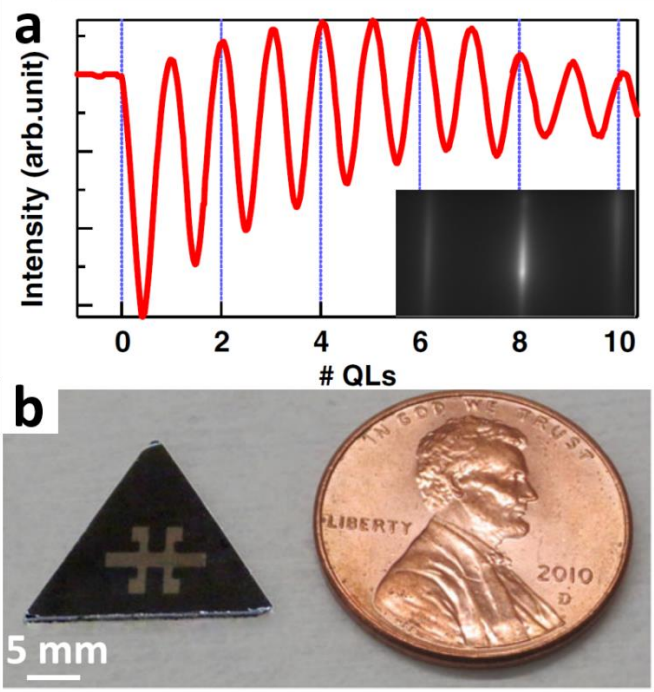

Figure 3-1 RHEED oscillation and real device image of the QAH sample. (a) RHEED oscillation indicating the TI thin film thickness of 10 QLs. Inset: RHEED image of the TI thin film. (b) Image of a 2 mm × 1 mm Hall-bar device fabricated using single-step dry etching method. Adopted from Ref. [46].

Six indium contacts were soldered onto the Hall-bar leads to allow the longitudinal and Hall resistivity measurement. The sample's transport property was first measured at 1.9 K in our PPMS system as shown in Figure 3-2. The coercive field showed up at around 30 K which is consistent with our group's previous study in Cr-doped TI systems because of the similar Cr doping levels[23]. The Hall resistance has already reached 7 kΩ a 5 K which is around 27% of the quantized value (i.e., 25.8 kΩ) as shown in Figure 3-2(a). The longitudinal resistance showed typical two peaks when magnetization reversed as shown in Figure 3-2(b).

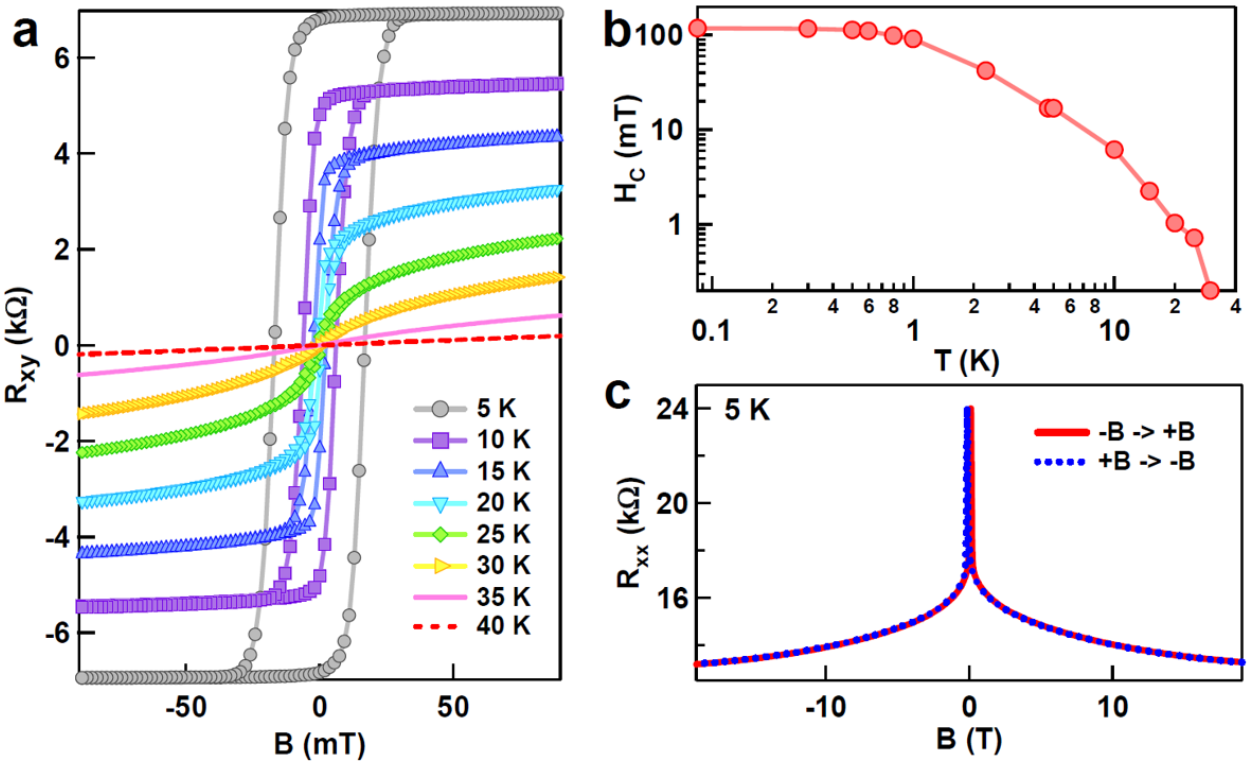

Figure 3-2 PPMS transport measurement of the magnetic TI thin films. (a) Hall resistance measurement from 5 K to 40 K. (b) Temperature dependent coercive field size of the thin film. (c) External magnetic field dependent longitudinal resistance measured at 5 K. Adopted from Ref. [46].

After verifying the sample quality, the magnetic TI Hall-bar device was loaded into a dilution fridge with the capability of cooling samples down to below 100 mK. Theoretically, the chiral edge state in the QAH regime only flows at the edge of sample with its chirality determined by the magnetization of the TI sample as shown in Figure 3-3(d). Such kind of chiral transport signature indeed showed up at 85 mK as shown in Figure 3-3. The first signature is that anomalous Hall resistance successfully reached the quantized value at 25.8 kΩ as shown in Figure 3-3(a). The longitudinal resistance also dropped to below 3 kΩ. Ideally, this value should drop to a near-zero value depending on the activation energy gap of the QAH states as well as the temperature. This

non-zero longitudinal resistance will be discussed more into details later. At a different thickness of 6 QLs as shown in Figure 3-3(c), we also observed the QAH effect at 85 mK showing that the QAH effect can be achieved in the same material system both in 2D and 3D regime.

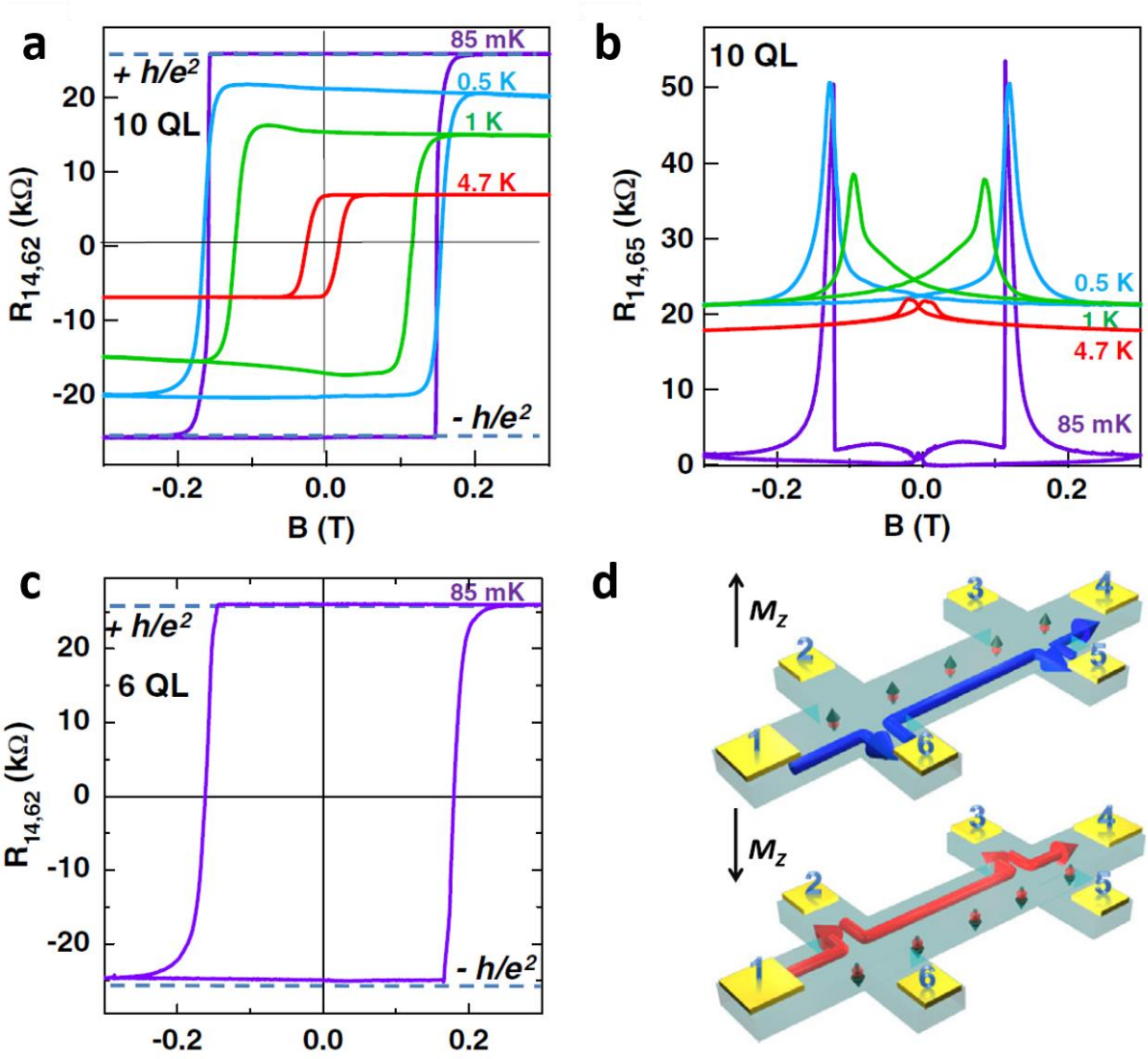

Figure 3-3 Observation of the QAH effect in 10 QLs magnetic TI at 85 mK. (a) Temperature dependent hysteresis loop of anomalous Hall resistance. The anomalous Hall resistance reached quantized value at 85 mK. (b) Temperature dependent longitudinal resistance. (c) A 6 QLs magnetic TI sample reached quantization at 85 mK. (d) Schematics of the chiral edge conduction

in the QAH regime. The current flows from contact 1 to contact 4, and the magnetization of the Cr-doped TI film is along the z-direction. Adopted from Ref. [46].

When the anomalous Hall resistance reached the quantized value as temperature was lowered down to below 100 mK, we noticed the longitudinal resistance also showed a decreasing trend as shown in Figure 3-4(a). Such residual resistance in the QAH regime was first reported in the first observation of the QAH effect in 5 QLs magnetic TI samples[35]. However, in that experiment, when a large external magnetic field was applied (B >10 T), this residual longitudinal resistance diminished to almost zero and the system was driven into a near-perfect dissipationless state. In contrast, when a large external field (up to 15 T) was applied to our 10 QLs magnetic TI samples, the residual longitudinal resistance did not disappear. Instead, the resistance remained at 3 kΩ over a large magnetic field range as shown in Figure 3-4(b). Obviously, the origin of the dissipative conduction in our 10 QLs magnetic TI is different from the 5 QLs report because of the very different magnetic field response. In the meantime, this dissipative term cannot be simply attributed to the trivial bulk contribution because of the lack of parabolic response which is commonly seen in metallic systems. One possible origin of this dissipative term in 3D TI regime is the side surface conduction. In the QAH regime, the top and bottom surfaces of the TI are fully gapped because of the out-of-plane magnetization. However, such magnetization direction cannot open gaps at the side surface in which case the side surface conduction is not chiral and can be dissipative. In the later study, we conducted a systematic thickness dependent study of the QAH effect and revealed that this dissipative term might have sample and measurement dependence. And in thicker magnetic TIs, the dissipative term mostly comes from the bulk band involvement.

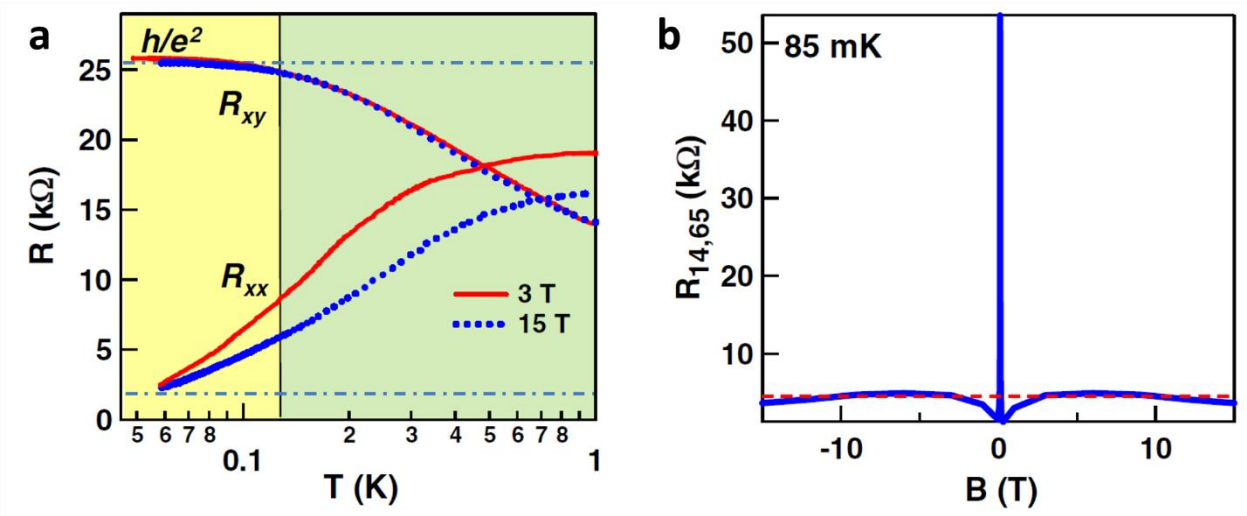

Figure 3-4 Nonzero longitudinal resistance in the 10 QLs QAH system. (a) Temperature-dependent longitudinal and Hall resistance of the thin film under constant out-of-plane field B = 3 T and 15 T. (b) Magnetic-field-dependent longitudinal resistance up to 15 T. The longitudinal resistance shows little field dependence when B is larger than 3 T. Adopted from Ref. [46].

A more careful low temperature measurement was conducted on this 10 QLs magnetic TI sample by our collaborators[62]. At both positive and negative magnetization, the thin film was zero-field-cooled down to base temperature as shown in Figure 3-5(a). The tracking of the longitudinal conductivity σ_{xx} versus reciprocal temperature provides the thermal activation energy of the system. This extrapolation is used as a fitting guide to better know the thin film temperature rather than relying on the cryostat thermometer reading which might not reflect the true sample temperature. To achieve the best quantization value, instead of a constant rate magnetic field scanning at the base temperature, a demagnetization cooling cycle was applied. The detailed steps are described as follows and illustrated in Figure 3-5(b): Starting from zero external field and positive TI magnetization, the field was then slowly increased followed by a long wait (> 2 hours).

This step allows maximal thermal equilibration between the sample and the cryostat. Then a fast field magnitude decrease was performed to produce an adiabatic demagnetization effect which further cooled the sample down. The temperature showing in Figure 3-5(b) which is the inferred temperature extrapolated using Figure 3-5(a) cooled to 25 mK using this process. The residual longitudinal resistance was driven to as low as 2 Ω. A long re-equilibration is also included after reaching the lowest temperature and the thin film slowly warmed up to 40 mK.

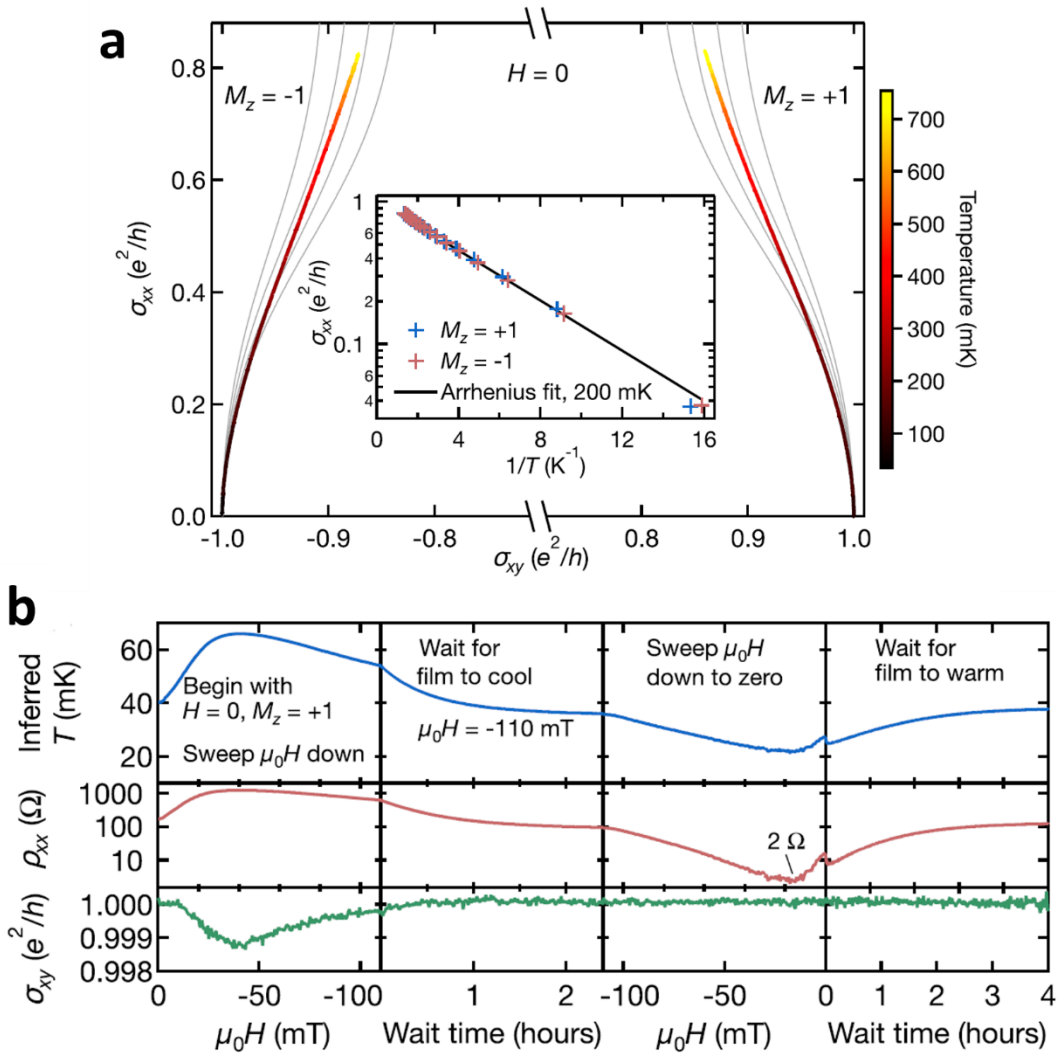

Figure 3-5 Temperature dependent longitudinal conductivity and adiabatic demagnetization cooling. (a) Temperature dependent zero-field cooling at two magnetization status of the TI thin

film. Inset: an Arrhenius plot of σ_{xx} as a function of inverse temperature. (b) A demagnetization cycle involving a slow field sweep to magnetize and a fast field sweep to zero to perform demagnetization cooling. Adopted from Ref. [62].

3.2. Metal-to-insulator transition in quantum anomalous Hall insulator

In the quantum Hall system, the tuning of the chemical potential across different Landau levels accompanies the quantum phase transition. Reflected in the transport signal including the longitudinal conductivity σ_{xx} and the Hall conductivity σ_{xy}, stable points appear at (σ_{xx}, σ_{xy}) = (0, ne^2/h) where n is the Landau level index. These stable quantized states are connected in a continuous semicircular trajectory during transitions[63, 64]. When the perpendicular external magnetic field is large enough to shift the ground Landau level beyond the Fermi level, the Quantum Hall system will be driven into a quantum Hall insulator state where the magnetoresistance diverges to an insulating regime when the temperature approaches absolute zero, but the Hall resistance remains finite and quantized.

In the case of the QAH effect, Wang *et al.* applied a microscopic network model of quantum percolation to investigate the universal scaling of the QAH effect plateau transition around the coercive field[65]. In the QAH regime, the quantized resistance reflected in the Hall channel and the near-zero resistance reflected in the longitudinal channel is a result of TI's non-trivial bandstructure and the exchange surface gap due to magnetic TI's out-of-plane ferromagnetic order. Combining these two together, a 3D magnetic TI becomes a Chern insulator with a non-zero first Chern number (C_1). C_1 is equal to ±1 in the QAH state. Additionally, by shrinking the TI thickness, the vertical quantum confinement will also change the band topology and drive the system into the $C_1 = 0$ insulating state. By precise tuning of the sample thickness, it is possible to

balance the competition between the hybridization induced insulating behavior and the exchange gap induced Chern insulator state such that the transition between normal insulator and the QAH insulator can be observed.

In this study, we carefully tuned the chemical composition of the magnetic TI grown on GaAs(111)B substrate which also allows the observation of the QAH effect without any chemical potential tuning. Specifically, the thin film thickness was fixed at 6 QLs which we found out that this value generates a hybridization surface gap m_0[66, 67]. Following the same Hall-bar fabrication and measurement schemes (shown in Figure 3-6(a)), we observed the quantization of the anomalous Hall resistance (R_{xy} = 25.8 kΩ) in this sample up to 260 mK as shown in Figure 3-6(b). A temperature-dependent magneto-resistance R_{xx} is shown in Figure xx(c). The R_{xx} value in the saturation region (B > 0.2 T) and its peak value during the magnetization reversal showed exact opposite trend when the temperature was cooled down from 13 K to 20 mK. The saturation R_{xx} continuously dropped to near-zero value as a result of dissipationless edge transport in the QAH regime. In the meantime, the R_{xx} peak value during magnetization reversal shows a diverging trend as summarized in Figure 3-6(d). Such dramatic change during the magnetization reversal at low temperature leads to a giant magneto-resistance ratio of up to 10^6% which is much larger than any value reported in different quantum Hall and quantum anomalous Hall systems[46, 60, 68, 69].

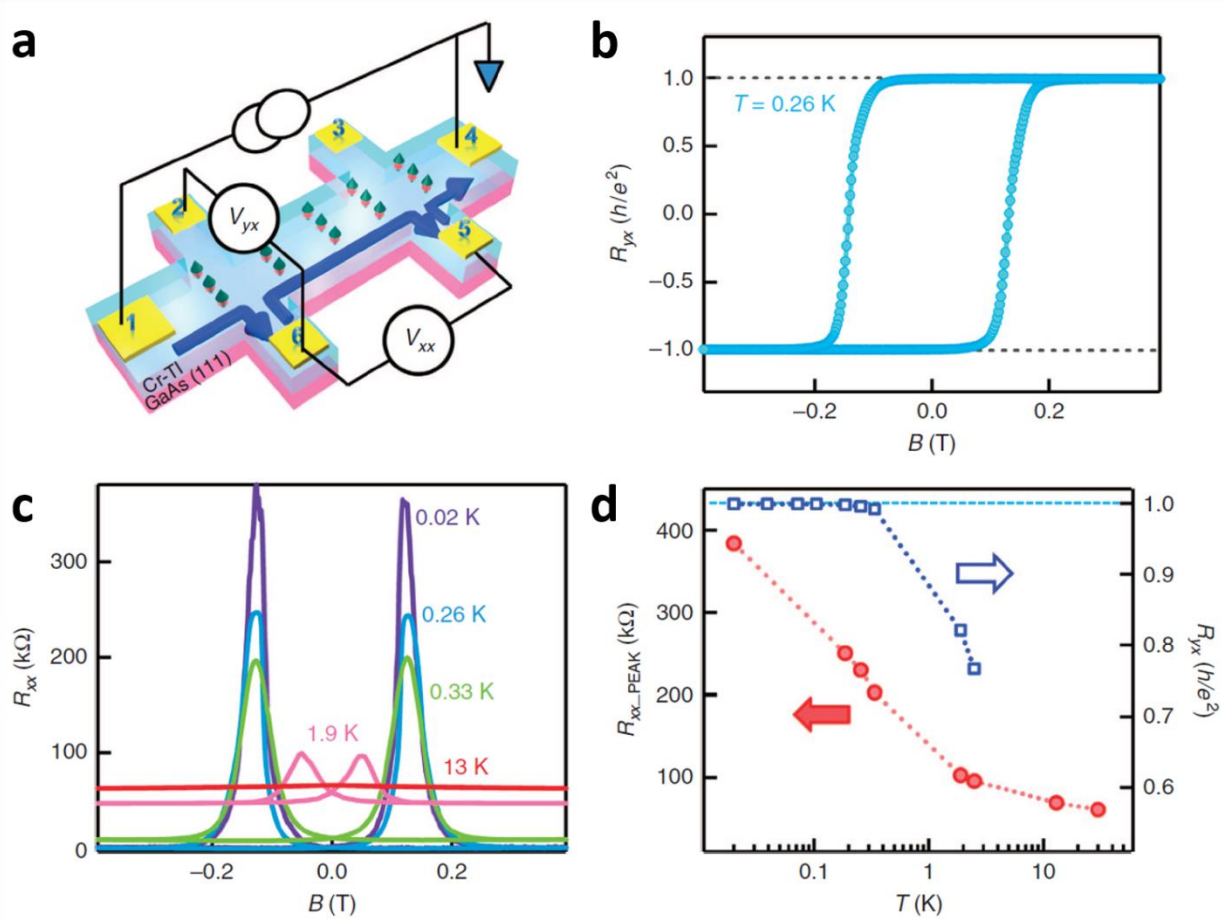

Figure 3-6 Quantum anomalous Hall effect in the 6 QLs magnetic TI thin film. (a) Schematic of the mm-sized Hall bar structure and four-point Hall measurements based on the MBE-grown magnetic TI thin film. (b) Quantum anomalous Hall results at T = 260 mK. The Hall resistances are quantized to be ± h/e^2 where the signs are determined by the chirality of the edge conduction. (c) Temperature-dependent magneto-resistance results. At the coercive fields, the peak of R_{xx} quickly diverges at lower temperatures. (d) Temperature-dependent R_{xx_PEAK} and R_{xy} extracted from Figs. 5-13(b) and (c). The anomalous Hall resistance R_{xy} becomes quantized up to 0.3 K, and the giant R_{xx_PEAK} resolved at 0.02 K is around 380 kΩ. Adopted from Ref. [70].

Such diverging behavior during magnetization reversal is a result of phase transition. To better present the transition, we performed standard resistivity to conductivity tensor conversion following the relationship below

$$\sigma_{xx} = \frac{\rho_{xx}}{{\rho_{xx}}^2 + {\rho_{yx}}^2} \ , \sigma_{xy} = \frac{\rho_{yx}}{{\rho_{xx}}^2 + {\rho_{yx}}^2} \qquad (3-1)$$

The converted result is shown in Figure 3-7(a) and (b). Two distinctive features show up in both σ_{xy} and σ_{xx} results at base temperature. In the σ_{xy} channel, instead of a direct transition between the two quantized states ($\sigma_{xy} = \pm 1\ e^2/h$), its value will go through an intermediate plateau state with $\sigma_{xy} = 0$. In the σ_{xx} channel, instead of a single peak during magnetization reversal, its value will drop to a small number right at the transition field which shares the same field position with the σ_{xy} plateau. Overall, we can summarize that during the transition between two QAH states, the QAH insulator will go through an insulating state with near-zero σ_{xy} and σ_{xx} values. Such transport behavior agrees very well with the theoretical prediction when a trivial hybridization gap is introduced into the QAH system[65]. The physics behind the QAH insulator to normal insulator transition can be explained using the multi-domain network model as shown in Figure 3-7(c). Considering the two surface-gap-generating mechanisms including the non-trivial exchange gap Δ_M due to the uniform out-of-plane ferromagnetic order and the trivial hybridization gap m_0 due to the vertical quantum confinement, in the 6 QLs magnetic TI, the m_0 is a constant. In the QAH regime, the Δ_M value is at maximum when the ferromagnetic orders are all aligned in the out-of-plane direction. In the saturation regime of our 6 QLs system, $|\Delta_M|$ is larger than $|m_0|$, so that the first Chern number of the system is ±1 which results the single chiral edge state at the sample boundary. However, during the magnetization reversal, where many upward and downward domains coexist in a random manner, the Δ_M value will decrease dramatically under the mean field approximation. When the $|\Delta_M|<|m_0|$ condition is satisfied, the first Chern number of the system will be zero meaning a trivial insulator state or we can call it the zero-Hall plateau state specifically for the QAH system.

The zero-Hall plateau behavior is not a unique feature in thin QAH insulators, in fact, this behavior was also observed in the graphene quantum Hall system[68]. It is proposed that the zeroth Landau level state in the graphene system arises from the lifting of the spin and sublattice degeneracy[71]. Even though the transport measurement also shows a diverging behavior in magneto-resistance channel at the zero-Hall plateau and a stable (σ_{xx}, σ_{xy}) = (*0*, *0*) state, the physics picture is completely different from the QAH zero-Hall plateaus. In the graphene system, high magnetic field is required to split a gap of the 4-fold degeneracy, while the trivial gap in the QAH system is fixed and is related only to the sample thickness which allows the observation of the zero-Hall plateau at small field. Moreover, the multi-domain network model is completely different from the graphene quantum Hall system which allows possible future work to engineer the zero-Hall plateau through magnetic interactions.

Beyond the zero-Hall plateau signature, as suggested by Wang *et al.*[65], we also studied the scaling behavior of the QAH plateau transition by tracing the temperature dependent σ_{xy} slope $S = (\partial\sigma_{xy}/\partial H)_{max}$ which is shown in Figure 3-7(d). The predicted relationship $S \propto T^{-\kappa}$ can only fit the data up to 100 mK with κ = 0.22 which is almost one half of the κ = 0.42 measured in the quantum Hall system[72]. The limited temperature fitting range may be due to the involvement of trivial bulk carriers into the transport signal. The difference between the QAH effect and quantum Hall effect in terms of the scaling behavior is not clear at this moment. However, it is no surprise that the two systems behave so differently in details. One key difference between the two is the "cleanliness": the magnetic TI host of the QAH effect is a rather "dirty" system with intentional doping defects and an average carrier mobility below 1000 $cm^2/V{\cdot}s$[35, 70]. For the quantum Hall system, the 2D electron gas's mobility can easily go above 10000 $cm^2/V{\cdot}s$[73, 74].

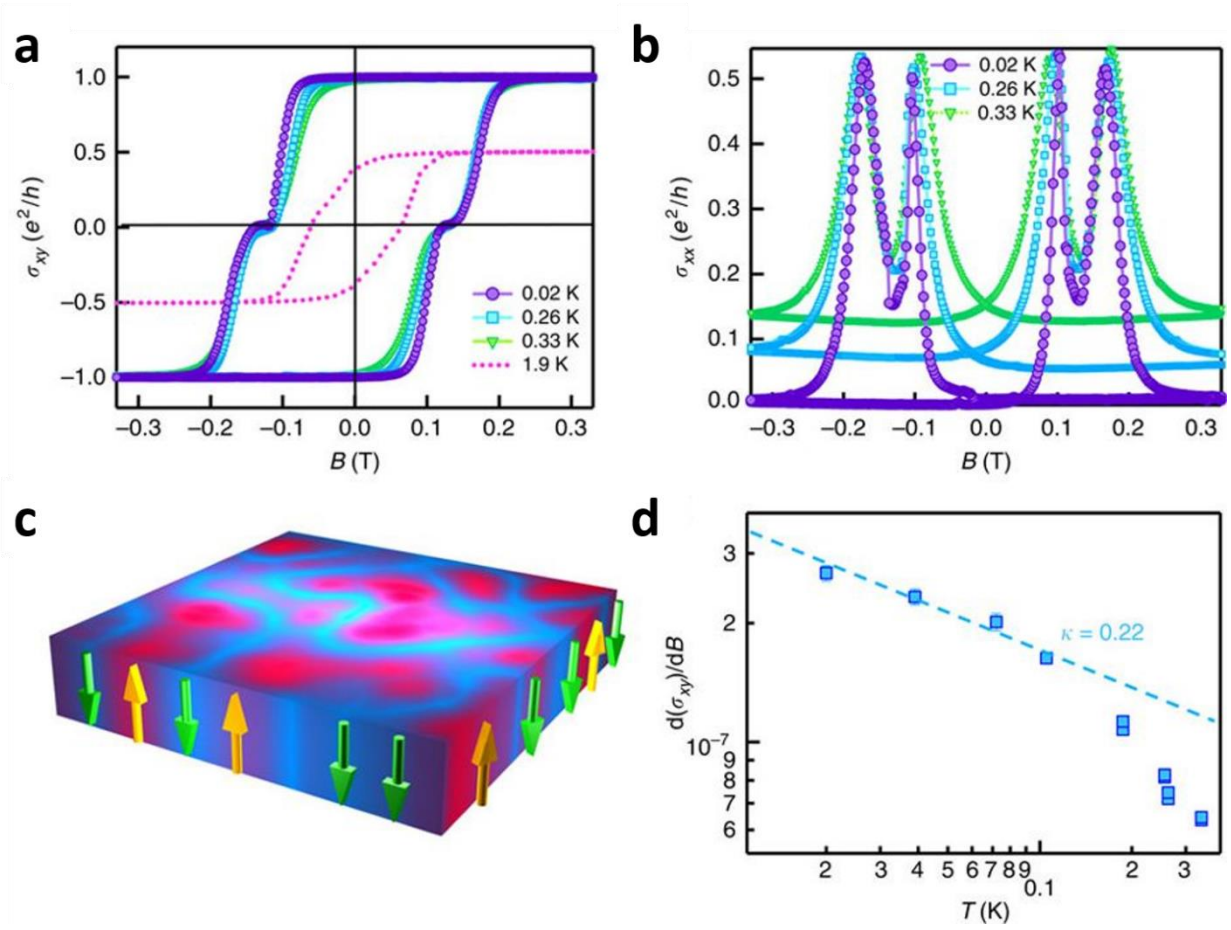

Figure 3-7 Quantum phase transition of quantum anomalous Hall effect. (a) Magnetic field-dependent σ_{xy} at different temperatures. Zero Hall plateaus at $\pm H_C$ are developed between the two QAHE states up to 0.33 K. (b) Magnetic field-dependent σ_{xx} at different temperatures. Even when the film already deviates from the perfect QAHE state at T = 0.33 K, both the zero σ_{xy} plateaus and double-peaked σ_{xx} still persist. (c) Schematic representation of the multi-domain network formed during the magnetization reversal process. The upward yellow arrows and downward green arrows denote the up and down magnetic domains, respectively. (d) Temperature-dependent transition slope $S = (\partial\sigma_{xy}/\partial H)_{max}$ extracted from (a). Adopted from Ref. [70].

3.3. Probing the low temperature limit of quantum anomalous Hall effect in Cr-doped $(BiSb)_2Te_3$

The quantum Hall effect, which was first observed in two-dimensional electron gas systems, demonstrates the first example of a quantum state that is topologically distinct from other condensed matters . Under a strong external magnetic field, the quantum Hall edge states emerging at the sample boundary exhibit the chiral dissipationless transport nature with a vanishing longitudinal resistance and a quantized Hall conductance of $\upsilon e^2/h$ (where υ is the Landau level index). Such a transport signature, if the requirement of high magnetic field can be removed, would unveil tremendous opportunities in low-power electronic applications[75]. This inspires an upsurge in searching for a zero-field version of quantum Hall effect for over three decades. One such version is known as the QAHE[7, 10, 11, 24, 31]. A topologically non-trivial electronic structure with time-reversal-symmetry broken by magnetic moment instead of an external magnetic field, is one of the most promising system to host the QAHE. Recently, the QAHE was demonstrated experimentally in magnetically doped topological insulators (MTIs), e.g., Cr/V:$(Bi,Sb)_2Te_3$, where the utilization of both the intrinsic strong spin-orbit coupling and the incorporated long-range out-of-plane ferromagnetic (FM) order give rise to the chiral edge state with a non-zero Chern number [22, 35]. However, to date, the observation of the QAHE state is yet limited to extremely low temperatures (below 1 K), even though some host MTIs possess a Curie temperature above 170 K [76, 77]. As a result, the underlying physics of this temperature limit has remained to be an open question so far [46, 60-62, 76, 78, 79].

To address this issue, earlier attempts have been focusing on understanding the FM origins and exploring the possible band structure modifications caused by the magnetic dopants. From the

ferromagnetic ordering aspect, the presence of superparamagnetic domains and their dynamics are believed to hinder the formation of a strong FM order in the MTIs [61, 80, 81]; while from the band structure point of view, the presence of both the magnetic impurity bands and the bulk valence band near the Fermi level could also introduce additional dissipative conduction channels, and hence deteriorate the transport signature of the QAHE [82, 83]. These findings all suggest sophisticated coupling mechanisms among the SOC, FM ordering, dopant profile, and film structure in realizing the QAHE [84]. Consequently, a QAHE platform in which all these key parameters can be manipulated individually is of great demand prior to pushing the limit of the QAHE towards room temperature. In this work, a set of MTI thin films are prepared with a wide tuning range of thickness and doping profile, with which the limiting factors to the onset of the QAHE can be systematically investigated. An intricate interplay between the FM order and the band structure is demonstrated by investigating the quantum transport signature, activation behavior, magneto-optic response, and the QAHE phase transition diagram. The activation behavior of the QAHE is found to be closely related to the gap between the Fermi level and its nearest bulk/impurity band edge. The tracing of such gap in samples with various thicknesses and the external magnetic field points to different origins of temperature limiting factors. More importantly, this QAHE activation gap can serve as a benchmark of the QAHE and provide a guide for searching high temperature QAHE material and heterostructures towards robust and functional QAHE states.

3.3.1. Global phase diagram of QAHE in various thicknesses

Using an optimized MTI thin film growth procedure established from our previous work [46, 70], a set of high-quality $(Cr_{0.12}Bi_{0.26}Sb_{0.62})_2Te_3$ samples with film thickness ranging from 6

QLs to 10 QLs were epitaxially grown with the Fermi level positioned inside the surface magnetic exchange gap without additional gate tuning. We first tested all the samples at 1.9 K in the PPMS system to make sure a large percent of anomalous Hall resistance quantization which is a very effective screening method to gauge the sample quality and the Fermi level position. Both longitudinal and Hall resistance data are shown in Figure 3-8.

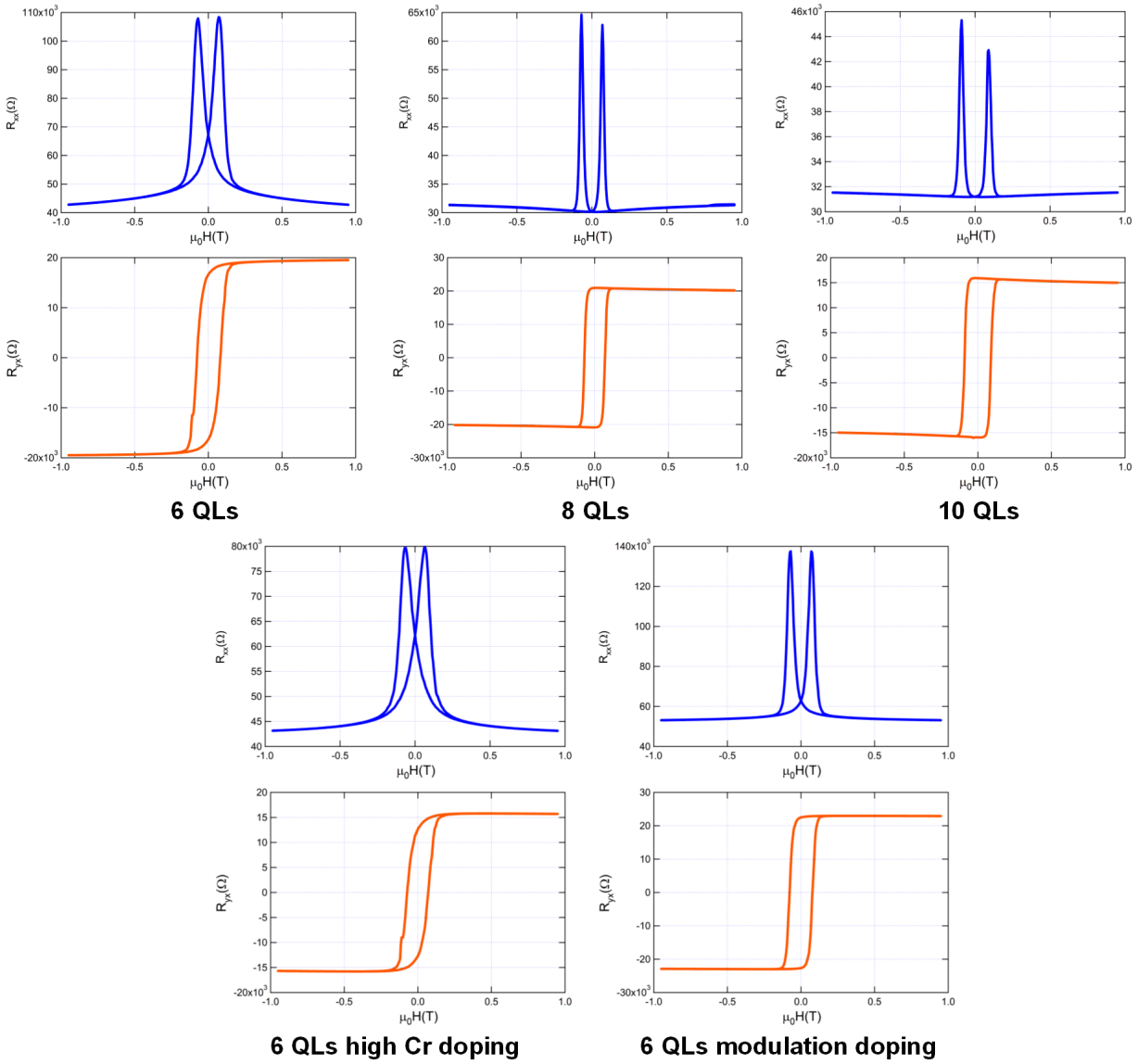

Figure 3-8 Hall measurement at 1.9 K. Hysteresis loop of R_{xx} and R_{yx} of 6 QLs MTI (uniform doping/high uniform doping/modulation doping), 8 QLs MTI and 10 QLs MTI measured at 1.9 K in PPMS system.

After verifying the thin film quality, qualified samples were loaded into dilution fridge system to conduct low temperature transport measurement at sub-1 K regimes. Figure 3-10 summarized the magneto-transport results of three uniformly-doped $(Cr_{0.12}Bi_{0.26}Sb_{0.62})_2Te_3$ samples with film thicknesses of 6 QLs, 8 QLs and 10 QLs, respectively. When the base

temperature is set at 20 mK, all three samples exhibit a fully-quantized hall resistance ($\rho_{yx} = \pm h/e^2$) at zero magnetic field, highlighting the realization of QAHE.

Strikingly, the detailed quantum conductance and topological phase transition obtained exhibit distinct features among the three samples. Specifically, at the extreme two-dimensional limit, i.e., the 6 QLs MTI sample, the top and bottom surfaces will strongly hybridize, resulting in the topological quantum phase transition between the $\pm h/e^2$ states (i.e., with Chern number C=±1 respectively) [65]. As discussed in our previous work [65, 70], the surface hybridization gap due to the quantum confinement of the 6 QLs MTI sample would compete with the magnetic exchange gap, whose magnitude is determined by the FM order. Accordingly, when the FM moment strength is minimized during the magnetization reversal, the dominant hybridization gap would give rise to a topologically trivial insulating state with C = 0. Experimentally, this emergent topological quantum transition is shown in Figure 3-10(d) and 1(g), where σ_{xx} of the 6 QLs sample goes through two peaks separating the C = ±1 and 0 states (all of which have zero σ_{xx} value), and σ_{xy} develops zero-conductance Hall-plateaus at C = 0 between the $\pm h/e^2$ states during each sweep (the orange/blue colored traces represent the different field sweep directions). Here, it is noted that the C = 0 insulating states exhibit resistance values over 10 MΩ as shown in Figure 3-9 which is by far the most insulating state reported in the QAHE systems [24, 25].

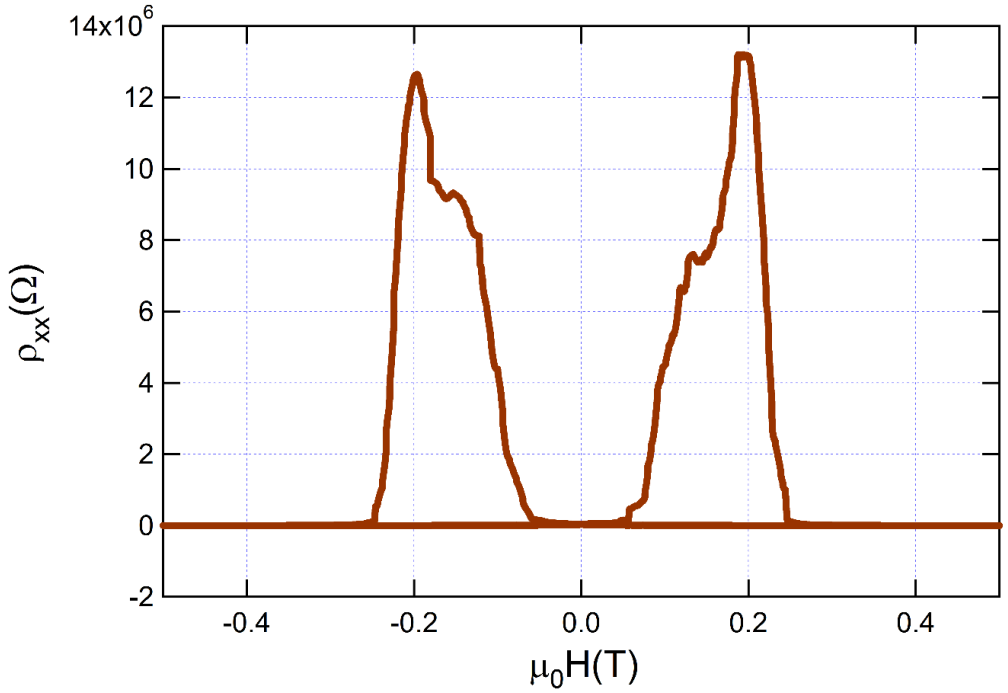

Figure 3-9 Longitudinal resistance versus external field in 6 QLs MTI. During transition, the peak resistance reaches above 10 MΩ.

Furthermore, the insulating state (σ_{xy}, σ_{xx}) = (0, 0) is found to be present across a wide magnetic field range (i.e., ~0.2 T) which not only manifests the unique metal-to-insulator switching of the QAHE state in the two-dimensional limit [70], but also offers the opportunity for searching exotic critical quantum phases, for instance, the chiral Majorana edge modes in the QAH/superconductor hybrid system between $C = \pm 1$ and $C = 0$ states [85, 86]. On the contrary, in thicker MTIs where the hybridization gap becomes negligible, the system is always topologically non-trivial with Chern number $C = \pm 1$. Such a scenario is demonstrated in both the 8 QLs and the 10 QLs samples, where a sharp transition between the $+h/e^2$ and the $-h/e^2$ edge states takes over in the QAHE hysteresis loop without the presence of any intermediate insulating states, as shown in Figure 3-10(e-f) and (h-i).

By achieving the QAH states across a wide thickness range, we can complete a thickness-dependent QAH phase diagram. As highlighted in Figure 3-10(k), the (σ_{xy}, σ_{xx}) plot of the 6 QLs MTI sample follows a double semicircular transition which continuously connects the ($\pm e^2/h$, 0) and (0, 0) states, while the 8 QLs and 10 QLs samples only exhibit two stable states at ($\pm e^2/h$, 0). More importantly, under the fixed magnetic sweeping speed (0.1 T/min), the 8 QLs film shows a single-domain behavior where the transition between the two quantized υ=±1 states is fast with only a few discrete (σ_{xy}, σ_{xx}) points located along the meta-stable transition route; on the contrary, the (σ_{xy}, σ_{xx}) plot of 10 QLs sample displays a more continuous feature and the transition loop is found to be slightly deviated from the perfect semicircle contour, which may suggest the presence of additional dissipative conduction path (given that the 10 QLs film may possibly have the largest bulk contribution). Interestingly, we notice that when the quantum confinement dominates in the ultra-thin MTI film (i.e., 5 QLs), the hybridization gap will simply drive the host QAHE system into a topologically trivial insulating state regardless of the external magnetic field [28-30]. Under such circumstances, the 5 QLs phase diagram reduces to a single point where σ_{xy} and σ_{xx} both are equal to zero corresponding to the fact that the Fermi level rests inside the trivial surface and bulk gap. In short, the thickness-dependent QAHE results, along with the corresponding QAH phase diagram shown in Figure 3-10(k), signify the importance of film thickness (or equivalently, the magnetic exchange gap and hybridization gap), thus implying the possibility to enhance the QAH temperature and manipulate QAH states via structural engineering, for which we will discuss in Section 3.3.4.

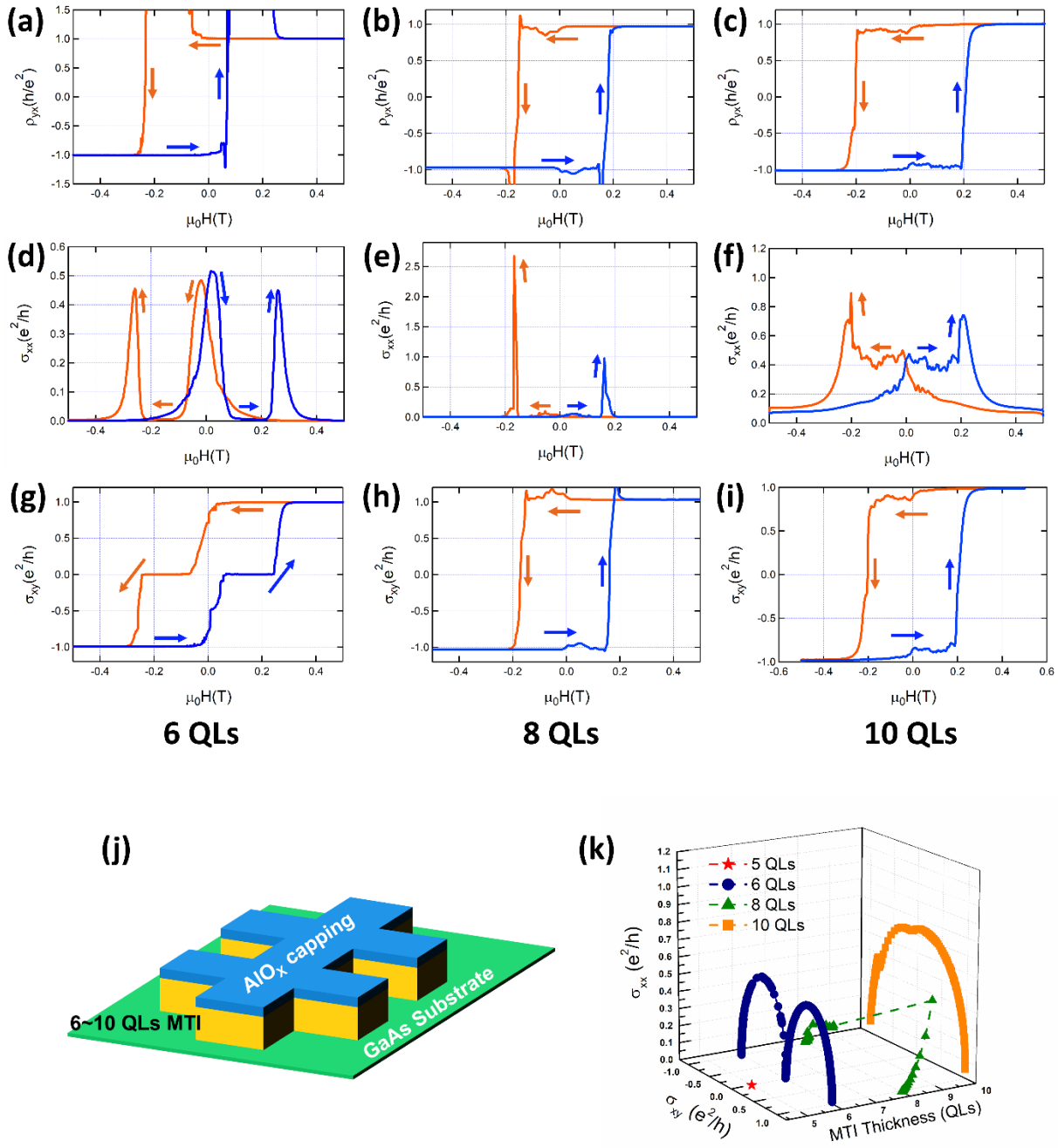

Figure 3-10 QAHE realized in different thicknesses of MTIs. Curves in red indicate the magnetic field sweeping from the positive to the negative direction and blue curves indicate the reverse trace. (a-c) Hall resistivity versus external magnetic field for samples with thicknesses of 6 QLs, 8 QLs and 10 QLs, respectively. All samples show Hall resistivity quantized at $\pm h/e^2$ at zero magnetic field. (d-f) Longitudinal conductivity for the same set of MTIs. At zero magnetic

field, 8 QLs and 10 QLs of MTI show vanishing longitudinal conductivity, yet the 6 QLs MTI shows a split double-peak behavior around the coercive field and non-zero longitudinal conductivity. (g-i) Hall conductivity for the same set of MTIs. At zero magnetic field, 8 QLs and 10 QLs MTI show quantized σ_{xy} at e^2/h. The 6 QLs MTI (g) shows zero-Hall-plateaus at coercive field and deviation from perfect quantized $\pm e^2/h$ when the external field is approaching zero. (j) Schematic drawing of the MTI samples. (k) Global phase diagram of the QAHE for MTIs' thicknesses range from 5 QLs to 10 QLs. For 5 QLs MTI, the hybridization gap dominates the system and drives it into a trivial insulator. For 6 QLs MTI, the competition between hybridization gap and exchange gap during transition forms a unique double-semicircle transition curve. For 8 QLs and 10 QLs sample, the phase transition only happens between the $C = \pm 1$ states.

3.3.2. QAH activation gap

In both integer and fractional QHE, the activation energy scale, which is usually extracted from the temperature-dependent σ_{xx} plot, has been widely used to determine the robustness of such quantum state against thermal fluctuation [69, 87, 88]. Sharing the same topological nature [89], the QAH activation gap (Δ) also carries similar information as its quantum Hall effect counterpart, hence it can be investigated by using the same approach. Application-wise, this activation gap size, which serves as a benchmark parameter, dictates the viable temperature range to utilize the dissipationless nature of QAH states. Inspired by the unique thickness-dependent QAH transport behaviors obtained in Figure 3-10, we further traced the QAH activation gap in these MTI thin films with different magnetic-field responses to better understand the underlying mechanisms, as well as to probe the possible temperature limiting factors. In particular, we attempted to use a single-activation-gap Arrhenius equation $\sigma_{xx} = \sigma_0 \cdot exp\left(-\frac{\Delta}{k_B T}\right)$ to fit the data, yet only succeeded in the high field regime in the 6 QLs MTI sample, as shown in Figure 3-11(a). Alternatively, when the external field was smaller than 0.15 T, an additional dissipative

conductivity term σ_1 that does not follow the Arrhenius equation had to be included to fit the data such that,

$$\sigma_{xx} = \sum_{i=0,1} \sigma_i \cdot exp\left(-\frac{\Delta_i}{k_B T}\right), \Delta_1 = 0 \qquad (3-2)$$

In contrast, the quantum Hall effect activation behaviors can always be described by one or few activation energies which follow Arrhenius equation in either graphene, oxide material or two-dimensional electron gas systems [88, 90-92]. Meanwhile, both Δ_0 and σ_1 have a strong field dependence where the increase of the applied magnetic field results in a larger activation gap and a smaller dissipative component, as depicted in Figure 3-11(d) and (e). Therefore, we may conclude that to drive the system into a near-perfect QAH state with minimized σ_1, an additional external field (> 0.15 T) is required to suppress the dissipative channel caused by the weak ferromagnetism and existence of superparamagnetism in the 6 QLs sample, as we will elaborate in Section III.

On the other hand, when the thin film thickness is beyond 6 QLs, the activation feature dramatically changes. As compared with the 6 QLs sample, the activated conduction behaviors of both the 8 QLs and 10 QLs samples always include both the dissipative conductivity σ_1 across the entire magnetic field range (0 T to 5 T), as shown in Figure 3-11(d). More interestingly, unlike the 6 QLs case, the magnitude of σ_1 in thicker MTI samples are found to gradually increase under larger magnetic field, hence implying a different origin of the dissipative channel rather than the unstable ferromagnetism, as illustrated in Figure 3-11(d). In fact, such phenomenon is commonly observed in metallic systems where the positive magneto-resistance background is related to the Fermi level crossing the trivial band edges. Besides, it is noted that our results agree well with the recent ARPES study [82] focusing on the band structure near the Dirac-point of the MTI, which showed the overlapping of the nontrivial surface band with the trivial bulk valence band.

In the meanwhile, as summarized in Figure 3-11(e), the QAH activation gaps Δ_0 in the cases of 8 QLs and 10 QLs MTIs are both negatively related to the external magnetic field, which are opposite to the 6 QLs scenario. Such field-dependent feature highlights the pronounced splitting of the bulk valence band under high magnetic field in the thicker MTI samples [93]. In general, magnetic dopants can induce an energy splitting between up and down spins, which has been well studied in diluted magnetic semiconductors[93, 94]. This splitting comes from the combined effect of the on-sight exchange energy and the Zeeman energy given by the applied field. The MTI system, without considering its topological property, also falls in the category as a diluted magnetic semiconductor system[95]. Such band splitting can impact MTI's transport properties if they are included in the thermal window. As shown in Figure 3-11(f), in the case of 6 QLs, the bulk-band splitting does not strongly impact the transport since they are pushed away from the surface bands due to the vertical quantum confinement. However, beyond 6 QLs, the band edges are closer to the Fermi level, and the activation gap Δ_0 may be strongly modulated. An increase in the applied field can enlarge the spin splitting, and therefore Δ_0 decreases. Furthermore, we need to point out that the 8 QLs sample shows almost five times larger activation gap and one order of magnitude smaller dissipative term than the 10 QLs sample. This dramatic difference again manifests the critical thickness limiting factor in the $(Bi,Sb)_2Te_3$ based QAH system where the inevitable increased bulk contribution finally prevents QAHE in even thicker MTI samples.

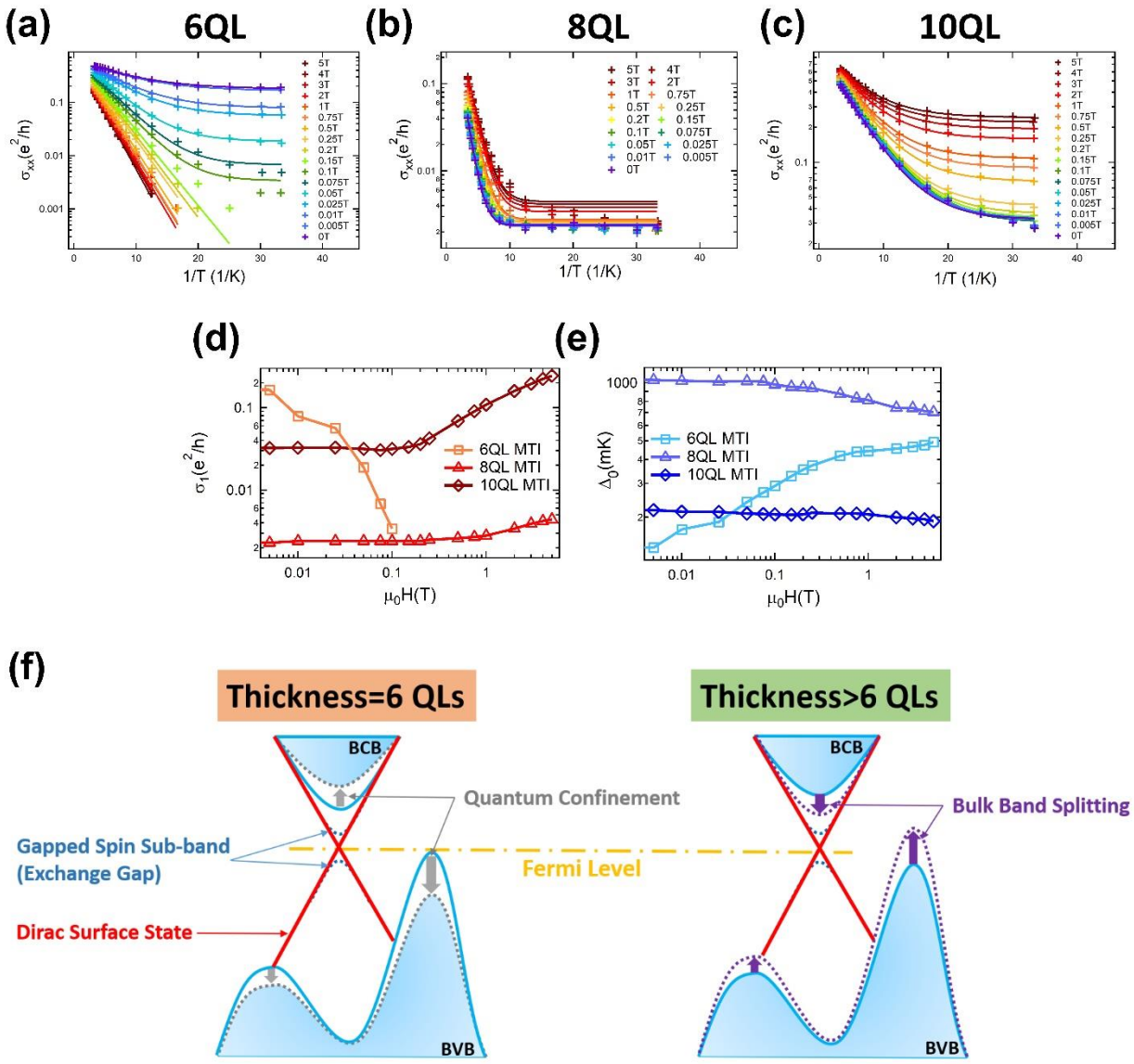

Figure 3-11 Field dependent longitudinal conductivity and activation behavior in different thicknesses of MTI. (a-c) σ_{xx} as a function of inverse temperature for 6 QLs, 8 QLs and 10 QLs MTIs with modified Arrhenius fit (details in text) under different external magnetic field. (d-e) Magnetic field dependence of parallel dissipative conductivity (σ_1) and QAH activation energy (Δ_0) of the 6 QLs, 8 QLs and 10 QLs MTIs extracted from (a-c) using modified Arrhenius fit. (f) Schematic drawing of band structure around Dirac point for thickness equal (Left) and larger to 6 QLs (Right). The shifted bulk band edge and its relative position with Fermi level explains the different magnetic field effect on activation energy for MTIs with different thicknesses.

3.3.3. Magneto-optic Kerr effect

The above transport experiments of the 6 QLs MTI sample revealed the importance of MTI's ferromagnetism in reaching full quantization. Unlike the 8 QLs and 10 QLs MTI samples, it is noted that the conductance σ_{xx} and σ_{xy} of the 6 QLs MTI deviate from the quantized value before the external field approaches zero, as shown in Figure 3-10(d) and (g). Therefore, the need of an additional small external field to realize full quantization may imply the existence of soft magnetic order in the 6 QLs MTI sample. To directly address this point, we further performed MOKE measurements on one of our 6 QLs MTI samples. The magneto-optical setup is constructed with a loop-less fiber-optic Sagnac interferometer for better sensitivity, which can accurately measure time-reversal-symmetry breaking event down to 10 nano-radians [96]. Figure 3-13(a) and (b) summarize both the temperature-dependent Kerr rotation angle and the anomalous Hall resistance R_{yx} results which are taken simultaneously. It is observed that the magnetic hysteresis behavior revealed by both results are highly consistent across a wide temperature range (70 mK-28 K) in terms of the coercive field size. Yet we need to emphasize the major difference between the two sets of data: when the system temperature decreases, the up-ramping of magnetic field quickly drives the Kerr signal to a saturation value around 10^{-3} rad that almost remains the same for up to 4.3 K as shown in Figure 3-13(a)(i.e., indicating the magnetization of the MTI sample is fully saturated); in contrast, the R_{yx} value will not reach the quantized h/e^2 value until T < 700 mK as shown in Figure 3-13(b). This finding may suggest that the robust macroscopic ferromagnetic order alone does not necessarily guarantee the dissipationless quantum transport in our MTI system.

As mentioned in Section II, we have identified the presence of a dissipative conductivity σ1 when the applied magnetic field is smaller than 0.15 T and related this term to the weak

ferromagnetism in the 6 QLs MTI. More importantly, in Figure 3-13(a) and (b), it is also noticed that the coercivity nearly vanishes above 12 K even though there is still a noticeable magnetic moment. Along with the quantization deviation shown in Figure 3-10(d) and (g), the above observations provide evidence of superparamagnetism's existence in the sample, which is often observed in a low dimensional magnetic system[97, 98]. To further justify our argument, we conducted a series of measurements tracing both temperature-dependent Kerr signal and R_{yx} signals by using different field cooling/warming schemes as shown in Figure 3-13(c-f). In the linear-scale plot, Figure 3-13(c) and (d), the temperature-dependent Kerr rotation signal during the field cooling ($\mu_0 H$ = 400 mT and 12 mT) process does not follow classic Curie-Weiss type of spontaneous magnetization behavior as a typical ferromagnet as shown in Figure 3-12[99].

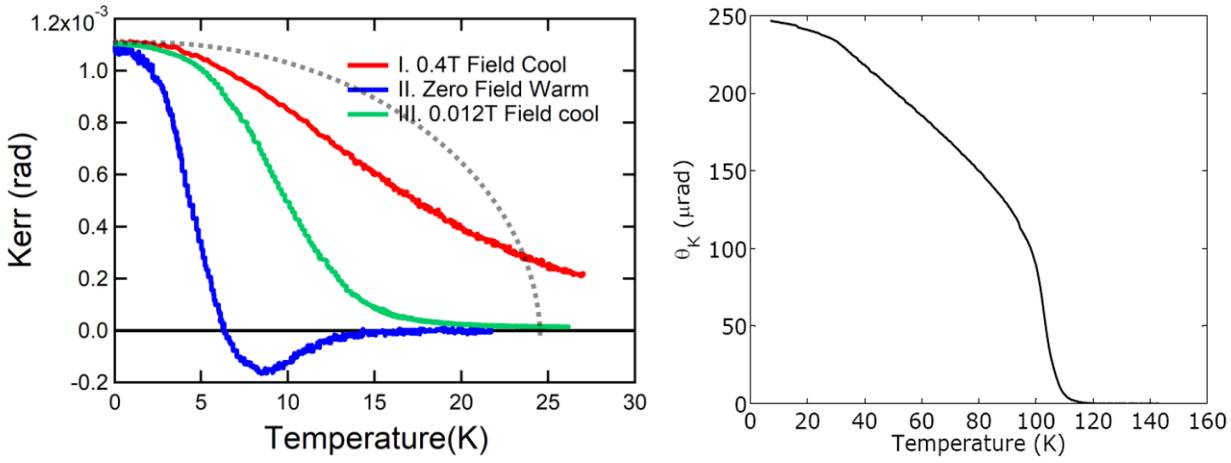

Figure 3-12 Comparison between MTI's ferromagnetism with typical ferromagnet. Reproduced Figure 3-13(a)(left) added with a qualitative curve (black dashed line) showing a typical ferromagnet's zero-field-warming curve and the Kerr rotation of $SrRuO_3$ during zero-field warming(right).

The evident discrepancy between the two field-cooling curves (red and green in Figure 3-13(c) and (d)) acquired under different magnetic fields suggests that the magnetism of 6 QLs

MTI is not strong enough to yield a robust order without the assistance of external field. More remarkably, during the succeeding zero-field warming process (step II curve in Figure 3-13(c) and (d), respectively), such anomaly in ferromagnetism in the 6 QLs MTI becomes more pronounced according to the following two observations. First, the deviation from the saturation magnetization starts as early as 400 mK (blue trace in Figure 3-13(e) and (f), T=400 mK is highlighted with dashed line) which is almost two orders of magnitude lower than MTI's perceived Curie temperature (~20 K). In addition, the zero-field warming curves for Kerr and R_{yx} signal go to near-zero when the base temperature reaches above 14 K. It may be attributed to the spin relaxation due to the competition between the magnetic anisotropy energy KV (K is the magnetocrystalline anisotropy constant, V is the nanomagnet volume) versus the thermal fluctuation energy k_BT, as the origin of superparamagnetism [100]. Secondly, we observed a rather abnormal sign change of both the Kerr rotation signal and the Hall voltage during the zero-field warming process within the [4 K, 10 K] regime. The reason of such magnetization flipping at elevated temperature is not clear yet, but it has also been observed in some magnetic systems with complicated spin configurations [101, 102]. The effect arising from the antiferromagnetically coupled Cr/Sb and Te moment identified using X-ray magnetic circular dichroism technique [103, 104] might participate in this phenomenon, which requires further investigation.

To conclude this part, for the 6 QLs uniform-doped MTI, this magnetic anisotropy energy when converted to temperature (T_{KV}), should be much lower than the Curie temperature T_C given that the onset of QAHE happens only at T < 700 mK. As a result, superparamagnetic domains may form inside the film [81] over a relatively wide temperature range, and the misalignment of such domains may account for the small QAHE activation gap Δ_0 as well as the parallel dissipative

conductivity σ_1 in the hybridized 2D MTI system. Therefore, to solve this problem, major effort should focus on improving MTIs with not only more robust but more uniform ferromagnetic order.

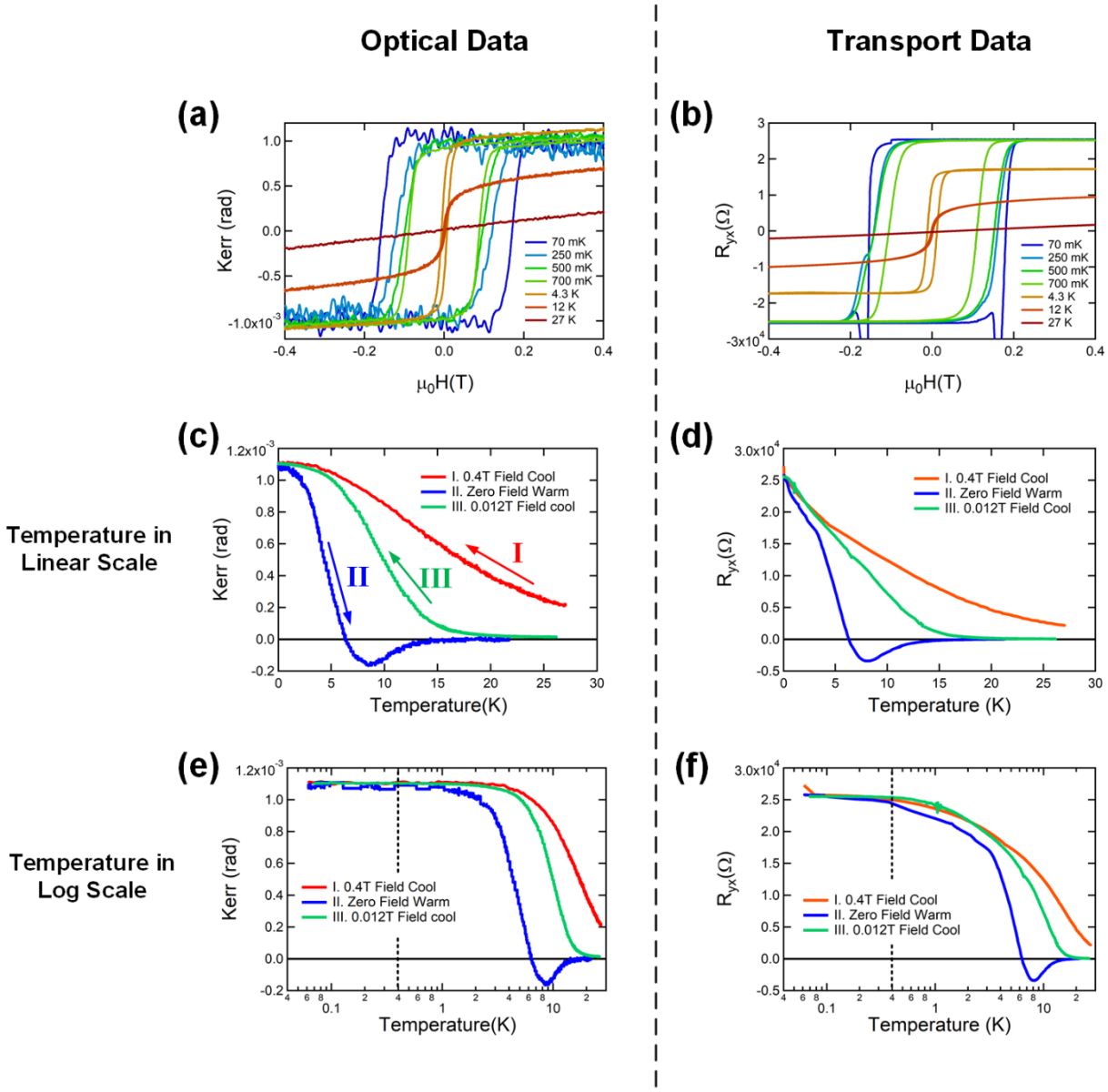

Figure 3-13 Concurrent magneto-optic Kerr effect and transport measurements of 6 QLs MTI. The magneto-optic setup is enhanced by Sagnac interferometer. (a, b) Hysteresis loops of Kerr rotation angle and Hall resistance at different temperatures. The ferromagnetic behavior of 6 QLs MTI disappears at 27 K. (c, d) Kerr rotation angle and Hall resistance under different field cooling and warming schemes. Under zero field warming, both Kerr rotation angle and Hall

resistance undergo a sign flipping during the process indicate an unstable ferromagnetism inside this 6 QLs MTI. (e, f) Re-plot of (c) and (d) by using log-scale for temperature. The expansion of low temperature data reveals the saturation of the Kerr rotation angle and the Hall resistance occurs at a much lower temperature regime (<400 mK) than the Curie temperature which indicate another temperature scale that is related to 6 QLs MTI's ferromagnetism and superparamagnetism observed.

3.3.4. Towards high temperature and functional QAHE

So far, we have identified two methods which may help to increase the QAH gap, namely the uniform single-domain ferromagnetic texture and the minimized dissipative bulk conduction channel. For the case of thicker MTI films, the realization of the QAHE is limited by the intrinsic band structure (*i.e.*, the small thermal window between the Fermi level and the bulk valence band as shown in Figure 3-11(f)). Therefore, in order to enlarge the thermal window, additional elemental doping (*e.g.,* Sn or S [105, 106]) are required to modify the bulk valence band. However, the involvement of such high vapor pressure elements would inevitably make it more difficult to precisely control the chemical composition of the MTI sample during sample growth [70]. Alternatively, as we demonstrated in Section II, the 2D MTI system turns out to be a better platform for the pursuit of high-temperature QAHE, since the parallel bulk conduction is minimized and the dissipative conductivity σ_1 (due to the multi-domain and superparamagnetic texture) can be suppressed with the assistance of the external magnetic field. Accordingly, to further stabilize the magnetic domain and to increase the QAHE exchange gap Δ_0 at zero magnetic field, we introduce structural engineering on the 2D MTI system by modifying the dopant profile in the 6 QLs MTI candidates.

To experimentally validate the above proposal, we prepared two additional 2D MTI samples with different structures: one is a uniformly-doped 6 QLs $(Cr_{0.16}Bi_{0.25}Sb_{0.59})_2Te_3$ with higher Cr doping of 16%; the other one is a trilayer structure sample where both the top and bottom surfaces (*i.e.*, with the thickness of 1 QL) are heavily-doped by Cr (~24%) while the bulk 4 QLs remains as the $(Cr_{0.12}Bi_{0.26}Sb_{0.62})_2Te_3$ composition, as illustrated in Figure 3-15(a). It is found that the higher uniform Cr-doping MTI showed similar transport behavior as the one with original recipe as shown in Figure 3-15(d). In contrast, for the trilayer modulation-doped MTI, the activated conduction plot shown in Figure 3-15(b) is governed by the single-gap picture without the presence of the dissipative σ_1 contribution even at zero magnetic field. More significantly, the measured QAH activation gap Δ_0= 80 μeV is more than 4 times larger than the uniform MTI counterpart at zero field, and is almost insensitive to external magnetic field, as highlighted in Figure 3-15(c). Concurrently, the longitudinal and hall conductance in this trilayer 6 QLs MTI sample perfectly quantized at $(\sigma_{xx}, \sigma_{xy}) = (0, \pm h/e^2)$ at zero field as shown in Figure 3-14, hence manifesting the formation of a robust intrinsic ferromagnetic order.

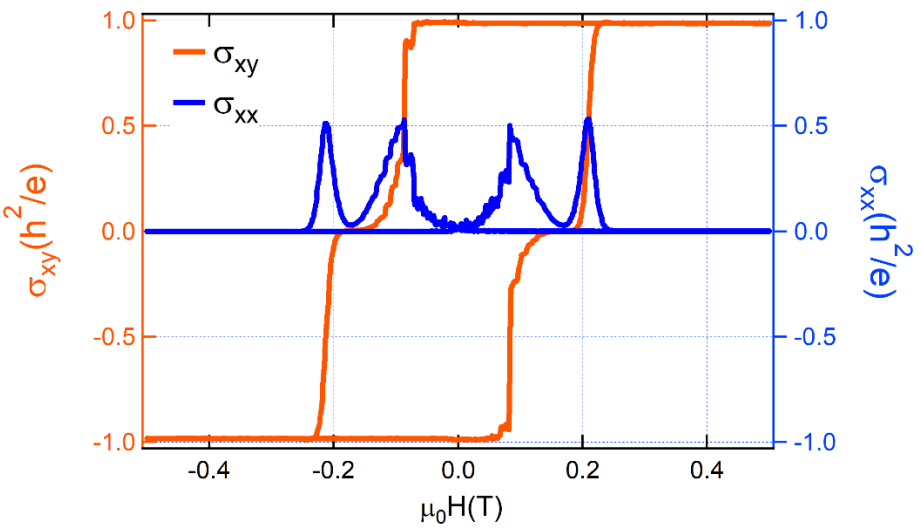

Figure 3-14 Hysteresis loop of Hall and longitudinal conductance of trilayer doped 6 QLs MTI measured at 20 mK.

Here, we need to point out that the onset of the QAHE in the trilayer sample is still around T = 1 K due to the relatively small magnetic exchange gap, (Indeed, several studies suggested the inhomogeneity of magnetic dopants could effectively smear out the exchange gap [107, 108]). Nevertheless, the use of the trilayer configuration by structural engineering unveils an effective way to drive the occurrence of the QAH state towards higher temperature.

In addition, it is also noted that while a more robust remnant quantized state in the modulation-doped 6 QLs MTI films was achieved, the flat zero-Hall plateaus have narrowed down to 0.04T, as shown in Figure 3-15(d). As discussed above, the exchange gap by modulation doping effectively modulates the relative strength between Δ_M (exchange gap size) and m_0 (hybridization gap size) especially during the magnetization reversal process where the filling factor C is related to parameters as [65]:

$$C = \begin{cases} \frac{\Delta_m}{|\Delta_m|}, & \text{for } |\Delta_m| > |m_0| \\ 0, & \text{for } |\Delta_m| < |m_0| \end{cases} \qquad (3-3)$$

The size of the zero-Hall plateaus is a key factor to successfully observing the chiral Majorana edge mode. By using different doping profile, we are able to control the width effectively. Consequently, such doping strategy can serve as an additional degree of freedom to control the chiral Majorana edge mode based on the MTI/superconductor heterostructure [86].

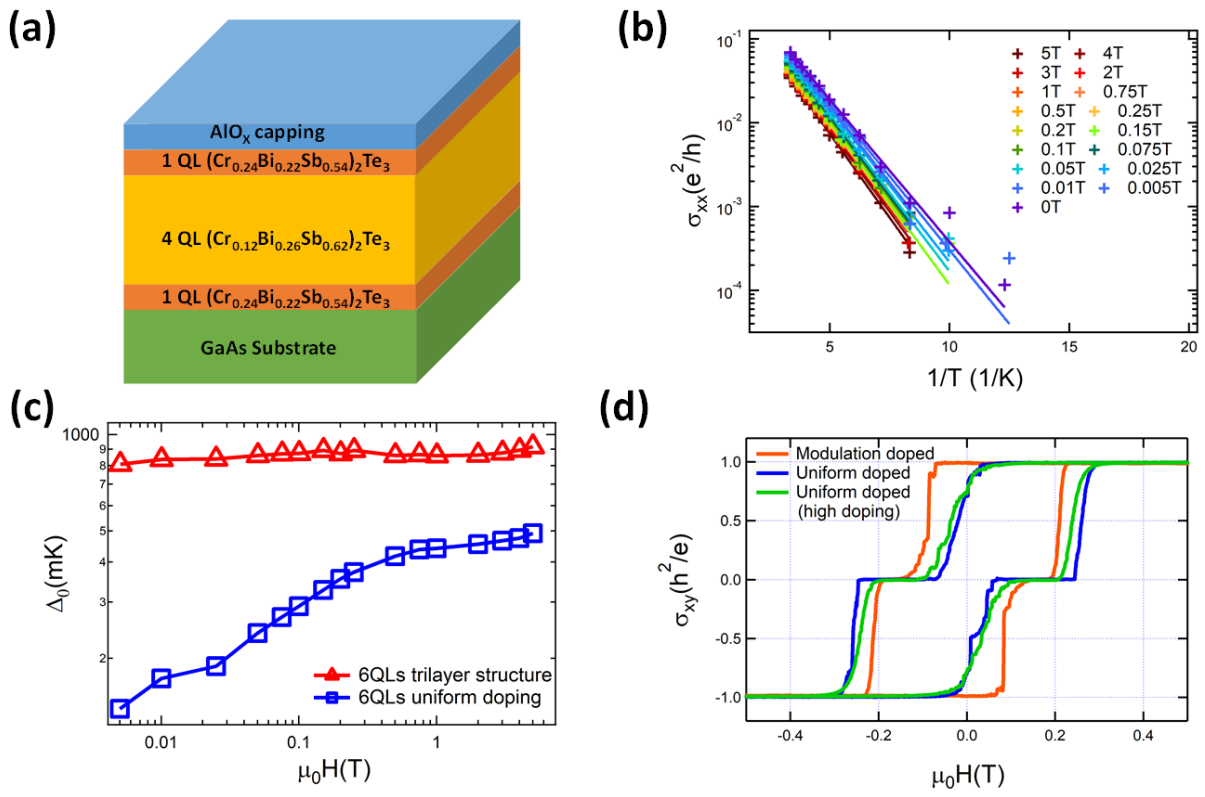

Figure 3-15 Structural engineering and tunable zero-hall plateaus in 6 QLs MTI samples. (a) Schematic drawing of the trilayer 6 QLs MTI structure with heavy Cr-doping at top and bottom surfaces. (b) σ_{xx} as a function of inverse temperature for the trilayer 6 QLs MTI sample at different external magnetic fields. The Arrhenius fitting does not need the use of extra dissipative term. (c) Comparison of the QAH activation energy versus external field between trilayer MTI and uniformly doped MTI. The trilayer QAH activation energy shows much less field dependency,

manifesting a more robust ferromagnetism. (d) Hysteresis loop of σ_{xx} for the 6 QLs MTIs samples using three different doping profiles. The widths of zero-Hall-plateaus in these samples vary greatly due to the doping engineering.

3.4. Summary of Chapter 3

In this chapter, we investigate the scale-invariant property of the QAH effect in thick magnetic TI samples and in milli-meter sized devices. The dissipationless chiral edge states and quantized Hall resistance showing at zero magnetic field demonstrate the unique advantage of this physical phenomenon towards low-dissipation electronics and spintronics.

In addition, by introducing vertical quantum confinement into the thin film system utilizing the advantage of MBE growth, we observed the intricate interplay between magnetic field and band topology. The accurate thickness control of the magnetic TI thin film facilitates the successful observation of metal-to-insulator transition in the QAH systems. And we find out that though the QAH effect shares the same topological nature with the quantum Hall effect, the detailed physical origins are very different. Specifically, in the zero-Hall plateau phenomenon observed both in the graphene quantum Hall system and the magnetic TI QAH system, the transport signature indeed looks similar, the microscopic details are different.

We have also studied the temperature limiting factors of the QAH states by quantitatively investigating the quantum transport behavior across a wide range of thickness and doping of MTI as well as their magneto-optic response. We showed that in the hybridized 2D limit (6 QLs), the QAH temperature is mostly limited by the formation of superparamagnetic states. By introducing proper modulation doping of Cr element, we successfully enlarged the exchange gap and stabilize

the ferromagnetism near zero field. However, the QAH gap size is still limited to around 1K. We believe that the small gap-size problem cannot be fully resolved by increasing the doping level alone. Because firstly magnetic doping is capped by solubility limit; and secondly the associated decrease in SOC when Cr substitutes the heavy element (*e.g.*, Bi or Sb) in MTI will restrict the upper bound of magnetic doping. Beyond the doping level limit, the statistical random fluctuation of magnetic dopant is also inevitable in MBE as well as any other low temperature epitaxy technique. This effect greatly limits the global non-trivial exchange gap size which explains the experimental discrepancy between the local 30 meV mass gap measured by scanning tunneling microscopy [109, 110] and a much smaller average activation gap size measured using transport method. On the other hand, for thicker MTI samples (8 QLs and 10 QLs) with more robust ferromagnetism, the QAH state is governed by the bulk effect and the activation gap size is vulnerable to the vicinity of the Fermi level to the bulk valence band. As a result, the onset temperature of the QAHE did not exhibit clear advantage over the 2D MTI samples.

Based on the results presented in this work, to further increase the QAH gap as well as its occurring temperature, here we propose two approaches. Internally, we could dope extra element that fulfills any of the following criterion: 1. element that introduces large SOC; 2. element that promotes long range coupling of the existing magnetic dopants; 3. elements that can suppress the side valence band near the Dirac point. Externally, we could interface highly ordered ferromagnetic or antiferromagnetic insulator to counter the inhomogeneity issue and raise MTI's ordering temperature through effective exchange interactions[27, 111].

Beyond the QAHE observed in current material system, we demonstrated the importance of structural engineering to functionalize the QAH states, especially for the study of the chiral Majorana edge mode and axion insulators[112, 113]. By optimizing the thickness and doping

profile of MTI, we could control the width of the quantized hall plateaus that adds an additional dimension to manipulate the chiral Majorana edge states which can be potentially utilized in fault-tolerant topological quantum computations.

Chapter 4

Topological insulator antiferromagnet heterostructures

4.1. Quantum anomalous Hall insulator/Cr_2O_3 heterostructure

The recent realization of the quantum anomalous Hall effect in magnetically-doped 3D TIs opens new possibilities for realizing dissipationless edge states without the application of an external magnetic field[24, 35]. With the introduction of magnetic dopants, the time-reversal symmetry of the topological surface states is broken, and the resulting magnetic exchange gap has led to a series of exotic physical phenomena[114-116]. Meanwhile, the engineering of TI-based magnetic heterostructures has greatly broadened the research areas and capability as the interfacial discontinuities in the topological or magnetic order yield a complex energy landscape which enables deterministic manipulation of the constituent materials[28, 117]. For example, the integration of a QAH insulator with a superconductor leads to the chiral Majorana edge modes[85, 86], and the growth of multi-layer QAH insulator layers spaced by the normal insulator CdSe results in an artificial high Chern number QAH insulator[118]. Currently, while most functional heterostructures have mainly focused on the control of the topological nature of the QAH insulator, the use of magnetic couplings in such hybrid systems to manipulate the QAH state has still remained unexplored. In the quest towards realizing a magnetic or antiferromagnetic

heterostructure based on a QAH insulator, there are two major challenges: Firstly, the material must be highly insulating to avoid current shunting effects. Secondly, the critical growth requirements for achieving the QAHE mandate that the selected magnetic material must be compatible with the QAH insulator, especially when it serves as the substrate. In addition, it is highly desirable that the adjacent magnetic layer would enable the effective manipulation of the magnetic or topological order in the QAH insulator, either through direct interface exchange (*e.g.* exchange bias) coupling or via magnetoelectric effect.

To address the above points, one potential candidate is Cr_2O_3, an antiferromagnetic insulator with Néel temperature (T_N) around 300 K[53]. As introduced in Chapter 2.4.1, we are able to prepare high quality TI/Cr_2O_3/Sapphire(0001) heterostructures using MBE growth technique. Given our previous experience of the Cr:$(Bi,Sb)_2Te_3$ growth on the Al_2O_3(0001) substrate[111], the realization of the QAH insulator on Cr_2O_3 is also possible. Furthermore, Cr_2O_3 is also known as a magnetoelectric material in which a net magnetic moment can be induced by applying an electric field. Such phenomenon, if properly utilized, can electrically manipulate the magnetic states of an adjacent exchange-coupled ferromagnetic material, thereafter enabling the electric-field controlled exchange bias[57, 119].

In this study, the MTI/Cr_2O_3 heterostructure exhibits the QAHE at low-temperature where dissipationless chiral edge conduction is achieved. In addition, by using the field cooling and depth-sensitive polarized neutron reflectometry techniques, we reveal the presence of exchange bias in the system as a result of strong interfacial exchange coupling. This work provides a new platform to study the interaction between quantum anomalous Hall insulator and antiferromagnet and unveils enormous opportunities for functionalizing and manipulating the quantum anomalous states through coupling with antiferromagnetic order.

4.1.1. Observation of QAH effect in MTI/Cr_2O_3 heterostructure

Most QAH insulators are currently grown on traditional semiconductor substrate (e.g., InP and GaAs[46, 120]) to achieve the best thin film quality, or on complex oxides (e.g., $SrTiO_3$[76]) to gain control of the thin film's chemical potential through back-gating. After careful tuning of the growth recipe, we successfully achieved high quality MTI on top of the (0001) Cr_2O_3/Al_2O_3 substrate.

After the sample growth, standard milli-meter sized Hall-bar device was fabricated. The device was then loaded into the dilution fridge with indium contacts attached to the device to allow transport measurement. As illustrated in Figure 4-1(a-b), when the sample is cooled down to 20 mK, the Hall resistivity reaches the quantized state at $\rho_{yx} = 1\ h/e^2$ and the longitudinal resistivity dropped to below 0.1 h/e^2. Using conductance tensor conversion to convert resistivity to conductivity, we can obtain the quantum phase transition as shown in Figure 4-1(c) where the semi-circular relationship of the conductance plot $(\sigma_{xy}, \sigma_{xx})$ continuously connect the two quantized points at $(\sigma_{xy}, \sigma_{xx}) = (\pm e^2/h, 0)$, again manifesting the quantum transport feature of the QAHE [70].

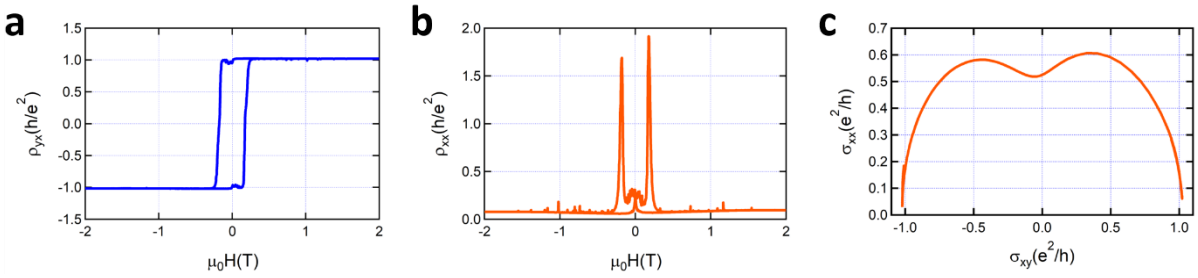

Figure 4-1 Realization of QAHE in MTI/Cr2O3 heterostructure. (a) Magnetic field dependent quantized anomalous Hall resistance. (b) Magnetic field dependent longitudinal resistance. (c) Phase transition when sweeping the external field.

(a-b) Hall and longitudinal resistivity of an MTI/Cr_2O_3 Hall-bar measured at 20 mK, Hall resistance reached 1 h/e^2. (c) Evolution of longitudinal conductivity σ_{xx} versus σ_{xy} when magnetic field was sweeping between two saturation states (+2 T and -2 T). The semicircular flow between (e^2/h, 0) points on the graph shows the quantum Hall states transition.

4.1.2. Exchange bias effect in MTI/Cr_2O_3 heterostructure

In order to understand the magnetic interaction between the two material systems, we performed exchange bias measurement. In a QAH insulator/Cr_2O_3 structure, we performed a series of magneto-transport measurements under different field cooling conditions. In particular, the sample was first warmed up to 320 K (i.e., above the T_N of Cr_2O_3 of 297 K), at which point a perpendicular magnetic field ranging from +3 T to -3 T was applied followed by cooling to 1.45 K. Once the base temperature was reached, anomalous Hall measurements were performed to capture the hysteresis loop shift due to exchange bias. As shown in Figure 4-2, the hysteresis loop of the QAH insulator under different field cool condition surprisingly exhibits no obvious exchange bias.

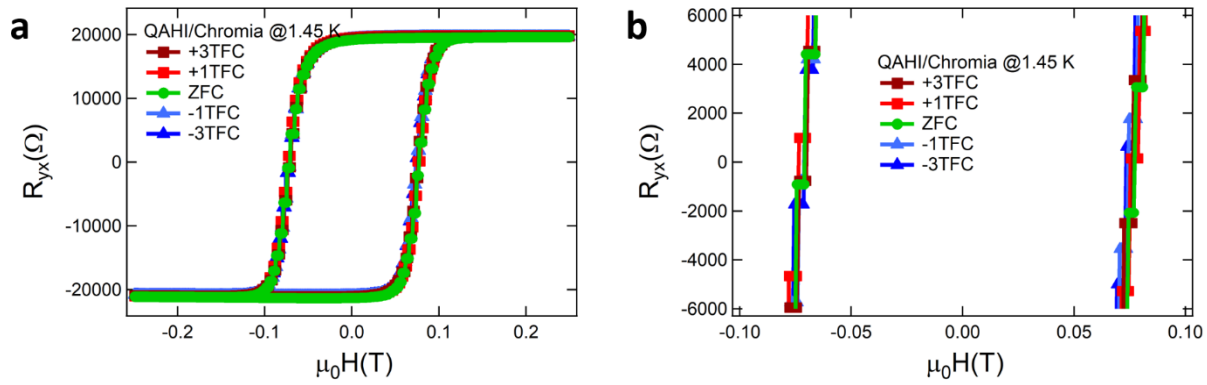

Figure 4-2 Hysteresis loops of QAH insulator/Cr_2O_3 heterostructures after different magnetic field cooling. (a) Full loop scan. (b) Expanded version of (a) to highlight near-zero exchange bias in this structure.

For comparison, we grew several MTIs on Cr_2O_3 with the same thickness but away from the optimized element ratio so that the Fermi level does not reside in the exchange gap of the Dirac cone, and as a result these films do not achieve quantization, as exemplified by a such smaller Hall resistance at 1.9 K in Figure 4-3(a). The exchange bias field for both the QAHI/Cr_2O_3 and the non-quantized MTI/Cr_2O_3 are extracted by subtracting the zero-field cooled hysteresis loop center position from the field cooled ones and presented in Figure 4-3(c).

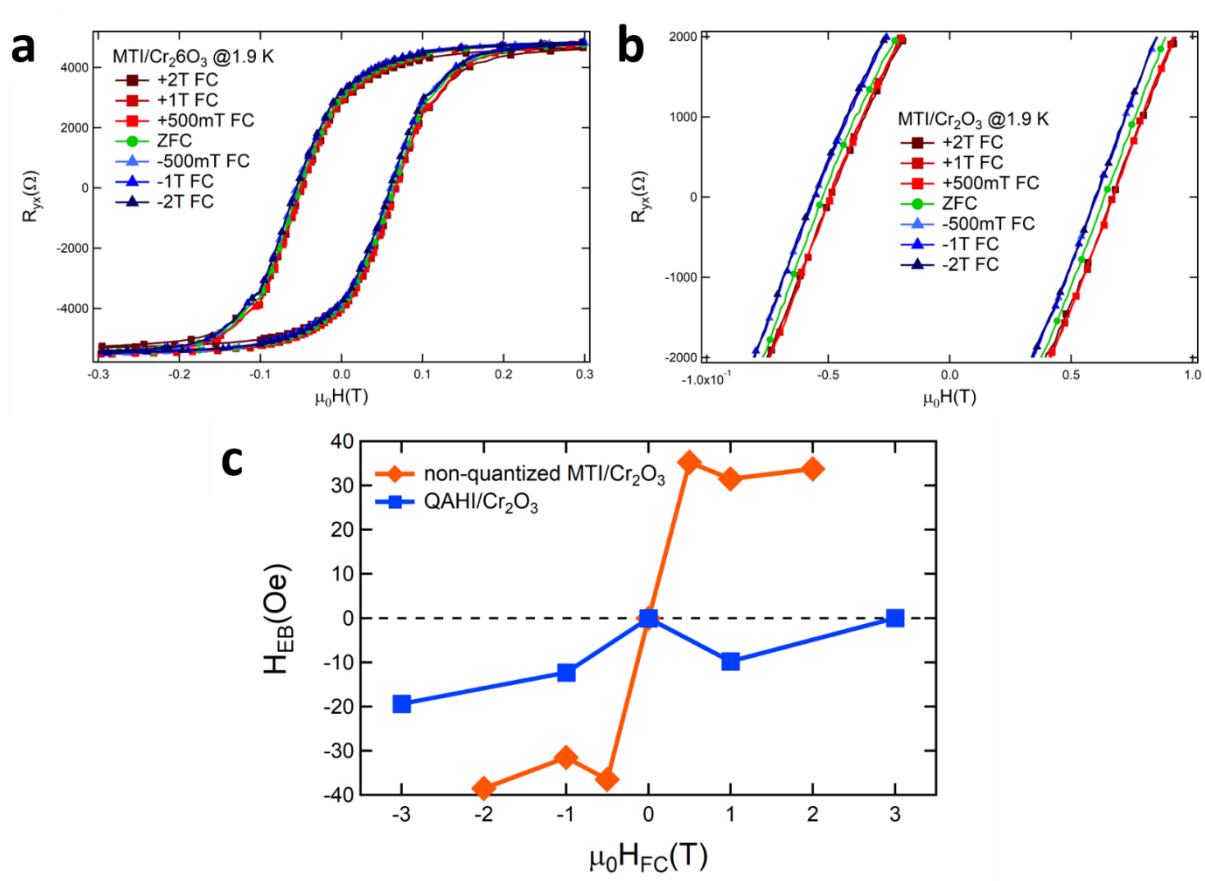

Figure 4-3 Exchange bias effect in non-quantized MTI/Cr_2O_3 heterostructure. (a) Hysteresis loops of the non-quantized MTI/Cr_2O_3 heterostructure after different magnetic field cooling. Positive field direction is defined the same as the thin film growth direction. (b) Expanded version of (a) to highlight the exchange bias effect. (c) Summarized exchange bias magnitude in Figure 4-2(a) and Figure 4-3(a): No obvious exchange bias is observed in the QAH insulator/Cr_2O_3 while a clear positive exchange bias is observed in the non-quantized MTI/Cr_2O_3 structure.

Here, we need to point out that although similar field-cooling measurements were performed, we observed large variations in terms of the exchange bias effect among these non-quantized MTI/Cr_2O_3 samples. Specifically, while two samples do exhibit exchange biased hysteresis loops as shown in Figure 4-3 and Figure 4-4(c), the magnetic hysteresis loops remain almost symmetric under different field-cooling conditions in two other samples, as highlighted in

Figure 4-4(a) and (b). More strikingly, it is noted that the established exchange bias fields of both samples presented in Figure 4-3 and Figure 4-4(c) shows the same sign with the applied magnetic field as illustrated in Figure 4-4(d). That is called positive exchange bias namely when a positive field is applied, the hysteresis loop shifts to the positive field direction, and vice versa. Such positive exchange bias is usually a result of anti-parallel alignment between the AFM and MTI's surface spins as shown schematically in Figure 4-4(e)[121].

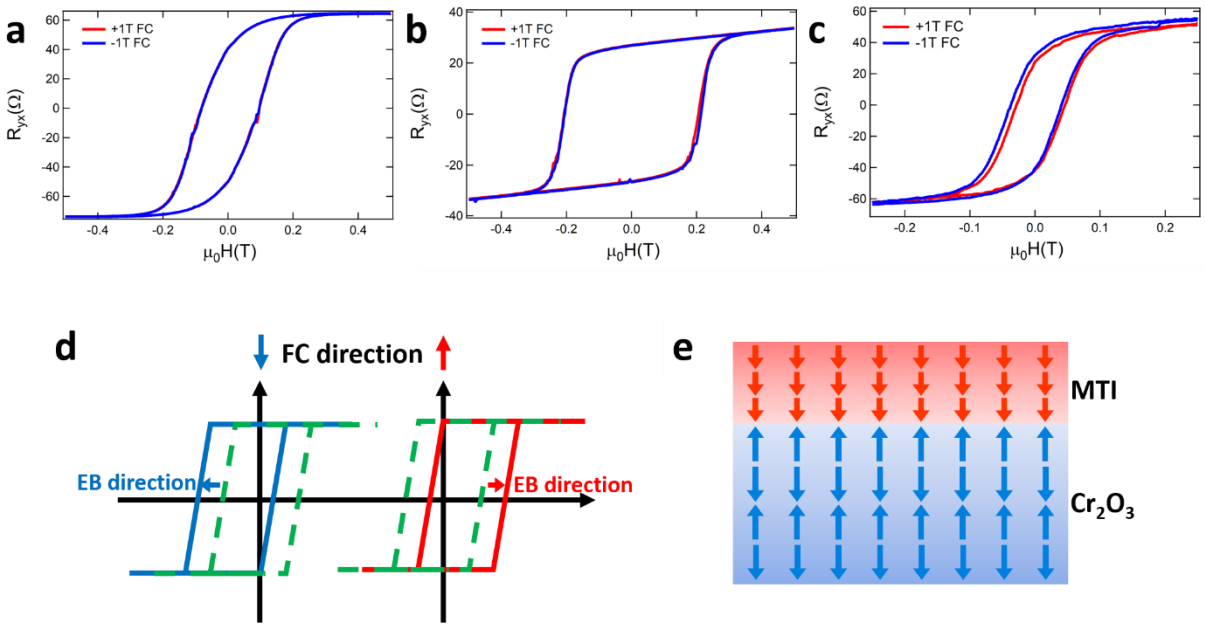

Figure 4-4 Large exchange bias variation across different MTI/Cr_2O_3 samples. (a-c) Hysteresis loops of three different MTI/Cr_2O_3 samples under different field cooling conditions. (d) Schematic drawing of a positive exchange bias. (e) Schematic drawing of spin alignment in the MTI/Cr_2O_3 heterostructure, the positive exchange bias sign is because of the anti-parallel alignment of spins at the interface.

In fact, beyond the sign of exchange bias, the understanding of exchange bias magnitude remained an ongoing challenge for both theorists and experimentalists. Regarding the exchange

bias magnitude, one of the most simple models is $\boldsymbol{H_E = \frac{J_{INT}}{M_{FM} t_{FM}}}$ [122] where $\boldsymbol{H_E}$ is the exchange bias magnitude, $\boldsymbol{J_{INT}}$ is the interface coupling constant, $\boldsymbol{M_{FM}}$ is the ferromagnetic saturation magnetization and $\boldsymbol{t_{FM}}$ is the thickness of the FM layer. However, these models tend to overestimate the $\boldsymbol{H_E}$ by orders of magnitude[122-124]. More complicated models which attempt to account for more detailed parameters including AFM or FM's domain effect[125], grain size distribution[126], random anisotropy in the AFM layer[127], surface roughness[128], uncompensated surface spins[129], etc., often only apply for a specific system. In general, there's no reliable tool to predict a new interface's exchange bias magnitude.

In our MTI/Cr_2O_3 heterostructure, we propose that there are two major factors responsible for the large exchange bias variations. Firstly, it is already confirmed by STEM that there is a very low surface roughness at the MTI/Cr_2O_3 interface, namely the as-grown Cr_2O_3 has a surface roughness around 2 Å and the MBE-grown MTI is essentially a van der Waals material which further reduces the local interface roughness. Consequently, the positive relationship between the surface roughness and the exchange bias magnitude which is widely reported in the literature[128, 130-133], may explain the small (H_{EB} < 10% coercive field) or even close to zero exchange bias observed in our MTI/Cr_2O_3 system. Secondly, much of the variation can be explained by different densities of pinned or uncompensated spins at different MTI/Cr_2O_3 interfaces. Previous study has shown that the Cr_2O_3 surface has a unique surface boundary magnetization state that is related to the exchange bias magnitude[57, 134, 135]. Under such circumstances, when coupled to the MTI, the number of uncompensated spins pinned at the interface is expected to vary among different batches of MTI/Cr_2O_3 samples and lead to the exchange bias variations.

4.1.3. Polarized neutron reflectometry measurement of the heterostructure

To directly examine the magnetic coupling at the interface, we used polarized neutron reflectometry (PNR) to determine the depth-resolved picture of the magnetization which allows us to understand the strength and range of the interfacial coupling across the MTI/Cr_2O_3 interface. PNR measurements were performed using the PBR instrument at the NIST Center for Neutron Research as described in the methods section, and samples were again field cooled from above the Cr_2O_3 T_N. The neutron measurement later was conducted at 6 K with an in-plane magnetic field applied ranging from 700 mT to 3 T.

Figure 4-5(a) shows the spin-dependent neutron reflectivities alongside the best fit for a measurement performed at the lower field of 700 mT. The fits shown, which are an extremely good match for the data, are generated using the theoretical model shown in Figure 4-5(b) and illustrated schematically in Figure 4-5(e). All models reveal extremely high-quality interfaces between the Cr_2O_3 and MTI, in agreement with the HRSTEM shown in Figure 2-15(b). Interestingly, the best fit shown in Figure 4-5(b) exhibits a non-uniform magnetization profile with a suppression of the magnetic scattering length-density (SLD, which is directly proportional to the magnetization) near the MTI/Cr_2O_3 interface. Since modeling of reflectivity data often produces multiple degenerate models which describe the data equally well, we evaluated a variety of candidate profiles. Specifically, we considered models with uniform and linearly varying magnetization profiles, as well as models exhibiting an exponential decay towards a bulk-like value or models with an interfacial dead layer. These alternative models are described and summarized in detail in the supplemental information. In all cases considered, we found that only a non-uniform magnetic SLD profile with suppressed magnetization at the MTI /Cr_2O_3 interface

can properly capture the spin asymmetry shown in Figure 4-5(c-d), where the spin asymmetry is defined as the difference between the spin-up and spin-down reflectivity normalized by their sum.

This finding is consistent in both the low field (700 mT) condition shown above and in the 3 T case, so that a non-uniform magnetization is required to properly describe the splitting between the reflectivity of the two spin states. Only the linear or exponential models, which yield qualitatively similar profiles due to the smearing associated with long-range interface roughness, can appropriately describe the data at both fields, with a slight preference for the linear model. Therefore, we conclude that applying an in-plane field results in a continuous magnetization gradient within the films.

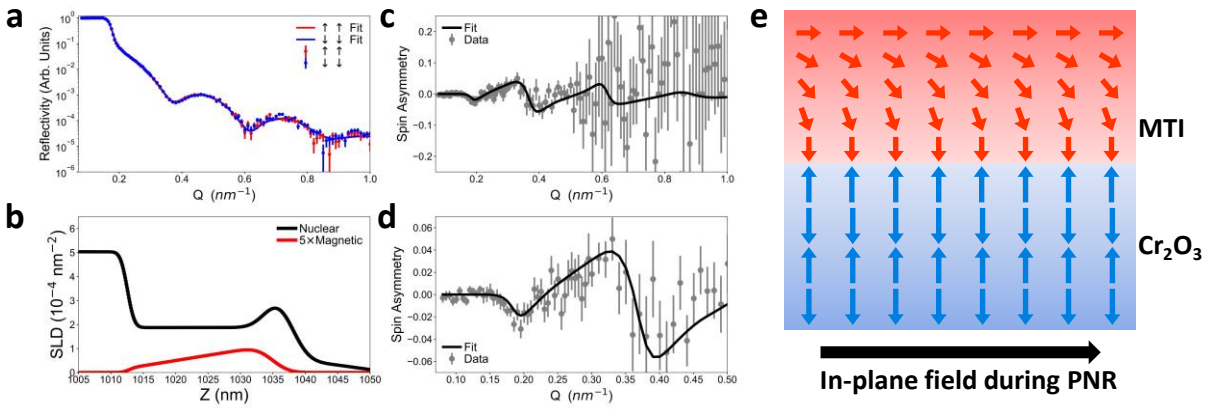

Figure 4-5 PNR measurement of the MTI/Cr_2O_3 structure. (a) Spin dependent polarized neutron reflectometry from an MTI/1 µm Cr_2O_3/Sapphire film in an applied in-plane field of 700 mT alongside the best fit generated by (b) the nuclear and magnetic depth profile model. (c) Spin asymmetry and (d) zoomed in view under these same conditions, again alongside the best fit model. (e) Schematic drawing of magnetic depth profile shown in (b) where an in-plane field was applied.

Given the relatively small magnitude of the exchange bias (H_{EB} < 100 Oe) reported in these films, it is surprising that the interface effects persist up to 3 T. We therefore propose that the non-

uniform gradient may be caused by the interactions between the MTI and the bulk AFM structure rather than solely coupling to uncompensated pinned spins. During the PNR measurement, due to the selection rules for magnetic neutron scattering which mandates that any magnetization component along the out-of-plane axis is invisible to neutrons i.e., will not contribute to the observed magnetic scattering length density. Hence, an in-plane field was applied to pull the MTI's magnetization into the in-plane direction to allow observation of the magnetic moment. The reduced magnetic SLD close to the MTI/Cr_2O_3 boundary according to the PNR fits indicates a decreasing in-plane magnetic moment component in the MTI towards the interface. Here we speculate that the exchange coupling between the MTI and Cr_2O_3 at the interface locks the MTI magnetization more strongly along the out-of-plane axis, resulting in an exchange-spring like structure under the influence of the in-plane field as the MTI magnetization rotates from in-plane direction (large SLD) towards out-of-plane direction (small SLD) when approaching the MTI/Cr_2O_3 interface. The reduction of the magnetization slope at higher field, shown in the supplemental information, also supports this interpretation. In the case of exponential or dead-layer models, applying a larger in-plane field results in a shorter exponential decay length or a smaller dead layer respectively, both corresponding to a more uniform magnetization profile which does not provide the most accurate fitting towards the PNR data. Alternative explanations, such as nonuniform Cr-dopant density, can be ruled out by energy dispersive X-ray spectroscopy which showed uniform Cr atom distribution in the structure as shown in Figure 4-6 and the fact that past PNR measurements of MTI films grown in the same chamber have never required such magnetization gradients to fit the data. Thus, the PNR data agrees with the fact that there exists extremely strong exchange coupling between the antiferromagnet and the MTI layers, and such

strong coupling can potentially lead to the manipulation of the quantum anomalous Hall states and other topological properties.

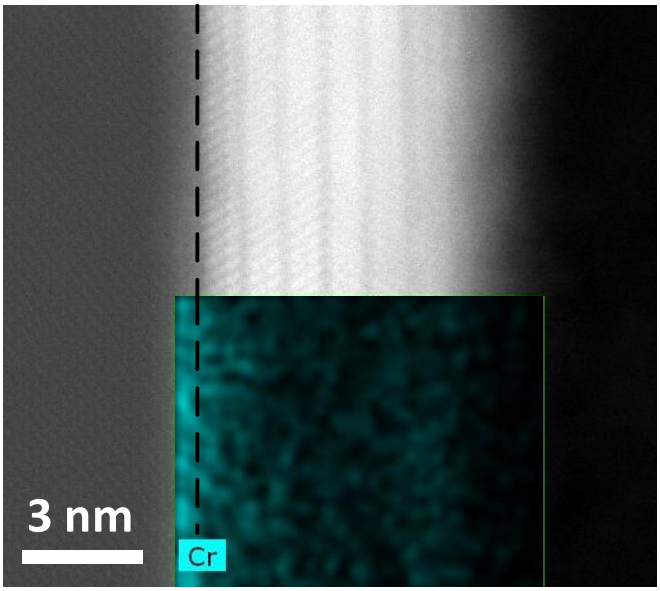

Figure 4-6 Superimposed HADDF and EDX elemental mapping of Cr in MTI/Cr_2O_3 structure. The Cr atom distribution in MTI is uniform.

4.1.4. Summary of Chapter 4.1

In conclusion, we have successfully realized quantum anomalous Hall effect in an MTI/Cr_2O_3 heterostructure. We further confirmed the exchange coupling between MTI and Cr_2O_3 by both the field-cooling magnetometry and the PNR measurements. The exchange bias effects observed in different field-cooling schemes revealed a strong anti-parallel coupling of magnetic moments across the interface. The PNR result further supported the coupling scenario by showing the detailed magnetization profile. Such magnetically coupled quantum transport system provides us an additional degree of freedom in terms of manipulating the quantum states which can be potentially used in spintronics and low-dissipation electronics.

4.2. Topological insulator/CrSe heterostructure

Introducing ferromagnetism into a TI via the magnetic proximity effect (MPE) of an adjacent magnetically ordered material has been identified as an important route towards breaking TI's time-reversal symmetry without impurity dopants. We have exchange-coupled the TI $(BiSb)_2Te_3$ (BST) with the antiferromagnetic CrSe, yielding MPE-induced ferromagnetism with Curie temperature of approximately 120 K when CrSe is grown on top of $(Bi,Sb)_2Te_3$, but not in the inverse bilayer structure with CrSe on the bottom. Magnetic X-ray spectroscopy suggests the MPE is dependent on a Cr-terminated CrSe surface, which results in Cr^{3+} surface states which experiences double-exchange interactions with the Cr^{2+} in bulk CrSe. This double-exchange stabilizes strong ferromagnetic order localized at the interface and magnetically polarizes Sb band in vicinity of the Fermi-level with ferromagnetic coupling to interfacial Cr spins. In contrast, Se-termination in the inverse bilayer results in no detectable MPE, reflecting the asymmetric $(Bi,Sb)_2Te_3$ top and bottom interface upon being sandwiched by two CrSe layers.

4.2.1. Magnetic proximity and exchange bias effects in TI-CrSe heterostructure

As demonstrated in Chapter 2.4.2, high quality TI-CrSe heterostructure can be grown using MBE technique on GaAs(111)B substrate. The growth order of the structure can be switched freely with high interface quality guaranteed after optimizing the growth recipe. To understand the interaction between the two material systems, we first calibrated the two independently using transport method. The 10 nm CrSe thin film is almost two orders of magnitude more resistive than 6 nm $(BiSb)_2Te_3$ thin films as shown in Figure 4-7. This kind of resistance mismatch allows us to

use transport method to study the heterostructure and its magnetic proximity effect because almost all the current will flow through the TI layer at low temperature.

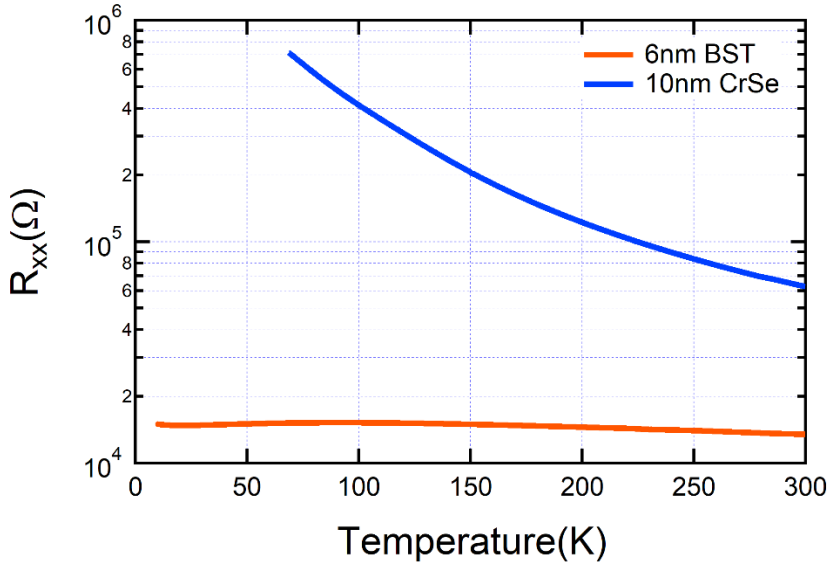

Figure 4-7 Temperature dependent longitudinal resistance of pure CrSe and BST thin films. Here we present three heterostructures including the sandwiched trilayer CrSe (3 nm)/TI (6 nm)/CrSe (6 nm)/GaAs structure and the bilayer CrSe (3 nm)/TI (6 nm)/GaAs, TI (5 nm)/CrSe (6 nm)/GaAs structures.

In the trilayer structure, we first verified the existence of magnetic proximity effect using transport measurement. A standard milli-meter sized Hall bar was fabricated using the same technique described in the previous chapters. We monitored the thin film's anomalous Hall resistance at different temperatures. Strikingly, even though the $(BiSb)_2Te_3$ was not doped with any magnetic elements, a pronounced anomalous Hall resistance showed up when the temperature was cooled down to 80 K as shown in Figure 4-8(a). More interestingly, the hysteresis loop of the anomalous Hall resistance shifted in the horizontal direction when different field cooling field was applied as shown in Figure 4-8(b). The magnitude of the loop shifting is above 1000 Oe which is

one order of magnitude more than the case in MTI/Cr_2O_3 structure. The sign of the exchange bias is negative meaning positive field cooling results hysteresis loop shifting to negative field direction which is opposite to the case in MTI/Cr_2O_3 structure. This result suggests the parallel magnetic moment alignment at the interface.

The above observation confirmed the existence of magnetic proximity effect between TI and CrSe because the transport signal at low temperature can be viewed as solely originated from the TI layer. In the meantime, the proximity induced ferromagnetism is coupled to the AFM order of the CrSe layer which results the pronounced exchange bias effect.

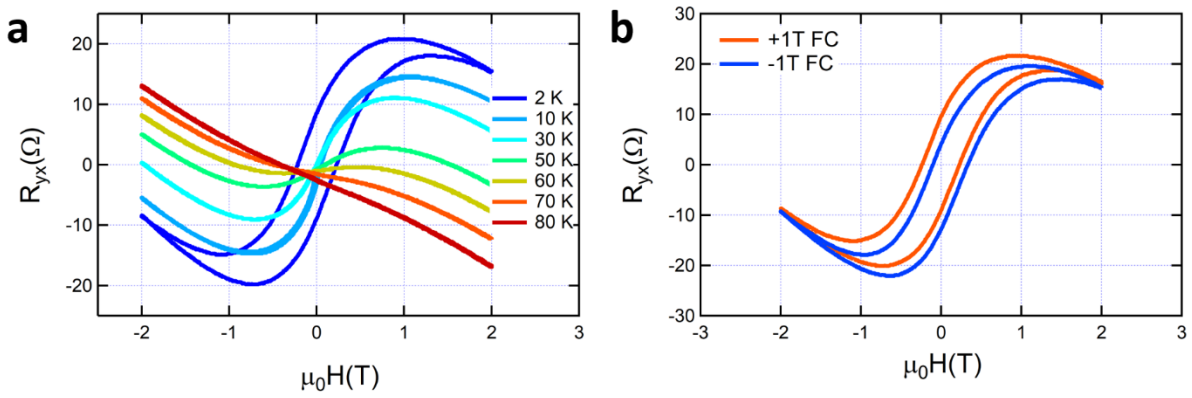

Figure 4-8 Anomalous Hall and exchange bias effect in the CrSe-BST-CrSe trilayer structure. (a) Temperature dependent anomalous Hall resistance in the trilayer structure. (b) Negative exchange bias effect in the trilayer structure by using ±1 T out-of-plane field cooling from room temperature to 2 K.

Although the proximity induced ferromagnetism arising from the trilayer structure is expected to be a result from two equal contributions of the two CrSe-BST interfaces due to the symmetric structure, surprising results emerge when a pair of CrSe/BST bilayers with opposite stacking order are characterized. Temperature dependent anomalous Hall resistance result is

presented in Figure 4-9 for the two structures. In Figure 4-9(a), the CrSe sits on top of the BST layer and the order is reversed in (b). We will refer (a) structure as the "top" bilayer and (b) as the "bottom" bilayer structure based on the position of the CrSe layer in the heterostructure stack. The two bilayer structures demonstrate very different magnetic field responses at low temperature. In the "top" bilayer, an obvious hysteresis loop shows up at a similar temperature (~ 80 K) as the trilayer structure indicating similar physical origins of the magnetic proximity effect. However, the Hall resistance is linear in the "bottom" bilayer structure across a wide temperature range indicating the non-existence of long-range ferromagnetism in this structure.

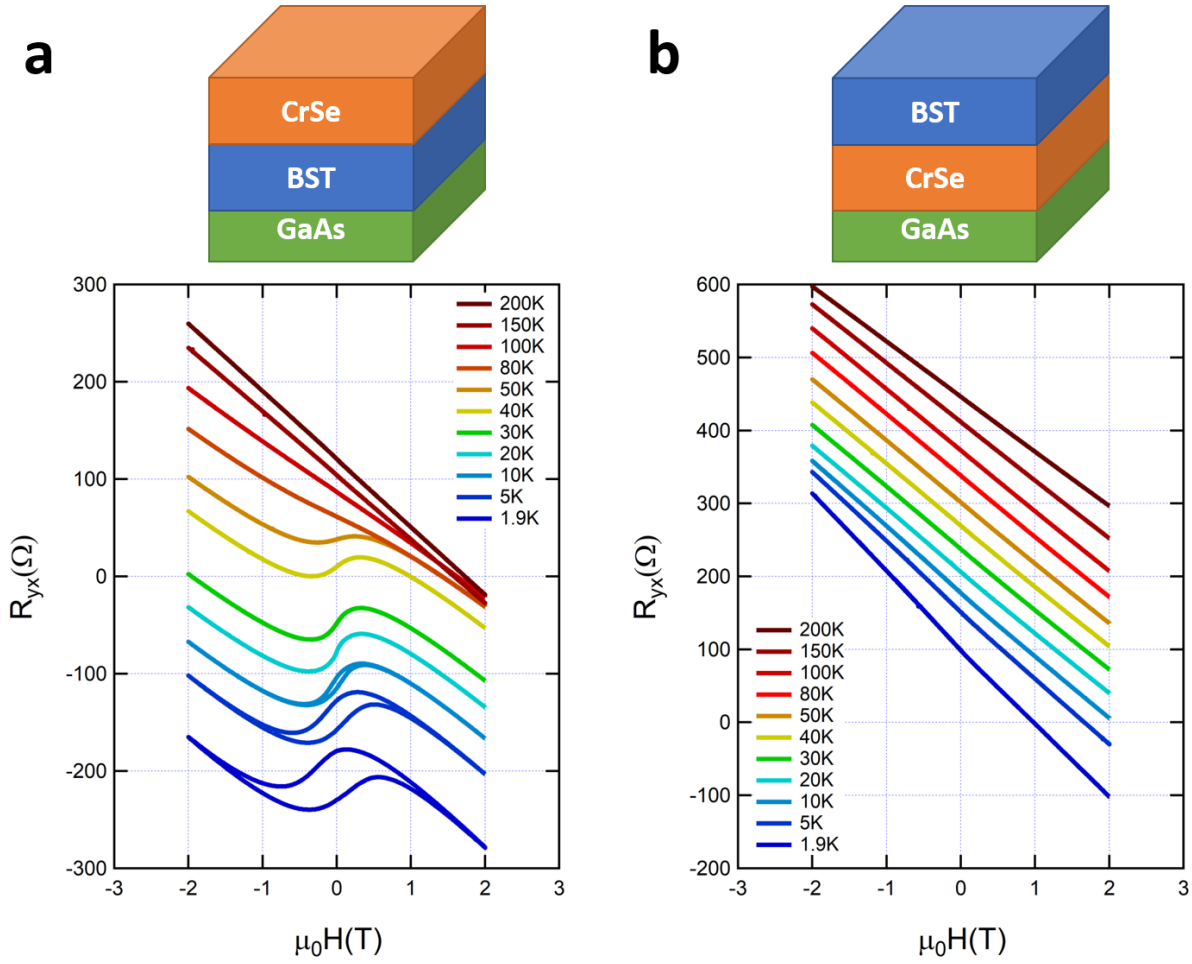

Figure 4-9 Different magnetic responses by switching the growth order of BST and CrSe. (a) Top: schematic drawing of the CrSe/BST/GaAs "top" bilayer structure. Bottom: temperature dependent anomalous Hall resistance in the "top" bilayer structure showing magnetic proximity effect. (b) Top: schematic drawing of the BST/CrSe/GaAs "bottom" bilayer structure. Bottom: temperature dependent anomalous Hall resistance in the "bottom" bilayer structure showing negligible magnetic proximity effect.

Cr inter-diffusion is one possibility that may lead to the observation of the induced magnetism but is unlikely the case in our structure due to the following reasons: 1. The magnetic ordering temperature of the trilayer and "top" bilayer structure is much higher than the Cr-doped TI system which is only around 30 K. 2. Inter-diffusion should happen at both CrSe-TI interfaces;

however, the magnetic proximity effect can only be observed in the "top" bilayer structure. Such kind of dramatic magnetic response difference is indicative of a system where the details of the interface are critical to the resulting magnetic states.

4.2.2. CrSe thickness dependent study

One way to better understand the heterostructure is by growing different thicknesses of AFM on top of the TI layer and study the magnetic field response. The strengthening of the AFM order by having thicker AFM may reveal the origin of the magnetic proximity effect. Here we prepare a set of "top" bilayer structures with four different CrSe thicknesses (1 nm, 3 nm, 7 nm and 12 nm) and a fixed TI thickness (8 QLs). We used ±1 T out-of-plane magnetic fields in our field-cooling and exchange bias effect measurement as shown in Figure 4-10 for all 4 samples. The first thing we notice is that in the 1 nm CrSe structure, magnetic proximity effect disappears with a linear Hall resistance as shown in Figure 4-10(a). This shows that to have the magnetic proximity effect, a well-established AFM order is required. This also excludes the doping or interfacial layer effect from the origin of magnetic responses because 1 nm of CrSe should be able to dope the TI or form an interfacial layer. When further increasing the CrSe thickness to 3 nm or above, robust anomalous Hall hysteresis loops show up as shown in Figure 4-10(b-d). Also, by using different field cooling schemes, we are able to see a large negative exchange bias effect. The coercive fields of the three thicknesses almost remain the same at 1.9 K (6000 Oe for 3 nm, 5900 Oe for 7 nm, 5400 Oe for 12 nm). However, the exchange bias field shows positive relationship with the AFM thickness (750 Oe for 3 nm, 3100 Oe for 7 nm, 4200 Oe for 12 nm). Both results are not surprising since the magnetic proximity effect is an interfacial effect which should not rely on the thickness of the AFM layer once it is established. However, the exchange bias effect is

closely related to the AFM order and thickness during field cool that is a more established AFM order or thicker AFM layer will generate more pronounced exchange bias effect which matches our observation results.

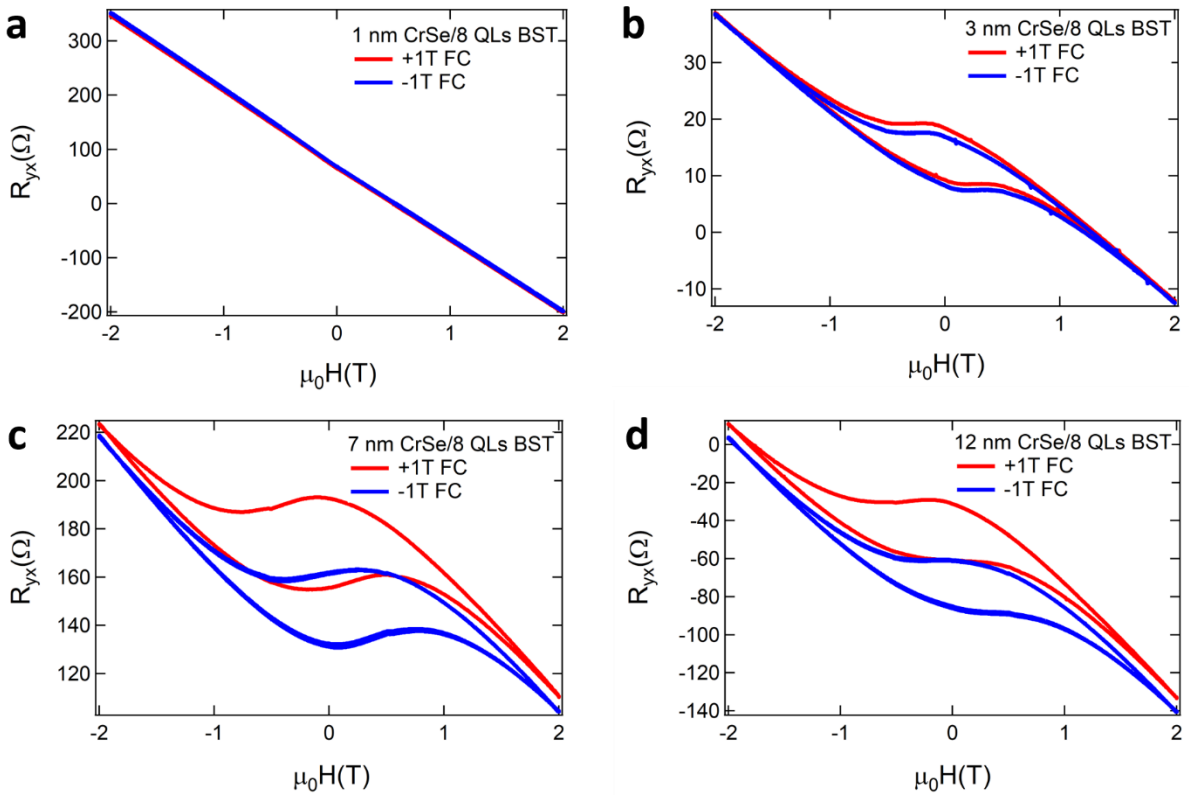

Figure 4-10 Exchange bias effect in different thicknesses of CrSe/TI structures. (a) No obvious proximity effect in 1 nm CrSe/8 QLs BST. (b-d) Both magnetic proximity and exchange bias effect can be seen from CrSe thickness = 3 nm to 12 nm. The exchange bias magnitude becomes more pronounced in thicker CrSe structures.

4.2.3. X-ray absorption spectroscopy of the CrSe-TI heterostructure

To better understand the physical origin of this phenomenon and provide better insight towards high temperature magnetic TI with robust ferromagnetic order, we applied two techniques

including soft X-ray absorption spectroscopy (XAS) and PNR that are very powerful in terms of resolving the ferromagnetism down to atomic level and magnetic moment distributions in a heterostructure. Combining these two techniques, we can reconstruct an element and layer-resolved picture of the heterostructures.

Here we first show the XAS result in Figure 4-11, which describes the XAS and X-ray magnetic circular dichroism (XMCD) at the Cr $L_{2,3}$-edge. The XAS and XMCD data were acquired using total electron yield mode at 10 K in an applied out-of-plane field of 4 T. Incident X-rays were switched from a circular polarization of ± 0.9 and traveled along the applied field direction. The XMCD was constructed from consecutive energy scans with opposite polarization.

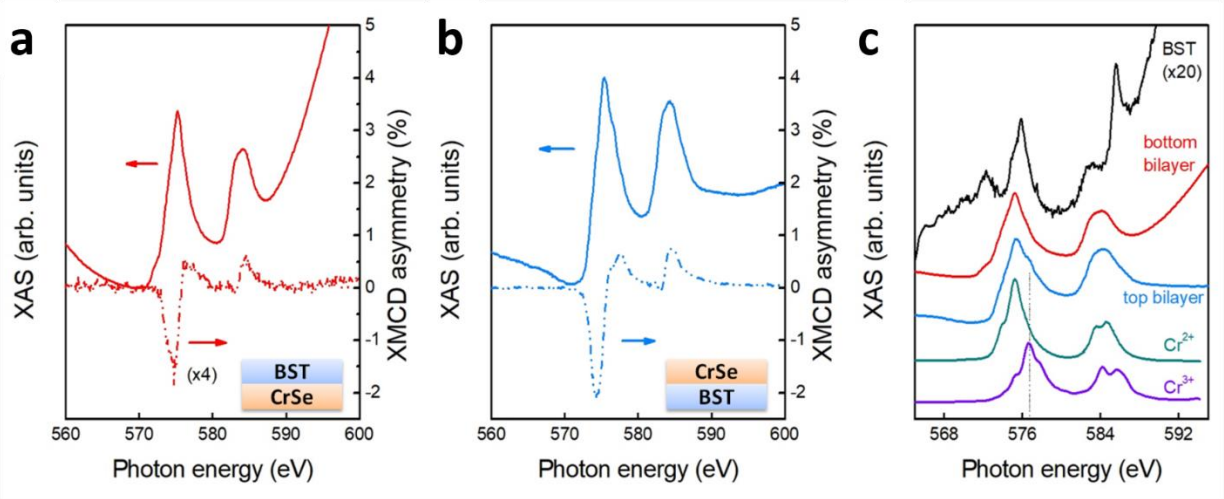

Figure 4-11 Electronic and magnetic structures of the two bilayer heterostructures probed by X-ray magnetic spectroscopy. (a-b) XAS and XMCD asymmetry at Cr $L_{2,3}$-edge in bottom and top bilayer taken at 10 K, respectively. (c) XAS at Cr $L_{2,3}$-edge for bottom and top bilayer alongside reference spectra of BST control sample, Cr^{2+}, and Cr^{3+} in Cr-doped Bi_2Se_3[136]. Herein, we referred the Cr^{2+} and Cr^{3+} reference spectra from the calculation results of A. I. Figueroa et al.'s work[136]. XAS of BST is to exhibit Te $M_{4,5}$-edge in order to define the Te electronic states deviating from Cr $L_{2,3}$-edge, which is 20 times smaller than Cr signal. Cr^{3+} contribution on XAS is as guided by the dash line.

As shown in Figure 4-11(a) and (b), although both the "top" and "bottom" bilayers yielded detectable XMCD on the Cr-edges, the dichroism of the "top" bilayer is significantly (at least 4×) larger. In both cases, we attribute the implied net Cr magnetization to a combination of pinned defects in the CrSe bulk and uncompensated spin at the interface [137], both of which will be probed via the surface-sensitive (approximately 5 nm probing depth) total electron yield mode. The large enhancement of the Cr magnetization in the top bilayer is particularly revealing that the top and bottom interfaces are indeed magnetically asymmetric. We conclude that the increased magnetization in the "top" bilayer indicates additional spin-polarization of the Cr at the CrSe/BST interface, yielding stronger ferromagnetic exchange interactions and supporting an MPE in the TI layer. On the other hand, a lack of spin-polarized Cr at the BST/CrSe interface weakens the interlayer exchange to the point where the anomalous Hall effect cannot be observed.

To better understand this issue, we examine the fine structure via XAS line shape shown in Figure 4-11(c), which compares the Cr $L_{2,3}$-edge XAS for the bottom and top bilayers alongside reference spectra of BST, Cr^{2+}, and Cr^{3+} [136, 138]. Here the Cr^{2+} and Cr^{3+} spectra are from A. I. Figueroa et al.'s study in Cr-doped BST [136]. Although the "top" and "bottom" bilayers exhibit relatively similar XAS features, one critical difference emerges. Specifically, a shoulder, highlighted by the dashed line in (c), appears in the XAS of the "top" bilayer which is not present in the "bottom" bilayer. Comparison with the reference spectra reveals that the primary Cr valence in both geometries is from Cr^{2+}, while the shoulder state in the "top" bilayer is associated with Cr^{3+} so that a BST/CrSe is associated with a small amount of mixed-valence Cr. The absence of any Cr^{3+} contribution in the "bottom" bilayer represents a critical difference between the two interfaces, and we believe that ferromagnetic order at the BST/CrSe in the "top" bilayer may be a result of Cr^{2+}-Cr^{3+} double-exchange [139-141].

4.2.4. PNR measurement of the CrSe-TI heterostructure

To examine the magnetization distribution as a function of depth, we performed PNR at 5 K in an applied in-plane field of 700 mT on a bare CrSe film as well as a "top" bilayer structure. Incident and scattered neutrons were polarized spin-up or spin-down with respect to the applied magnetic field, and any net magnetization within the sample will result in a difference in the potential experienced by spin up vs. spin down neutrons so that the two reflectivity curves become split. Thus, the reflected intensity of the non-spin-flip cross sections, shown in Figure 4-12(a-c), is sensitive to both the structural depth profile and the depth profile of the magnetization parallel to the applied field. The nuclear and magnetic scattering length density (SLD) depth profiles were extracted by modeling the PNR using the REFL1D software package for χ^2 optimization[142]. Fitting the PNR reveals that the bare CrSe film is best described with no net magnetization in the bulk and a small magnetization of at most (95% confidence interval) 32 emu/cc at the film surface, as expected given the almost complete absence of any splitting between the spin-up and spin-down reflectivities. We therefore conclude that the majority of the Cr XMCD in Figure 4-11(a) is associated with moments at the interface between CrSe and the BST.

This interpretation is supported by fitting the PNR of a CrSe/BST bilayer with the top geometry, shown in Figure 4-12(d-f). In this case, a clear splitting is observed with a significant nonzero spin asymmetry, defined as the difference between the two spin-dependent reflectivities normalized by their sum. This data may be well described by a magnetization which is localized tightly to the interface, with both proximity-induced magnetism and a small region of ferromagnetically ordered Cr in the CrSe near the interface. It must be noted that although the interfacial model plotted in Figure 4-12(f) yields an excellent fit to the data, the large interfacial

roughness associated with the layered step structure in BST films tends to smear out the magnetization profile in PNR so that it is difficult to determine the precise extent of the magnetic layer. That is, both a magnetic interface and models with a uniformly magnetized CrSe layer (see Figure 4-12(f)) yield extremely similar depth profiles and therefore effectively indistinguishable reflectivity curves. Thus, while PNR demonstrates the emergence of a significant net magnetization consistent with interfacial double-exchange and an MPE in the top geometry bilayer, it cannot uniquely determine the relative moment distribution between the interfacial BST, interfacial CrSe, and bulk CrSe.

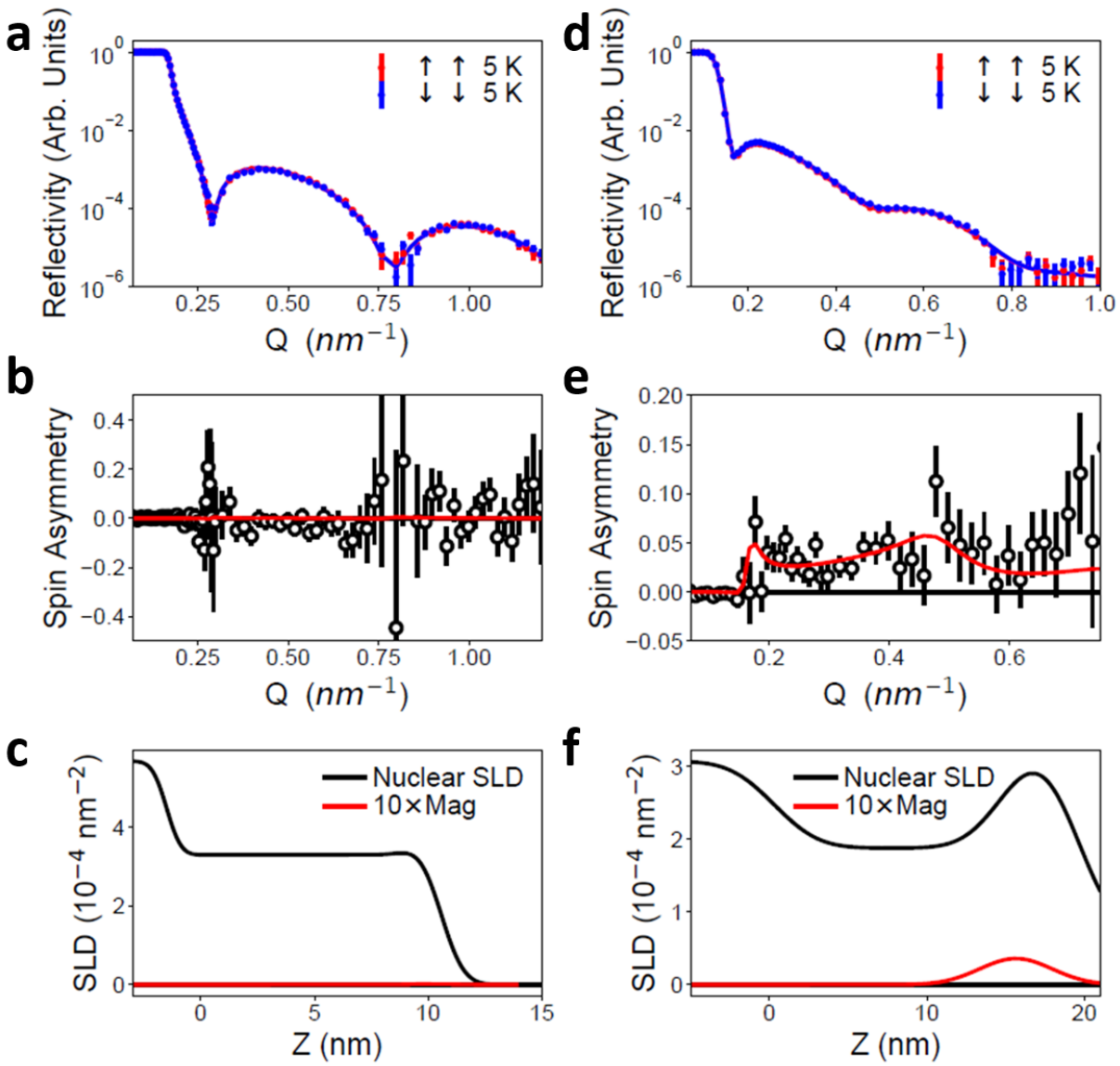

Figure 4-12 Magnetic profile at the interface characterized by polarized neutron reflectivity. (a) Fitted PNR and (b) spin asymmetry for a bare CrSe film. (c) Structural and magnetic depth profile used the generate the fit shown for the CrSe film. (d) Fitted polarized neutron reflectivity and (e) spin asymmetry for a CrSe/$(BiSb)_2Te_3$ heterostructure along with (f) the structural and magnetic depth profile used the generate the fit shown. Measurements were performed in an applied magnetic field of 700 mT after field cooling to 5 K.

4.2.5. XAS/XMCD of the Sb M_5-edge

Having demonstrated the clear emergence of a net magnetization in the "top" bilayer through X-ray and neutron scattering experiments, we can now re-examine the presence and origin of the MPE in this structure. The appearance of Cr^{3+} is attributable to a population of Cr at or adjacent to the van der Waal's gap on BST's surface, specifically the gap at the BST/CrSe interface[136]. The Cr^{3+} may therefore indicate that the CrSe adjacent to BST is terminated by Cr in the top bilayer, leading to a Cr^{3+} state as in the case of Cr-doped TIs. On the other hand, the absence of Cr^{3+} in bottom bilayer reveals that the CrSe is instead terminated by Se in this geometry. Direct contact between BST and Cr combined with the Cr^{2+}-Cr^{3+} double-exchange-mediated ferromagnetic order at the interface then gives rise to an MPE and the observed anomalous Hall effect in the "top" bilayer while the Se-terminated nature of the bottom bilayer inhibits both ferromagnetic double exchange among Cr and direct magnetic exchange between the BST and CrSe, so no indications of MPE are observed. The definitive test of this theory is the direct observation of MPE-induced ferromagnetism through XAS/XMCD on edges associated with the TI, such as Bi, Sb, or Te elements. Although such direct evidence has historically eluded detection in proximity-effect heterostructures, we examined XAS and XMCD at the Sb M_5-edge, as shown in Figure 4-13, and observed a clear difference signal in the case of the top bilayer. Critically, no such XMCD is observed in the bottom bilayer geometry, and the extracted XMCD from Sb in both bilayers are presented together for comparison. The significant XMCD on the Sb M_5-edge suggests the presence of spin-polarized 5p-electrons on Sb[143-145] so that the MPE is confirmed directly. The spin-polarized Sb orbit enables a local moment in the vicinity of the Fermi-level, which electrically dominates the transport property of BST, explaining the sharp difference between top

and bottom interface in the original trilayer structure. It must be noted that the XMCD at Sb M_5 and Cr L_3 feature the opposite asymmetries, pointing up and down, respectively. The result suggests the MPE-induced moment on Sb is ferromagnetically coupled to the neighboring Cr based on their inverse transition symmetries of L_3 and M_5, which are p→d and d→p, respectively[143-145].

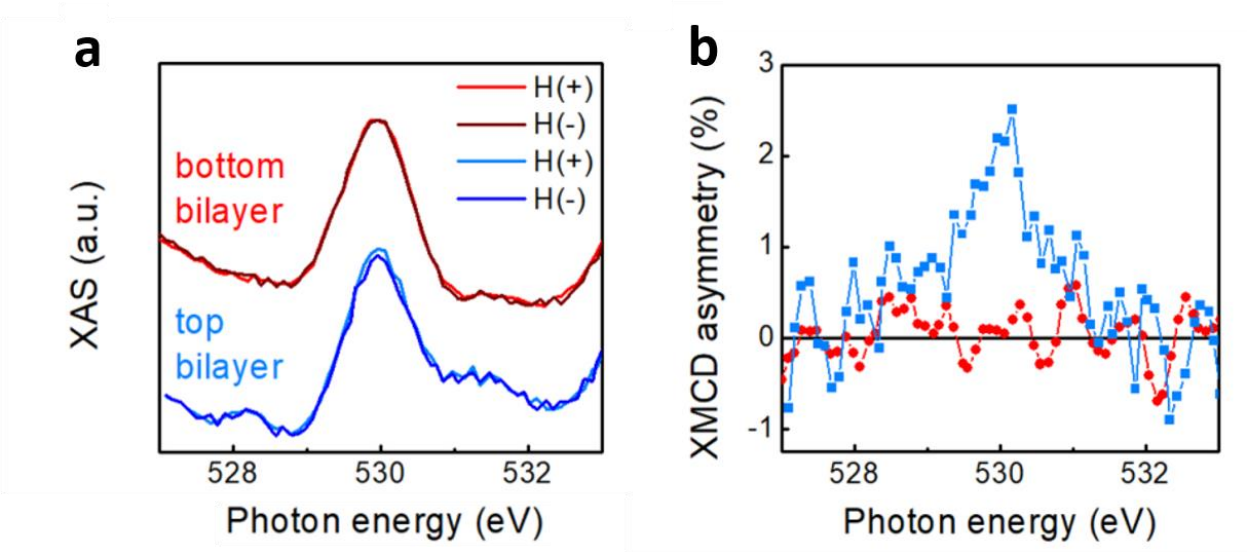

Figure 4-13 MPE-induced ferromagnetism of BST studied by magnetic X-ray spectroscopy. (a) XAS of Sb M_5 edge probed under applying +4 T and -4 T, denoted as H(+) and H(-), in bottom and top bilayer. (b) XMCD asymmetry at Sb M_5 edge gained from the two XAS in (a).

4.2.6. Summary of Chapter 4.2

In conclusion, we have directly demonstrated an MPE induced in BST through interfacial coupling to the AFM CrSe, with direct evidence through magnetic spectroscopy at the Sb M_5-edge. We show that the MPE is strongly dependent on the symmetry of the interface, with BST/CrSe interfaces exhibiting no evidence of an MPE while BST/CrSe interfaces are magnetized and support an MPE. X-ray magnetic spectroscopy and neutron scattering support a picture in which

Cr^{3+} is stabilized through Cr-termination of the BST/CrSe interface leading to Cr^{2+}-Cr^{3+} double-exchange-mediated interface ferromagnetism in CrSe which couples to the BST. On the other hand, BST/CrSe interfaces appear to be Se-terminated, inhibiting the interlayer exchange coupling. This work identifies key requirements necessary to activate an MPE at the interface of a BST-based exchange-coupled bilayer and provides an ideal model system in which to explore the fundamental mechanisms behind designing these systems for room-temperature functionality.

4.3. Summary of Chapter 4

In this chapter, we studied two antiferromagnet systems combined with topological insulator. The antiferromagnet Cr_2O_3 thin film grown on sapphire substrate can serve as a high-quality substrate for TI and magnetic TI growth, the superior quality of the epilayer grow on this substrate facilitates the first observation of quantum anomalous Hall effect on a magnetic substrate. While investigating the magnetic interaction between Cr_2O_3 and MTI systems, we discovered that the exchange bias effect might not be the best indicator to identify and quantify the interaction strength between the two. We in fact observed a large exchange bias magnitude variation in this heterostructure. The possible reasons for this kind of variation may be the atomically flat MTI/Cr_2O_3 interface and the unique boundary magnetization in Cr_2O_3. In the meantime, for those samples that showed exchange bias effect, we observed a positive exchange bias which confirmed the detailed magnetic moment alignment at the material boundary. Since exchange bias effect cannot provide accurate magnetic interaction information in this system, we used PNR technique to directly probe the magnetic moment's depth profile in the heterostructure. In this measurement, we noticed a magnetic moment shift towards the interface which is likely a result of out-of-plane

magnetization pinning in the MTI layer. Such kind of pinning confirms the magnetic coupling between MTI and Cr_2O_3.

The second antiferromagnet we studied is CrSe which is a noncolinear AFM that can be grown in our MBE chamber. In this system, we studied the unique AFM proximity effect when combined with undoped TI system. Magnetic proximity effect is particularly interesting in today's TI research field because it might be able to solve the critical dopant fluctuation problem when the magnetic elements was doped into the TI system during MBE growth. In CrSe/TI system, we successfully observed the AFM induced proximity effect which successfully raised the Curie temperature of the system by 3 times. In the meantime, we observed a large exchange bias effect in this heterostructure that may potentially be useful in TI based spintronics devices. In addition, we used advanced X-ray and neutron techniques to investigate the origin of the magnetic proximity effect and discovered a unique interface-dependent proximity phenomenon. This work greatly helps our understanding of the physical origin of magnetism in Bi_2Te_3 based TI family and can be a useful material platform to study AFM based TRS-breaking physics.

Chapter 5

Conclusion and Perspective

In this dissertation, we first demonstrate our material growth capability using the MBE technique. By using this method, we are able to achieve high quality single crystal topological insulators with flexible doping and thickness control. Beyond the conventional semiconductor substrate (GaAs in our case), we explore the possibility of growing topological insulator on different kinds of substrates including mica and Cr_2O_3, which all resulted high quality growth. In the meantime, we can prepare TI-AFM heterostructures including TI/Cr_2O_3 and TI/CrSe. All of the materials are structurally characterized using TEM for better understanding the interface quality.

Utilizing the high-quality TI thin films, we are able to realize the quantum anomalous Hall effect in the Cr-doped $(BiSb)_2Te_3$ materials grown in our MBE chamber. Beyond the first experimental observation of the QAHE below the 2D limit reported by Chang *et al.*,[35] we realized the QAHE in a 10 QLs magnetic TI thin film beyond the 2D limit and in a milli-meter sized device which demonstrates the scale-invariant nature of the QAH states. Additionally, utilizing the accurate control of magnetic TI thickness, we demonstrate the introduction trivial insulating gap into the QAH system through thinning down the TI below its 2D limit (6 QLs) that generates the vertical quantum confinement. The additional insulating state, as a result, demonstrates a unique metal-to-insulator transition behavior in the thin TI device.

Though the dissipationless QAH states emerge at zero external field show a major advantage over the quantum Hall effect which requires a large external magnetic field, the occurring temperature of the QAHE is still low (< 1 K) in the current material system. We dive into this subject trying to understand the temperature limiting factors of the QAHE in the Cr-doped $(BiSb)_2Te_3$ materials in Chapter 3.3. By growing different thicknesses of magnetic TI and using different doping strategies, we are able to identify that the temperature limiting factors have thickness dependence. We show that in the hybridized 2D limit (6 QLs), the QAH temperature is limited by the formation of superparamagnetic states. By introducing modulation doping of Cr element at the top and bottom surfaces, we can increase the QAH occurring temperature and stabilize the ferromagnetism near zero field. In thicker TI materials, the QAH state is limited by the bulk effect and the activation gap size is vulnerable to the vicinity of the Fermi level to the bulk valence band. During this study, we also noticed an interesting relationship between the Cr-doping strategy and the metal-to-insulator transition behavior. The interplay between the two may give us an additional dimension of freedom to manipulate other quantum phases, *e.g.*, chiral Majorana edge mode in this material system.

In Chapter 4, we investigate integrating the QAH insulator or TI with two antiferromagnet systems. The QAH states are closely related to the TI host's magnetic state. By forming heterostructures with an AFM material, we gain an additional degree of freedom to control TI's magnetic state other than sweeping the external magnetic field. We demonstrate the first observation of the QAHE on a magnetically-ordered substrate Cr_2O_3. And with the help of exchange bias and PNR technique, we successfully identified the existence of magnetic coupling and its detailed configurations. In the TI-CrSe system, since we can grow both materials in our MBE chamber, we can form different kinds of heterostructures and stacking orders freely. In this

heterostructure, we discovered a unique interface-dependent AFM magnetic proximity effect that raises the TI's magnetic ordering temperature by three times. In the meantime, we observed a giant exchange bias effect showing a robust coupling between TI's surface magnetic order and the CrSe layer's AFM order. Both findings can potentially be used to manipulate the dissipationless QAH states.

In summary, all the results presented in this dissertation show promising prospects towards realizing the QAHE at higher temperature and effective means to control and manipulate the QAH states. The understanding of the material growth, temperature limiting factors in the current material system and the TI-AFM coupling mechanism are critical to help searching for a better QAH host. The QAH states, which have great advantages over the quantum Hall states in terms of zero magnetic field requirement and the superconductivity in terms of more clear physics known to the human beings, have a bright future in delivering dissipationless electron transport at room temperature and being packed into a common electronic device.

References

[1] X. L. Qi, T. L. Hughes, and S. C. Zhang, "Topological field theory of time-reversal invariant insulators," *Physical Review B*, vol. 78, Nov 2008.

[2] M. Z. Hasan and C. L. Kane, "Colloquium: Topological insulators," *Reviews Of Modern Physics*, vol. 82, pp. 3045-3067, Nov 8 2010.

[3] X. L. Qi and S. C. Zhang, "Topological insulators and superconductors," *Reviews Of Modern Physics*, vol. 83, Oct 14 2011.

[4] S. Murakami, N. Nagaosa, and S. C. Zhang, "Dissipationless quantum spin current at room temperature," *Science*, vol. 301, pp. 1348-1351, Sep 5 2003.

[5] J. Sinova, D. Culcer, Q. Niu, N. A. Sinitsyn, T. Jungwirth, and A. H. MacDonald, "Universal intrinsic spin Hall effect," *Physical Review Letters*, vol. 92, Mar 26 2004.

[6] Y. K. Kato, R. C. Myers, A. C. Gossard, and D. D. Awschalom, "Observation of the spin hall effect in semiconductors," *Science*, vol. 306, pp. 1910-1913, Dec 10 2004.

[7] C. L. Kane and E. J. Mele, "Z(2) topological order and the quantum spin Hall effect," *Physical Review Letters*, vol. 95, Sep 30 2005.

[8] C. L. Kane and E. J. Mele, "Quantum spin Hall effect in graphene," *Physical Review Letters*, vol. 95, Nov 25 2005.

[9] Y. G. Yao, F. Ye, X. L. Qi, S. C. Zhang, and Z. Fang, "Spin-orbit gap of graphene: First-principles calculations," *Physical Review B*, vol. 75, Jan 2007.

[10] B. A. Bernevig, T. L. Hughes, and S. C. Zhang, "Quantum spin Hall effect and topological phase transition in HgTe quantum wells," *Science*, vol. 314, pp. 1757-1761, Dec 15 2006.

[11] M. Konig, S. Wiedmann, C. Brune, A. Roth, H. Buhmann, L. W. Molenkamp, *et al.*, "Quantum spin hall insulator state in HgTe quantum wells," *Science*, vol. 318, pp. 766-770, Nov 2 2007.

[12] I. Knez, R. R. Du, and G. Sullivan, "Evidence for Helical Edge Modes in Inverted InAs/GaSb Quantum Wells," *Physical Review Letters*, vol. 107, Sep 19 2011.

[13] S. F. Wu, V. Fatemi, Q. D. Gibson, K. Watanabe, T. Taniguchi, R. J. Cava, *et al.*, "Observation of the quantum spin Hall effect up to 100 kelvin in a monolayer crystal," *Science*, vol. 359, pp. 76-79, Jan 5 2018.

[14] L. Fu, C. L. Kane, and E. J. Mele, "Topological insulators in three dimensions," *Physical Review Letters*, vol. 98, Mar 9 2007.

[15] J. E. Moore and L. Balents, "Topological invariants of time-reversal-invariant band structures," *Physical Review B*, vol. 75, Mar 2007.

[16] R. Roy, "Z(2) classification of quantum spin Hall systems: An approach using time-reversal invariance," *Physical Review B*, vol. 79, May 2009.

[17] D. Hsieh, D. Qian, L. Wray, Y. Xia, Y. S. Hor, R. J. Cava, *et al.*, "A topological Dirac insulator in a quantum spin Hall phase," *Nature*, vol. 452, pp. 970-U5, Apr 24 2008.

[18] H. J. Zhang, C. X. Liu, X. L. Qi, X. Dai, Z. Fang, and S. C. Zhang, "Topological insulators in Bi2Se3, Bi2Te3 and Sb2Te3 with a single Dirac cone on the surface," *Nature Physics*, vol. 5, pp. 438-442, Jun 2009.

[19] Y. Xia, D. Qian, D. Hsieh, L. Wray, A. Pal, H. Lin, *et al.*, "Observation of a large-gap topological-insulator class with a single Dirac cone on the surface," *Nature Physics*, vol. 5, pp. 398-402, Jun 2009.

[20] Y. L. Chen, J. H. Chu, J. G. Analytis, Z. K. Liu, K. Igarashi, H. H. Kuo, *et al.*, "Massive Dirac Fermion on the Surface of a Magnetically Doped Topological Insulator," *Science*, vol. 329, pp. 659-662, Aug 6 2010.

[21] J. S. Zhang, C. Z. Chang, Z. C. Zhang, J. Wen, X. Feng, K. Li, *et al.*, "Band structure engineering in (Bi1-xSbx)(2)Te-3 ternary topological insulators," *Nature Communications*, vol. 2, Dec 2011.

[22] C. Z. Chang, J. S. Zhang, M. H. Liu, Z. C. Zhang, X. Feng, K. Li, *et al.*, "Thin Films of Magnetically Doped Topological Insulator with Carrier-Independent Long-Range Ferromagnetic Order," *Advanced Materials*, vol. 25, pp. 1065-1070, Feb 20 2013.

[23] X. F. Kou, M. R. Lang, Y. B. Fan, Y. Jiang, T. X. Nie, J. M. Zhang, *et al.*, "Interplay between Different Magnetisms in Cr-Doped Topological Insulators," *Acs Nano*, vol. 7, pp. 9205-9212, Oct 2013.

[24] R. Yu, W. Zhang, H. J. Zhang, S. C. Zhang, X. Dai, and Z. Fang, "Quantized Anomalous Hall Effect in Magnetic Topological Insulators," *Science*, vol. 329, pp. 61-64, Jul 2 2010.

[25] X. L. Qi, R. D. Li, J. D. Zang, and S. C. Zhang, "Inducing a Magnetic Monopole with Topological Surface States," *Science,* vol. 323, pp. 1184-1187, Feb 27 2009.

[26] M. R. Lang, M. Montazeri, M. C. Onbasli, X. F. Kou, Y. B. Fan, P. Upadhyaya, *et al.*, "Proximity Induced High-Temperature Magnetic Order in Topological Insulator - Ferrimagnetic Insulator Heterostructure," *Nano Letters,* vol. 14, pp. 3459-3465, Jun 2014.

[27] C. Tang, C. Z. Chang, G. Zhao, Y. Liu, Z. Jiang, C. X. Liu, *et al.*, "Above 400-K robust perpendicular ferromagnetic phase in a topological insulator," *Sci Adv,* vol. 3, p. e1700307, Jun 2017.

[28] Q. L. He, G. Yin, A. J. Grutter, L. Pan, X. Che, G. Yu, *et al.*, "Exchange-biasing topological charges by antiferromagnetism," *Nat Commun,* vol. 9, p. 2767, Jul 17 2018.

[29] Q. L. He, X. F. Kou, A. J. Grutter, G. Yin, L. Pan, X. Y. Che, *et al.*, "Tailoring exchange couplings in magnetic topological-insulator/antiferromagnet heterostructures," *Nature Materials,* vol. 16, pp. 94-100, Jan 2017.

[30] Q. L. He, L. Pan, A. L. Stern, E. C. Burks, X. Y. Che, G. Yin, *et al.*, "Chiral Majorana fermion modes in a quantum anomalous Hall insulator-superconductor structure," *Science,* vol. 357, pp. 294-299, Jul 21 2017.

[31] F. D. M. Haldane, "Model for a Quantum Hall-Effect without Landau-Levels - Condensed-Matter Realization Of the Parity Anomaly," *Physical Review Letters,* vol. 61, pp. 2015-2018, Oct 31 1988.

[32] C. X. Liu, X. L. Qi, X. Dai, Z. Fang, and S. C. Zhang, "Quantum anomalous Hall effect in Hg1-yMnyTe quantum wells," *Physical Review Letters,* vol. 101, Oct 3 2008.

[33] A. Budewitz, K. Bendias, P. Leubner, T. Khouri, S. Shamim, S. Wiedmann, *et al.* (2017, June 01, 2017). Quantum anomalous Hall effect in Mn doped HgTe quantum wells. *arXiv e-prints*. Available: https://ui.adsabs.harvard.edu/\#abs/2017arXiv170605789B

[34] Y.-J. Chien and University of Michigan. Library. Deep Blue. (2007). *Transition Metal-Doped Sb2Te3 and Bi2Te3 Diluted Magnetic Semiconductors*. Available: http://hdl.handle.net/2027.42/57593

[35] C. Z. Chang, J. S. Zhang, X. Feng, J. Shen, Z. C. Zhang, M. H. Guo, *et al.*, "Experimental Observation of the Quantum Anomalous Hall Effect in a Magnetic Topological Insulator," *Science,* vol. 340, pp. 167-170, Apr 12 2013.

[36] J. R. Arthur, "Molecular beam epitaxy," *Surface Science,* vol. 500, pp. 189-217, Mar 10 2002.

[37] A. Y. Cho, "Molecular-Beam Epitaxy," *Journal of the Electrochemical Society,* vol. 124, pp. C105-C105, 1977.

[38] C. Kittel, *Introduction to solid state physics*, 5th ed. New York: Wiley, 1976.

[39] M. Lang, L. He, F. Xiu, X. Yu, J. Tang, Y. Wang, *et al.*, "Revelation of topological surface states in Bi2Se3 thin films by in situ Al passivation," *ACS Nano,* vol. 6, pp. 295-302, Jan 24 2012.

[40] L. J. Du, I. Knez, G. Sullivan, and R. R. Du, "Robust Helical Edge Transport in Gated InAs/GaSb Bilayers," *Physical Review Letters,* vol. 114, Mar 4 2015.

[41] L. Fu and C. L. Kane, "Topological insulators with inversion symmetry," *Physical Review B,* vol. 76, Jul 2007.

[42] H. J. Zhang, C. X. Liu, X. L. Qi, X. Y. Deng, X. Dai, S. C. Zhang, *et al.*, "Electronic structures and surface states of the topological insulator Bi1-xSbx," *Physical Review B,* vol. 80, Aug 2009.

[43] A. Koma, "Vanderwaals Epitaxy - a New Epitaxial-Growth Method for a Highly Lattice-Mismatched System," *Thin Solid Films,* vol. 216, pp. 72-76, Aug 28 1992.

[44] L. He, X. F. Kou, and K. L. Wang, "Review of 3D topological insulator thin-film growth by molecular beam epitaxy and potential applications," *Physica Status Solidi-Rapid Research Letters,* vol. 7, pp. 50-63, Feb 2013.

[45] X. F. Kou, L. He, M. R. Lang, Y. B. Fan, K. Wong, Y. Jiang, *et al.*, "Manipulating Surface-Related Ferromagnetism in Modulation-Doped Topological Insulators," *Nano Letters,* vol. 13, pp. 4587-4593, Oct 2013.

[46] X. F. Kou, S. T. Guo, Y. B. Fan, L. Pan, M. R. Lang, Y. Jiang, *et al.*, "Scale-Invariant Quantum Anomalous Hall Effect in Magnetic Topological Insulators beyond the Two-Dimensional Limit (vol 113, 137201, 2014)," *Physical Review Letters,* vol. 113, Nov 7 2014.

[47] M. I. B. Utama, F. J. Belarre, C. Magen, B. Peng, J. Arbiol, and Q. H. Xiong, "Incommensurate van der Waals Epitaxy of Nanowire Arrays: A Case Study with ZnO on Muscovite Mica Substrates," *Nano Letters,* vol. 12, pp. 2146-2152, Apr 2012.

[48] K. Wang, Y. W. Liu, W. Y. Wang, N. Meyer, L. H. Bao, L. He, *et al.*, "High-quality Bi2Te3 thin films grown on mica substrates for potential optoelectronic applications," *Applied Physics Letters*, vol. 103, Jul 15 2013.

[49] Y. S. Zhou, K. Wang, W. H. Han, S. C. Rai, Y. Zhang, Y. Ding, *et al.*, "Vertically Aligned CdSe Nanowire Arrays for Energy Harvesting and Piezotronic Devices," *Acs Nano*, vol. 6, pp. 6478-6482, Jul 2012.

[50] S. M. Richardson and J. W. Richardson, "Crystal-Structure of a Pink Muscovite from Archers Post, Kenya - Implications for Reverse Pleochroism in Dioctahedral Micas," *American Mineralogist*, vol. 67, pp. 69-75, 1982.

[51] T. Fukuma, Y. Ueda, S. Yoshioka, and H. Asakawa, "Atomic-Scale Distribution of Water Molecules at the Mica-Water Interface Visualized by Three-Dimensional Scanning Force Microscopy," *Physical Review Letters*, vol. 104, Jan 8 2010.

[52] W. J. Takei, D. E. Cox, and G. Shirane, "Magnetic Structures in the MnSb-CrSb System," *Physical Review*, vol. 129, pp. 2008-2018, 1963.

[53] N. Wu, X. He, A. L. Wysocki, U. Lanke, T. Komesu, K. D. Belashchenko, *et al.*, "Imaging and Control of Surface Magnetization Domains in a Magnetoelectric Antiferromagnet," *Physical Review Letters*, vol. 106, Feb 23 2011.

[54] T. Ashida, M. Oida, N. Shimomura, T. Nozaki, T. Shibata, and M. Sahashi, "Observation of magnetoelectric effect in Cr2O3/Pt/Co thin film system," *Applied Physics Letters*, vol. 104, Apr 14 2014.

[55] M. Street, W. Echtenkamp, T. Komesu, S. Cao, P. A. Dowben, and C. Binek, "Increasing the Neel temperature of magnetoelectric chromia for voltage-controlled spintronics," *Applied Physics Letters*, vol. 104, Jun 2 2014.

[56] M. A. Henderson and S. A. Chambers, "HREELS, TPD and XPS study of the interaction of water with the alpha-Cr2O3(001) surface," *Surface Science*, vol. 449, pp. 135-150, Mar 20 2000.

[57] X. He, Y. Wang, N. Wu, A. N. Caruso, E. Vescovo, K. D. Belashchenko, *et al.*, "Robust isothermal electric control of exchange bias at room temperature," *Nature Materials*, vol. 9, pp. 579-585, Jul 2010.

[58] L. M. Corliss, N. Elliott, R. L. Sass, and J. M. Hastings, "Magnetic Structure of Chromium Selenide," *Physical Review*, vol. 122, pp. 1402-&, 1961.

[59] V. A. Ivanova, D. S. Abdinov, and G. M. Aliev, "On Some Characteristics of Chromium Selenides," *Physica Status Solidi,* vol. 24, pp. K145-&, 1967.

[60] J. G. Checkelsky, R. Yoshimi, A. Tsukazaki, K. S. Takahashi, Y. Kozuka, J. Falson, *et al.*, "Trajectory of the anomalous Hall effect towards the quantized state in a ferromagnetic topological insulator," *Nature Physics,* vol. 10, pp. 731-736, Oct 2014.

[61] S. Grauer, S. Schreyeck, M. Winnerlein, K. Brunner, C. Gould, and L. W. Molenkamp, "Coincidence of superparamagnetism and perfect quantization in the quantum anomalous Hall state," *Physical Review B,* vol. 92, Nov 30 2015.

[62] A. J. Bestwick, E. J. Fox, X. F. Kou, L. Pan, K. L. Wang, and D. Goldhaber-Gordon, "Precise Quantization of the Anomalous Hall Effect near Zero Magnetic Field," *Physical Review Letters,* vol. 114, May 4 2015.

[63] S. Kivelson, D. H. Lee, and S. C. Zhang, "Global Phase-Diagram in the Quantum Hall-Effect," *Physical Review B,* vol. 46, pp. 2223-2238, Jul 15 1992.

[64] F. von Oppen, B. I. Halperin, and A. Stern, "Conductivity tensor of striped quantum Hall phases," *Physical Review Letters,* vol. 84, pp. 2937-2940, Mar 27 2000.

[65] J. Wang, B. Lian, and S. C. Zhang, "Universal scaling of the quantum anomalous Hall plateau transition," *Physical Review B,* vol. 89, Feb 7 2014.

[66] C. X. Liu, H. Zhang, B. H. Yan, X. L. Qi, T. Frauenheim, X. Dai, *et al.*, "Oscillatory crossover from two-dimensional to three-dimensional topological insulators," *Physical Review B,* vol. 81, Jan 2010.

[67] Y. Zhang, K. He, C. Z. Chang, C. L. Song, L. L. Wang, X. Chen, *et al.*, "Crossover of the three-dimensional topological insulator Bi2Se3 to the two-dimensional limit," *Nature Physics,* vol. 6, pp. 584-588, Aug 2010.

[68] J. G. Checkelsky, L. Li, and N. P. Ong, "Zero-energy state in graphene in a high magnetic field," *Physical Review Letters,* vol. 100, May 23 2008.

[69] G. S. Boebinger, H. L. Stormer, D. C. Tsui, A. M. Chang, J. C. M. Hwang, A. Y. Cho, *et al.*, "Activation-Energies And Localization In the Fractional Quantum Hall-Effect," *Physical Review B,* vol. 36, pp. 7919-7929, Nov 15 1987.

[70] X. F. Kou, L. Pan, J. Wang, Y. B. Fan, E. S. Choi, W. L. Lee, *et al.*, "Metal-to-insulator switching in quantum anomalous Hall states," *Nature Communications,* vol. 6, Oct 2015.

[71] Z. Jiang, Y. Zhang, H. L. Stormer, and P. Kim, "Quantum hall states near the charge-neutral dirac point in graphene," *Physical Review Letters,* vol. 99, Sep 7 2007.

[72] H. P. Wei, D. C. Tsui, M. A. Paalanen, and A. M. M. Pruisken, "Experiments on Delocalization and Universality in the Integral Quantum Hall-Effect," *Physical Review Letters,* vol. 61, pp. 1294-1296, Sep 12 1988.

[73] C. R. Dean, A. F. Young, P. Cadden-Zimansky, L. Wang, H. Ren, K. Watanabe, *et al.*, "Multicomponent fractional quantum Hall effect in graphene," *Nature Physics,* vol. 7, pp. 693-696, Sep 2011.

[74] M. J. Manfra, L. N. Pfeiffer, K. W. West, R. de Picciotto, and K. W. Baldwin, "High mobility two-dimensional hole system in GaAs/AlGaAs quantum wells grown on (100) GaAs substrates," *Applied Physics Letters,* vol. 86, Apr 18 2005.

[75] K. S. Novoselov, Z. Jiang, Y. Zhang, S. V. Morozov, H. L. Stormer, U. Zeitler, *et al.*, "Room-temperature quantum hall effect in graphene," *Science,* vol. 315, pp. 1379-1379, Mar 9 2007.

[76] C. Z. Chang, W. W. Zhao, D. Y. Kim, H. J. Zhang, B. A. Assaf, D. Heiman, *et al.*, "High-precision realization of robust quantum anomalous Hall state in a hard ferromagnetic topological insulator," *Nature Materials,* vol. 14, pp. 473-477, May 2015.

[77] Z. H. Zhou, Y. J. Chien, and C. Uher, "Thin-film ferromagnetic semiconductors based on Sb2-xVxTe3 with T-C of 177 K," *Applied Physics Letters,* vol. 87, Sep 12 2005.

[78] M. H. Liu, W. D. Wang, A. R. Richardella, A. Kandala, J. Li, A. Yazdani, *et al.*, "Large discrete jumps observed in the transition between Chern states in a ferromagnetic topological insulator," *Science Advances,* vol. 2, Jul 2016.

[79] Y. B. Ou, C. Liu, L. G. Zhang, Y. Feng, G. Y. Jiang, D. Y. Zhao, *et al.*, "Heavily Cr-doped (Bi,Sb)(2)Te-3 as a ferromagnetic insulator with electrically tunable conductivity," *Apl Materials,* vol. 4, Aug 2016.

[80] E. O. Lachman, A. F. Young, A. Richardella, J. Cuppens, H. R. Naren, Y. Anahory, *et al.*, "Visualization of superparamagnetic dynamics in magnetic topological insulators," *Sci Adv,* vol. 1, p. e1500740, Nov 2015.

[81] E. O. Lachman, M. Mogi, J. Sarkar, A. Uri, K. Bagani, Y. Anahory, *et al.*, "Observation of superparamagnetism in coexistence with quantum anomalous Hall C=±1 and C=0 Chern states," *ArXiv e-prints,* vol. 1710, 2017.

[82] W. Li, M. Claassen, C. Z. Chang, B. Moritz, T. Jia, C. Zhang, *et al.*, "Origin of the low critical observing temperature of the quantum anomalous Hall effect in V-doped (Bi, Sb)2Te3 film," *Sci Rep*, vol. 6, p. 32732, Sep 07 2016.

[83] T. R. F. Peixoto, H. Bentmann, S. Schreyeck, M. Winnerlein, C. Seibel, H. Maass, *et al.*, "Impurity states in the magnetic topological insulator V:(Bi,Sb)(2)Te-3," *Physical Review B*, vol. 94, Nov 22 2016.

[84] X. Feng, Y. Feng, J. Wang, Y. B. Ou, Z. Q. Hao, C. Liu, *et al.*, "Thickness Dependence of the Quantum Anomalous Hall Effect in Magnetic Topological Insulator Films," *Advanced Materials*, vol. 28, pp. 6386-+, Aug 10 2016.

[85] J. Wang, Q. Zhou, B. Lian, and S. C. Zhang, "Chiral topological superconductor and half-integer conductance plateau from quantum anomalous Hall plateau transition," *Physical Review B*, vol. 92, Aug 31 2015.

[86] Q. L. He, L. Pan, A. L. Stern, E. C. Burks, X. Che, G. Yin, *et al.*, "Chiral Majorana fermion modes in a quantum anomalous Hall insulator-superconductor structure," *Science*, vol. 357, pp. 294-299, Jul 21 2017.

[87] M. M. Fogler, D. G. Polyakov, and B. I. Shklovskii, "Activated conductivity in the quantum Hall effect," *Surface Science*, vol. 361, pp. 255-260, 1996.

[88] A. J. M. Giesbers, U. Zeitler, M. I. Katsnelson, L. A. Ponomarenko, T. M. Mohiuddin, and J. C. Maan, "Quantum-hall activation gaps in graphene," *Physical Review Letters*, vol. 99, Nov 16 2007.

[89] R. Yoshimi, K. Yasuda, A. Tsukazaki, K. S. Takahashi, N. Nagaosa, M. Kawasaki, *et al.*, "Quantum Hall states stabilized in semi-magnetic bilayers of topological insulators," *Nature Communications*, vol. 6, Oct 2015.

[90] G. S. Boebinger, A. M. Chang, H. L. Stormer, and D. C. Tsui, "Magnetic-Field Dependence Of Activation-Energies In the Fractional Quantum Hall-Effect," *Physical Review Letters*, vol. 55, pp. 1606-1609, 1985.

[91] K. I. Bolotin, F. Ghahari, M. D. Shulman, H. L. Stormer, and P. Kim, "Observation of the fractional quantum Hall effect in graphene," *Nature*, vol. 462, pp. 196-199, Nov 12 2009.

[92] A. Tsukazaki, S. Akasaka, K. Nakahara, Y. Ohno, H. Ohno, D. Maryenko, *et al.*, "Observation of the fractional quantum Hall effect in an oxide," *Nature Materials*, vol. 9, pp. 889-893, Nov 2010.

[93] C. Michel, P. J. Klar, S. D. Baranovskii, and P. Thomas, "Influence of magnetic-field-induced tuning of disorder and band structure on the magnetoresistance of paramagnetic dilute magnetic semiconductors," *Physical Review B*, vol. 69, Apr 2004.

[94] H. B. Wu, K. Chang, and J. B. Xia, "Electronic structure of diluted magnetic semiconductor superlattices: In-plane magnetic field effect," *Physical Review B*, vol. 65, May 15 2002.

[95] J. M. Zhang, W. M. Ming, Z. G. Huang, G. B. Liu, X. F. Kou, Y. B. Fan, *et al.*, "Stability, electronic, and magnetic properties of the magnetically doped topological insulators Bi2Se3, Bi2Te3, and Sb2Te3," *Physical Review B*, vol. 88, Dec 30 2013.

[96] J. Xia, Y. Maeno, P. T. Beyersdorf, M. M. Fejer, and A. Kapitulnik, "High resolution polar Kerr effect measurements of Sr2RuO4: Evidence for broken time-reversal symmetry in the superconducting state," *Physical Review Letters*, vol. 97, Oct 20 2006.

[97] C. Y. Yang, S. J. Chang, M. H. Lee, K. H. Shen, S. Y. Yang, H. J. Lin, *et al.*, "Competing Anisotropy-Tunneling Correlation of the CoFeB/MgO Perpendicular Magnetic Tunnel Junction: An Electronic Approach," *Sci Rep*, vol. 5, p. 17169, Nov 24 2015.

[98] C. M. Liu, Y. C. Tseng, C. Chen, M. C. Hsu, T. Y. Chao, and Y. T. Cheng, "Superparamagnetic and ferromagnetic Ni nanorod arrays fabricated on Si substrates using electroless deposition," *Nanotechnology*, vol. 20, Oct 14 2009.

[99] A. Aharoni, *Introduction to the theory of ferromagnetism*, 2nd ed. Oxford ; New York: Oxford University Press, 2000.

[100] B. D. Cullity and C. D. Graham, *Introduction to magnetic materials*, 2nd ed. Hoboken, N.J.: IEEE/Wiley, 2009.

[101] Y. J. Ke, X. Q. Zhang, Y. Ma, and Z. H. Cheng, "Anisotropic magnetic entropy change in RFeO3 single crystals (R = Tb, Tm, or Y)," *Sci Rep*, vol. 6, p. 19775, Jan 25 2016.

[102] S. Cao, H. Zhao, B. Kang, J. Zhang, and W. Ren, "Temperature induced spin switching in SmFeO3 single crystal," *Sci Rep*, vol. 4, p. 5960, Aug 5 2014.

[103] L. B. Duffy, A. I. Figueroa, L. Gladczuk, N. J. Steinke, K. Kummer, G. van der Laan, *et al.*, "Magnetic proximity coupling to Cr-doped Sb2Te3 thin films," *Physical Review B*, vol. 95, Jun 19 2017.

[104] M. Ye, W. Li, S. Zhu, Y. Takeda, Y. Saitoh, J. Wang, *et al.*, "Carrier-mediated ferromagnetism in the magnetic topological insulator Cr-doped (Sb,Bi)2Te3," *Nat Commun*, vol. 6, p. 8913, Nov 19 2015.

[105] S. K. Kushwaha, I. Pletikosic, T. Liang, A. Gyenis, S. H. Lapidus, Y. Tian, *et al.*, "Sn-doped Bi1.1Sb0.9Te2S bulk crystal topological insulator with excellent properties," *Nature Communications,* vol. 7, Apr 2016.

[106] Y. Xu, I. Miotkowski, C. Liu, J. F. Tian, H. Nam, N. Alidoust, *et al.*, "Observation of topological surface state quantum Hall effect in an intrinsic three-dimensional topological insulator," *Nature Physics,* vol. 10, pp. 956-963, Dec 2014.

[107] M. Mogi, R. Yoshimi, A. Tsukazaki, K. Yasuda, Y. Kozuka, K. S. Takahashi, *et al.*, "Magnetic modulation doping in topological insulators toward higher-temperature quantum anomalous Hall effect," *Applied Physics Letters,* vol. 107, Nov 2 2015.

[108] Z. Yue and M. E. Raikh, "Smearing of the quantum anomalous Hall effect due to statistical fluctuations of magnetic dopants," *Physical Review B,* vol. 94, Oct 31 2016.

[109] I. Lee, C. K. Kim, J. Lee, S. J. L. Billinge, R. D. Zhong, J. A. Schneeloch, *et al.*, "Imaging Dirac-mass disorder from magnetic dopant atoms in the ferromagnetic topological insulator Cr-x(Bi0.1Sb0.9)(2-x)Te-3," *Proceedings Of the National Academy Of Sciences Of the United States Of America,* vol. 112, pp. 1316-1321, Feb 3 2015.

[110] C. C. Chen, M. L. Teague, L. He, X. Kou, M. Lang, W. Fan, *et al.*, "Magnetism-induced massive Dirac spectra and topological defects in the surface state of Cr-doped Bi2Se3-bilayer topological insulators," *New Journal of Physics,* vol. 17, Nov 17 2015.

[111] X. Che, K. Murata, L. Pan, Q. L. He, G. Yu, Q. Shao, *et al.*, "Proximity-Induced Magnetic Order in a Transferred Topological Insulator Thin Film on a Magnetic Insulator," *ACS Nano,* vol. 12, pp. 5042-5050, May 22 2018.

[112] D. Xiao, J. Jiang, J. H. Shin, W. Wang, F. Wang, Y. F. Zhao, *et al.*, "Realization of the Axion Insulator State in Quantum Anomalous Hall Sandwich Heterostructures," *Phys Rev Lett,* vol. 120, p. 056801, Feb 2 2018.

[113] M. Mogi, M. Kawamura, A. Tsukazaki, R. Yoshimi, K. S. Takahashi, M. Kawasaki, *et al.*, "Tailoring tricolor structure of magnetic topological insulator for robust axion insulator," *Sci Adv,* vol. 3, p. eaao1669, Oct 2017.

[114] H. Z. Lu, W. Y. Shan, W. Yao, Q. Niu, and S. Q. Shen, "Massive Dirac fermions and spin physics in an ultrathin film of topological insulator," *Physical Review B,* vol. 81, Mar 2010.

[115] R. D. Li, J. Wang, X. L. Qi, and S. C. Zhang, "Dynamical axion field in topological magnetic insulators," *Nature Physics,* vol. 6, pp. 284-288, Apr 2010.

[116] Y. B. Fan, P. Upadhyaya, X. F. Kou, M. R. Lang, S. Takei, Z. X. Wang, *et al.*, "Magnetization switching through giant spin-orbit torque in a magnetically doped topological insulator heterostructure," *Nature Materials,* vol. 13, pp. 699-704, Jul 2014.

[117] Q. L. He, G. Yin, L. Yu, A. J. Grutter, L. Pan, C. Z. Chen, *et al.*, "Topological Transitions Induced by Antiferromagnetism in a Thin-Film Topological Insulator," *Phys Rev Lett,* vol. 121, p. 096802, Aug 31 2018.

[118] G. Y. Jiang, Y. Feng, W. X. Wu, S. R. Li, Y. H. Bai, Y. X. Li, *et al.*, "Quantum Anomalous Hall Multilayers Grown by Molecular Beam Epitaxy," *Chinese Physics Letters,* vol. 35, Jun 2018.

[119] T. Ashida, M. Oida, N. Shimomura, T. Nozaki, T. Shibata, and M. Sahashi, "Isothermal electric switching of magnetization in Cr2O3/Co thin film system," *Applied Physics Letters,* vol. 106, Mar 30 2015.

[120] M. Mogi, M. Kawamura, R. Yoshimi, A. Tsukazaki, Y. Kozuka, N. Shirakawa, *et al.*, "A magnetic heterostructure of topological insulators as a candidate for an axion insulator," *Nat Mater,* vol. advance online publication, 02/13/online 2017.

[121] T. Nozaki, M. Oida, T. Ashida, N. Shimomura, T. Shibata, and M. Sahashi, "Positive exchange bias observed in Pt-inserted Cr2O3/Co exchange coupled bilayers," *Applied Physics Letters,* vol. 105, Nov 24 2014.

[122] J. Nogues and I. K. Schuller, "Exchange bias," *Journal of Magnetism and Magnetic Materials,* vol. 192, pp. 203-232, Feb 1999.

[123] R. L. Stamps, "Mechanisms for exchange bias," *Journal of Physics D-Applied Physics,* vol. 33, pp. R247-R268, Dec 7 2000.

[124] R. Jungblut, R. Coehoorn, M. T. Johnson, J. A. Destegge, and A. Reinders, "Orientational Dependence of the Exchange Biasing in Molecular-Beam-Epitaxy-Grown Ni80fe20/Fe50mn50 Bilayers," *Journal of Applied Physics,* vol. 75, pp. 6659-6664, May 15 1994.

[125] D. Mauri, H. C. Siegmann, P. S. Bagus, and E. Kay, "Simple-Model for Thin Ferromagnetic-Films Exchange Coupled to an Antiferromagnetic Substrate," *Journal of Applied Physics,* vol. 62, pp. 3047-3049, Oct 1 1987.

[126] K. Nagasaka, L. Varga, Y. Shimizu, S. Eguchi, and A. Tanaka, "The temperature dependence of exchange anisotropy in ferromagnetic/PdPtMn bilayers," *Journal of Applied Physics,* vol. 87, pp. 6433-6435, May 1 2000.

[127] U. Nowak, K. D. Usadel, J. Keller, P. Miltenyi, B. Beschoten, and G. Guntherodt, "Domain state model for exchange bias. I. Theory," *Physical Review B,* vol. 66, Jul 1 2002.

[128] T. J. Moran, J. M. Gallego, and I. K. Schuller, "Increased Exchange-Anisotropy Due to Disorder at Permalloy/Coo Interfaces," *Journal of Applied Physics,* vol. 78, pp. 1887-1891, Aug 1 1995.

[129] K. Takano, R. H. Kodama, A. E. Berkowitz, W. Cao, and G. Thomas, "Interfacial uncompensated antiferromagnetic spins: Role in unidirectional anisotropy in polycrystalline Ni81Fe19/CoO bilayers," *Physical Review Letters,* vol. 79, pp. 1130-1133, Aug 11 1997.

[130] J. Nogues, T. J. Moran, D. Lederman, I. K. Schuller, and K. V. Rao, "Role of interfacial structure on exchange-biased FeF2-Fe," *Physical Review B,* vol. 59, pp. 6984-6993, Mar 1 1999.

[131] T. J. Moran, J. Nogues, D. Lederman, and I. K. Schuller, "Perpendicular coupling at Fe-FeF2 interfaces," *Applied Physics Letters,* vol. 72, pp. 617-619, Feb 2 1998.

[132] D. Lederman, J. Nogues, and I. K. Schuller, "Exchange anisotropy and the antiferromagnetic surface order parameter," *Physical Review B,* vol. 56, pp. 2332-2335, Aug 1 1997.

[133] J. X. Shen and M. T. Kief, "Exchange coupling between NiO and NiFe thin films," *Journal of Applied Physics,* vol. 79, pp. 5008-5010, Apr 15 1996.

[134] W. Echtenkamp and C. Binek, "Electric Control of Exchange Bias Training," *Physical Review Letters,* vol. 111, Oct 31 2013.

[135] S. Cao, X. Zhang, N. Wu, A. T. N'Diaye, G. Chen, A. K. Schmid, *et al.,* "Spin polarization asymmetry at the surface of chromia," *New Journal of Physics,* vol. 16, Jul 17 2014.

[136] A. I. Figueroa, "et al., Magnetic Cr doping of Bi2Se3: Evidence for divalent Cr from x-ray spectroscopy," *Physical Review B,* vol. 90, p. 134402, 2014.

[137] H. Ohldag, "et al., Correlation between Exchange Bias and Pinned Interfacial Spins," *Physical Review Letters,* vol. 91, p. 017203, 2003.

[138] R. Cheng, "et al., Potential phase control of chromium oxide thin films prepared by laser-initiated organometallic chemical vapor deposition," *Applied Physics Letters,* vol. 78, pp. 521-523, 2001.

[139] S. Zhang, "et al., Cr enhanced ferromagnetism in $La_{0.5}Ba_{0.5}CoO_3$ due to possible double-exchange interaction," *Journal of Alloys and Compounds,* vol. 628, pp. 251–256, 2015.

[140] P. Schlottmann, "et al., Double-exchange mechanism for CrO_2," *Physical Review B,* vol. 67, p. 174419, 2003.

[141] M. J. R. Hoch, "et al., Disorder and double-exchange spin dynamics in $La_{0.7}Sr_{0.3}MnO_3$ and $La_{0.7}Sr_{0.3}CoO_3$ from NMR hyperfine couplings," *Physical Review B,* vol. 75, p. 104421, 2007.

[142] B. J. Kirby, "Phase-sensitive specular neutron reflectometry for imaging the nanometer scale composition depth profile of thin-film materials," *Current Opinion in Colloid & Interface Science,* vol. 17, pp. 44-53, 2012.

[143] M. Ye, "et al., Carrier-mediated ferromagnetism in the magnetic topological insulator Cr-doped $(Sb,Bi)_2Te_3$," *Nature Communications,* vol. 6, p. 8913, 2015.

[144] L. B. Duffy, "et al., Magnetic proximity coupling to Cr-doped Sb_2Te_3 thin films," *Physical Review B,* vol. 95, p. 224422, 2017.

[145] A. Kimura, "et al., Magnetic circular dichroism in the soft-x-ray absorption spectra of Mn-based magnetic intermetallic compounds," *Physical Review B,* vol. 56, pp. 6021-6030, 1997.